Numerical and Experimental Investigation of Multistable Systems

by

Dennis J. Tweten

Department of Mechanical Engineering and Materials Science
Duke University

Date: _____

Approved:

_____
Brian P. Mann, Supervisor

_____
Donald Bliss

_____
Terrence Oas

_____
Lawrie Virgin

_____
Stefan Zauscher

Dissertation submitted in partial fulfillment of the requirements for the degree of Doctor of Philosophy in the Department of Mechanical Engineering and Materials Science
in the Graduate School of Duke University
2013

Abstract

Numerical and Experimental Investigation of Multistable Systems

by

Dennis J. Tweten

Department of Mechanical Engineering and Materials Science
Duke University

Date: _____

Approved:

_____
Brian P. Mann, Supervisor

_____
Donald Bliss

_____
Terrence Oas

_____
Lawrie Virgin

_____
Stefan Zauscher

An abstract of a dissertation submitted in partial fulfillment of the requirements for the degree of Doctor of Philosophy in the Department of Mechanical Engineering and Materials Science
in the Graduate School of Duke University
2013

Abstract

The focus of this dissertation is on phenomena exhibited by multistable systems. Two phenomena of particular importance are chaos control and stochastic resonance. In this work, both models that can predict ordered responses and experiments in which ordered responses occur are explored. In addition, parameter identification methods are presented and improved.

Chaos control, when implemented with delays, can be an effective way to stabilize unstable periodic orbits within a multistable system experiencing a chaotic response. Delayed control is easy to implement physically but greatly increases the complexity of analyzing such systems. In this work, the spectral element method was adapted to evaluate unstable periodic orbits stabilized by feedback control implemented with delays. Examples are presented for Duffing systems in which the delay is equal to the forcing period. The spectral approach is also extended to analyze the control of chaos with arbitrary delays. Control with arbitrary delays can also be used to stabilize equilibria within the chaotic response. These methods for arbitrary delays are explored in self-excited, chaotic systems.

Stochastic resonance occurs in multistable systems when an increase in noise results in an ordered response. It is well known that noise excitation of multistable systems results in the system escaping from potential wells or switching between wells. In stochastic resonance, a small external signal is amplified due to these switching events. Methods for modeling stochastic resonance in both underdamped and

overdamped systems are presented. In addition, stochastic resonance in a bistable, composite beam excited by colored noise is investigated experimentally. The experimental results are compared with analytical models, and the effect of modal masses on the analytical expressions is explored. Finally, an alternative approach for calculating the effect of colored noise excitation is proposed.

In order to implement analysis methods related to delay differential equations or stochastic resonance, the parameters of the system must be known in advance or determined experimentally. Parameter identification methods provide a natural connection between experiment and theory. In this work, the harmonic balance parameter identification method was applied to beam energy harvesters and is improved using weighting matrices. The method has been applied to a nonlinear, bistable, piezoelectric beam with a tip mass. Then, an experimental method of determining the number of restoring force coefficients necessary to accurately model the systems was demonstrated. The harmonic balance method was also applied to a bistable, beam system undergoing stochastic resonance. Finally, a new weighting strategy is presented based on the signal to noise ratio of each harmonic.

To my wife Kimberly

Contents

List of Tables

List of Figures

List of Abbreviations and Symbols

Symbols

D	Noise Intensity
E	Young's modulus
k_B	Boltzmann constant
m	Mass
r_K	Kramers rate
t	Time
ω	Response frequency
ω_n	Natural frequency
Ω	Forcing frequency
σ	Standard deviation
τ	Delay
ζ	Damping ratio

Abbreviations

DDE	Delay differential equation
DFC	Delayed feedback control
DOF	Degree of freedom
EDFC	Extended delayed feedback control
EOM	Equation of motion

FE	Floquet exponent
FFT	Fast Fourier transform
HBID	Harmonic balance identification
LGL	Legendre-Gauss-Lobatto
LRT	Linear response theory
LS	Least Squares
MDFC	Multiple delay feedback control
ODE	Ordinary differential equation
PSD	Power spectral density
RTD	Residence time distribution
SDOF	Single degree of freedom
SNR	Signal to noise ratio
SPA	Spectral power amplification
SR	Stochastic resonance
UPO	Unstable periodic orbit

Acknowledgements

I would like to thank Professor Brian Mann for his advice, support, and help. I truly appreciate the time and commitment he showed to me to help me become a better researcher. I have learned a great deal about both proteins and research by working with Prof. Mann, Prof. Terry Oas, Prof. Stefan Zauscher, Prof. Piotr Marszalek, and Dr. Zehra Parlak, and I appreciate being part of many worthwhile discussions. I also want to thank Prof. Donald Bliss, Prof. Lawrie Virgin, Prof. Oas, and Prof. Zauscher for serving on several of my committees and for their insightful feedback and suggestions.

Chapter 4 is closely based on the paper by Tweten et al. (2012). I would like to thank Genevieve Lipp, Dr. Firas Khasawneh, and Prof. Brian Mann for their contribution to this work.

I have been part of a great group of colleagues from whom I have learned and with whom I have enjoyed working. Clark McGehee, Zach Ballard, Ben Owens, Genevieve Lipp, Dr. Firas Khasawneh, Dr. Sam Stanton, and Dr. Simo Sah have all contributed to my research and provided helpful feedback.

My family has been amazingly supportive. Kimberly, you have been there for me every step of the way, and it has meant so much to me. Finally, I would like to thank Lillian, Evelyn, and Annelise for taking this adventure with me.

1

Introductory Material

In this section, challenges and opportunities of working with multistable systems are presented. The opportunities discussed revolve around the emergence of order within complex responses of multistable systems. In addition, specialized methods for modeling and predicting these ordered responses are discussed. Then, the content of the work and a brief preview of each chapter is provided.

1.1 Background

Multistable systems present innumerable challenges and opportunities for investigators. Whether endeavoring to understand complex systems or predict nonlinear, dynamical behavior, researchers must often adopt complex or specialized methods compared to equivalent linear systems. However, multistable systems also provide opportunities not available in their linear counterparts such as chaos control and stochastic resonance. Many opportunities arise from dynamics related to stable equilibriums and unstable periodic orbits (UPOs) which can be exploited to create an ordered response. For instance, adding delayed feedback to a chaotic response can stabilize UPOs, and increasing noise excitation can induce ordered switching between

stable equilibriums.

Adding delayed feedback to a multistable system greatly increases the complexity of analyzing the resulting system. For instance, solutions of delay systems based on Floquet theory result in an infinite dimensional solution (Khasawneh and Mann, 2011b). In most cases, numerical techniques which approximate the solution as finite are chosen for the analysis. The evaluation of control gains in the extended, delayed feedback control (EDFC) of chaos is a good extension of numerical delay methods. In EDFC, the UPOs embedded in a strange attractor are stabilized using delayed feedback. The system then begins to order itself resulting in the control power approaching zero.

Noise is often considered a nuisance which must be reduced or filtered, but noise in a multistable system can also lead to ordered responses such as stochastic resonance. In a nonlinear, multistable system with noise, the system randomly switches states with a mean switching rate, which typically varies with the intensity of the noise excitation (Anishchenko et al., 1999). In stochastic resonance, a small external signal is amplified due to switching events. This phenomenon is a resonance in the sense that the time scales of the signal and mean switching rate coincide at the peak amplification (Gammaitoni et al., 1995).

In order to implement analysis methods related to delay differential equations or stochastic resonance, the parameters of the system must be known in advance or determined experimentally. Parameter identification methods provide a natural connection between experiment and theory. These techniques can be used to identify properties of theoretical models, investigate unknown systems, or even as part of a design process. Linear parameter identification methods have value even for multistable systems if the system response is composed of small deviations from an equilibria. However, if parameters necessary for chaos control or stochastic resonance are to be determined, the parameter identification method must also be able

to compensate for or even take advantage of nonlinear responses.

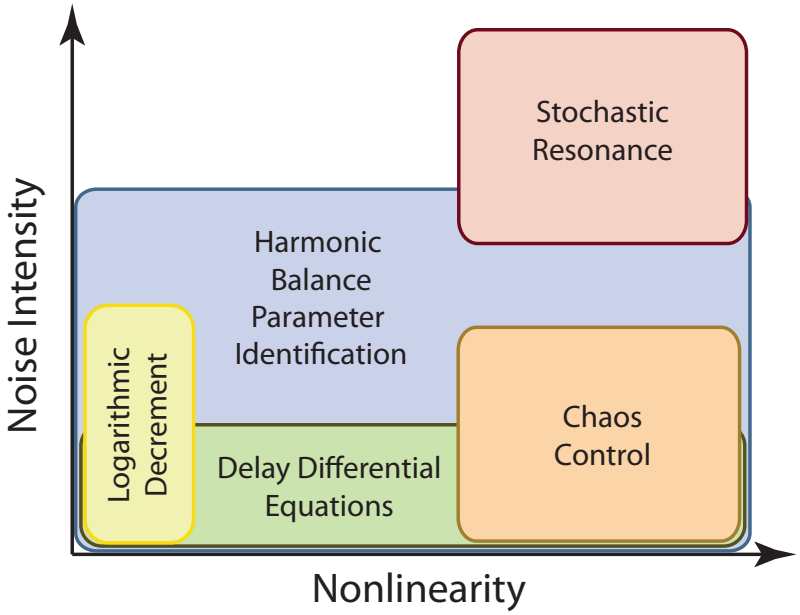

FIGURE 1.1: The plane showing noise intensity versus nonlinearity highlights the relationship between multistable system responses and numerical techniques. Both the chaos control and stochastic resonance responses require multistable systems and hence are to the right side of the nonlinear axis.

In categorizing both the response of multistable systems and methods with which to evaluate the response, one may imagine a plane of increasing nonlinearity and noise excitation such as the one in Fig. 1.1. The horizontal axis of this plane represents the range in the nonlinearity of the system. Behaviors to the left side of the plane represent nearly linear responses about an equilibria, and those to the right represent highly nonlinear responses. The vertical axis represents noise excitation with no noise at the bottom and relatively large excitation to the top. Ranges of multistable system behaviors along with modeling and parameter identification techniques are plotted in the plane for reference. Chaos control which requires a high level of nonlinearity and tolerates a moderate level of noise intensity is plotted in the lower right section of the plane. Stochastic resonance which depends on both a high level of nonlinearity and a relatively large noise excitation covers a range in the upper right portion of the plane.

Analysis methods are also included on the plane to show the relationship between nonlinear responses and the techniques discussed throughout this work. Methods for delay differential equations (DDE)s applied for analyzing chaos control can be used for all levels of nonlinearity (via linearization) and a moderate amount of noise. Parameter identification methods such as the harmonic balance identification method can be used for nonlinear systems and a much larger level of noise excitation than the DDE methods. Finally, the logarithmic decrement method is limited to nearly linear responses but can be used for a fairly wide range of noise excitations.

1.2 Dissertation Organization

In chapter 2, the harmonic balance parameter identification method is applied to beam energy harvesters and is improved using weighting matrices. First, the method is applied to both weakly-nonlinear and nonlinear, bistable, piezoelectric beams with tip masses. Then, an experimental method for determining the number of restoring force coefficients necessary to accurately model the systems is presented. Next, the harmonic balance parameter identification method is extended to account for multiple concurrent frequencies in order to identify parameters of weakly nonlinear systems. System parameters are identified for the two experimental energy harvesters. Subsequently, a new weighting strategy is presented based on the signal to noise ratio of each harmonic. This new weighting strategy is compared with the typically unweighted method for estimating parameters from data with Gaussian, uniform, and Laplacian noise distributions. Finally, chapter 2 explores the relationship between the accuracy of the estimated parameters and the range of phase space transversed by a steady state response. This chapter is based on the work published in Tweten and Mann (2012a, 2013).

Chapter 3 presents an uncertainty analysis on the logarithmic decrement method which provides a deeper understanding of the influences of measurement uncertainty,

damping, and the number of periods on the estimated damping ratio. In particular, the trade-off between increasing the number of periods and measurement noise is addressed. The insights gained from this analysis are condensed into a single figure which provides the ideal number of periods to use. The figure is applicable for a common range of measurement uncertainties and damping ratios.

In chapter 4, a comparison of the semi-discretization, spectral element, and Legendre collocation methods is presented. Each method is a technique for solving DDEs as well as determining regions of stability in the DDE parameter space. First, the necessary concepts, assumptions, and equations required to implement each method are provided. Then, the criteria of convergence rate and computational time are defined. Finally, using these criteria, each method is compared using three numerical studies: a ship stability example, the delayed damped Mathieu equation, and a helicopter rotor control problem. This chapter is based on collaborative work published by Tweten et al. (2012).

In chapter 5, the spectral element approach is adapted to evaluate UPOs stabilized by EDFC. Examples are presented for stabilizing UPOs in Duffing systems in which the delay is equal to the forcing period. The Floquet exponents (FE)s calculated by the spectral approach are compared to published results for two examples. In addition, the spectral method was used to analyze a high dimensional, asymmetrical system with a UPO in chaos arising from tori doubling following a Hopf bifurcation. This chapter is based on the work published in Tweten and Mann (2012b).

The spectral approach is extended in chapter 6 to the control of chaos with arbitrary control delays. Three important cases are explored using the spectral approach: half-period delayed feedback control (DFC), control loop latency in DFC and EDFC, and steady state control using multiple delay feedback control (MDFC). These control methods are explored in self-excited, chaotic systems.

In chapter 7, methods for evaluating stochastic resonance and numerical techniques for modeling stochastic resonance in overdamped systems are presented. First, stochastic resonance is defined, and the basic mechanisms such as times-scale coincidence are discussed. Then, the analytical techniques derived from two-state theory and linear response theory for stochastic resonance theory modeling are presented. In addition, numerical techniques for evaluating the signal amplification such as spectral power amplification (SPA) and signal to noise (SNR) ratio are presented. Finally, comparisons between simulated data and analytical models are presented for overdamped stochastic resonance.

In chapter 8, stochastic resonance in a bistable, composite beam excited by colored noise is investigated experimentally. Experimental results for average upcrossing period, SPA, and SNR are compared with analytical methods for underdamped systems. These analytical methods include expressions developed from Kramers, Melnikov, and two-state theory. Also, the effect of a modal mass on the analytical expressions is explored. Finally, an alternative approach for estimating the effect of a colored noise spectrum on the SPA and SNR of underdamped systems is proposed.

A brief summary and the important conclusions of each chapter are presented in chapter 9. In addition, future work based on the results and conclusions presented in the previous chapters is proposed. The proposed future work is focused on parameter identification, chaos control, and stochastic resonance.

2

Harmonic Balance Parameter Identification

There are a wide variety of applications for vibratory energy harvesters including powering structural health monitoring networks (Park et al., 2008), charging batteries (Sodano et al., 2005), and powering wireless sensors (Ottman et al., 2002). Many vibratory energy harvesters are linear systems which attempt to maximize power by matching the system's resonant frequency with ambient vibration. The main limitation of this approach is the trade-off between the magnitude and the bandwidth of the response. The intentional use of nonlinearity in energy harvesters has recently gained interest because of the potential to combine large responses with a wider response in bandwidth as compared to linear oscillators (Mann and Sims, 2009). Thorough investigation of nonlinear oscillators involves theoretical models to predict behavior and to both design and interpret experiments (Stanton et al., 2010). However, the behavior of nonlinear oscillators is significantly more complicated than linear oscillators. Determining accurate parameters for a theoretical, nonlinear model can be difficult due to large uncertainties in magnetic properties, composite beams, and piezoelectric characteristics among others. Therefore, the investigation of energy harvesters from experimentally determined parameters is an important task (Stanton

et al., 2011).

Model parameters for such systems can often be determined using experimental time history data. A number of parameter identification methods which use experimental time data are available, such as the energy balance (Mann and Khasawneh, 2009; Liang and Feeny, 2006), harmonic balance (Yasuda et al., 1988b), and direct parameter estimation (Mohammad et al., 1992) methods. Additional parameter identification methods are discussed in an excellent survey by Kerschen et al. (2006). For nonlinear energy harvesters, parameter identification methods which require few measurements, such as position and base acceleration, and which take advantage of the steady state response are of particular interest.

The harmonic balance identification (HBID) method uses the Least-Squares (LS) method to identify parameters from the steady state response. A typical approach to improve the LS method is to utilize a weighting matrix. Common weighting methods in the literature rely on the difference in variances between observations. However, in the HBID method, the variance of the elements within an observation change from column to column, but the variances of each observation are identical. That is to say the variances of the rows of the observation matrix are the same, while the variances of the columns differ. The literature currently does not include a weighting scheme that addresses the HBID method and these unique characteristics. This chapter introduces two weighting schemes designed to address the variance structure of the HBID. These weighting schemes are then compared with two baselines to determine the affect on estimated parameter accuracy from noisy data. This chapter also explores the identification of parameters using the HBID method in a reduced phase space.

The content of this chapter is organized as follows. First, the equations of motion for both single degree of freedom systems and continuous beams with base excitation are formulated. The harmonic balance method is then extended to incorporate

multiple concurrent forcing frequencies in order to apply the method to weakly nonlinear systems. A method to experimentally determine the modal mass of a beam at a single measurement location follows. Next, experimental data is compared with simulations using the parameters identified. Subsequently, a method for identifying parameters using a reduced phase space is presented. Then, the approach taken to select weighting matrices, quantify identified parameter error, and propagate uncertainty is given. Finally, four different weighting schemes within the HBID method are compared using simulated results.

2.1 Description of Physical System

This chapter first applies the harmonic balance parameter identification (HBID), also known as the describing function method (Kerschen et al., 2006), to base excited energy harvesters. The original implementation of the HBID method assumed that the excitation is applied directly to the system mass (Yasuda et al., 1988b,a) or directly to the beam (Yasuda and Kamiya, 1990). For the case of base excitation, the differential equations must be written in terms of differences between the movement of the base and mass. The following two sections present the equations for a base excited single degree of freedom system and a base excited beam.

2.1.1 Base Excited Single Degree of Freedom System

Consider the single degree of freedom (DOF) system in Fig. 2.1 with base excitation acceleration b, base position x_1, and absolute mass position x_2. In this system, the deflection is dependent on the difference between the mass and base positions, and the damping velocity is dependent on the difference between the mass and base velocities. A nonlinear restoring force with a power series model can be represented by

$$N(\Delta x) = \beta_0 + \beta_1 \Delta x + \ldots + \beta_p \Delta x^p \,, \tag{2.1}$$

where the relative position between the base and the mass is $\Delta x = x_2 - x_1$, β_i is the i^{th} restoring force coefficient per mass, and p is the order of the nonlinear restoring force. Summing the forces about the mass m, results in the following equation of motion (EOM)

$$m\ddot{x}_2 + m\mu(\dot{x}_2 - \dot{x}_1) + mN(\Delta x) = 0\,, \tag{2.2}$$

where the over dot represents differentiation with respect to time, $\ddot{x}_2$ is the acceleration of the mass, $\dot{x}_2$ is the velocity of the mass, $\dot{x}_1$ is the velocity of the base, and the damping is given by $c = m\mu$. In order to use the HBID method, all terms on the left side of the equality must be based on the same reference, which was chosen to be Δx. Dividing the equation by the mass m and then subtracting the base acceleration b from both sides results in the EOM in the desired form of

$$\Delta\ddot{x} + \mu\Delta\dot{x} + N(\Delta x) = -b\,, \tag{2.3}$$

where $b = \ddot{x}_1$, $\Delta\ddot{x} = \ddot{x}_2 - \ddot{x}_1$, and $\Delta\dot{x} = \dot{x}_2 - \dot{x}_1$.

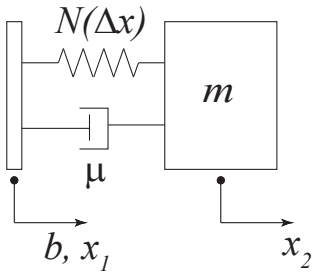

FIGURE 2.1: Nonlinear base excited system with base acceleration b, base position x_1, mass position x_2, damping μ, and nonlinear restoring force $N(\Delta x)$, where $\Delta x = x_2 - x_1$.

Once the EOM for the base excited single DOF system is rearranged into the form of Eq. (2.3), it is strait forward to implement in the HBID method. The energy harvester of interest, however, is a continuous beam with tip mass as shown in Fig. 2.3.

2.1.2 Base Excited Linear Beam

Identification methods for continuous beams have been investigated by Yasuda and Kamiya (1990), but the beam was assumed to be simply supported and externaly forced. By contrast the following equations are for a base excited, fixed-free, Euler-Bernoulli beam with tip mass.

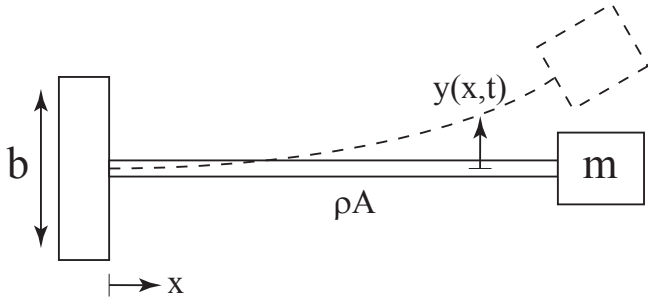

FIGURE 2.2: Top view of a beam with a tip mass, base acceleration b, position along the beam x, and relative beam deflection $y(x,t)$.

The modes for the uniform, Euler-Bernoulli, fixed-free beam are given by

$$\psi_n(x) = A_n \Big(\sin(\alpha_n x) - \sinh(\alpha_n x) - \frac{\sin(\alpha_n L) + \sinh(\alpha_n L)}{\cos(\alpha_n L) + \cosh(\alpha_n L)} (\cos(\alpha_n x) - \cosh(\alpha_n x)) \Big) , \tag{2.4}$$

where A_n is a constant and α_n is the eigenvalue. For a fixed-free beam with a tip mass, the eigenvalues are dependent on both the mass m and and the density per length ρA (Meirovitch, 2001). It should be noted that $\alpha_n^4 = \omega_n^2 \rho A / EI$ where ω_n is the modal frequency, E is Young's modulus, and I is the second moment of inertia. The boundary conditions for the uniform fixed-free beam with tip mass require that the modes be orthogonal using the relationship

$$\rho A \int_0^L \psi_n(x)\psi_p(x)\,\mathrm{d}x + m\psi_n(L)\psi_p(L) = \delta_{np}\,, \tag{2.5}$$

where ρ is the density, A is the cross sectional area, L is the beam length, $\delta_{np} = 1$ when $n = p$, and $\delta_{np} = 0$ when $n \neq p$ (Meirovitch, 2001). Using the orthogonal

relationship, the modes can be decoupled to arrive at the following equation of motion for the beam

$$\psi_n(x_p)\left(\ddot{q}_n(t) + 2\zeta\omega_n\dot{q}_n(t) + \omega_n^2 q_n(t)\right) = -Q_n b \tag{2.6a}$$

$$Q_n = \frac{\psi_n(x_p)\left(\rho A \int_0^L \psi_n(x)\,dx + \psi_n(L)m\right)}{\rho A \int_0^L \psi_n^2(x)\,dx + \psi_n^2(L)m} \tag{2.6b}$$

where x_p is the location along the beam at which the deflection is measured, $\psi_n(x_p)q_n(t)$ is the measured deflection of the beam due to the n^{th} mode, ζ is the damping, ω_n is the modal frequency of the n^{th} mode, and b is the acceleration of the base. In the present implementation of the HBID method, it is assumed that each mode can be excited independently in which case Eq. (2.6) becomes equivalent to Eq (2.3). This assumption was found to be reasonable for both systems considered in this chapter since the second modes had much higher frequencies than the first modes in both cases. The validity of this assumption for other systems can be determined by performing a frequency sweep.

If the factor Q_n can be calculated before implementing the HBID method, Q_n must be multiplied with the measured acceleration b to result in an identified mass of unity. In many cases, the beam parameters such as density and Young's modulus are not known or are not constant along the beam, or for a nonlinear beam, the beam mode may not be known. In these cases, the factor Q_n cannot be calculated with accuracy before the experiment. Instead, the acceleration is not multiplied by a factor, and each parameter is identified with a factor of $1/Q_n$ which is the modal mass. Then, the parameters may be divided by the identified modal mass to acquire the parameters.

2.1.3 Base Excited Nonlinear Beam Model

A base excited, double-well, beam energy harvester was selected for experiments and as the model for the simulations. The physical system is a piezoelectric beam with a magnetic tip mass and corresponding stationary magnet, as shown in Fig. 2.3. A

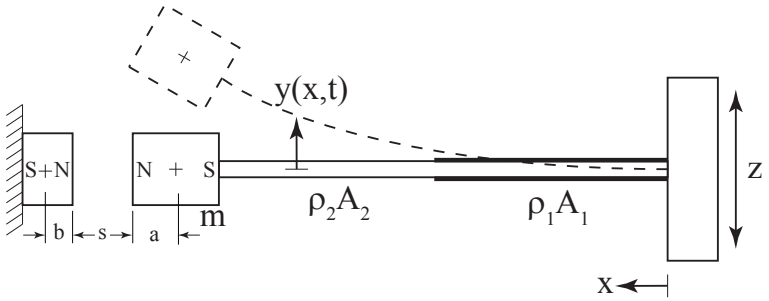

FIGURE 2.3: Top view of a beam with a tip mass, base position z, position along the beam x, and relative beam deflection $y(x,t)$. The properties for the section of the beam with the piezoelectric laminate are given by $\rho_1 A_1$, and the properties of the remaining section are given by $\rho_2 A_2$.

typical energy approach to derive the EOM for such a beam system is to formulate energy expressions of the system including the beam and magnet interaction, and to perform a modal expansion of the beam. The modal approach results in a series of decoupled, single degree of freedom, EOM based on each mode. This approach was taken by Stanton et al. (2010) to develop the EOM for a nearly identical system to the one shown in Fig. 2.3. Since the response of each mode is independent of the others, only one EOM is necessary to model the system as long as a single mode is being excited.

A further simplification of the EOM can be made by assuming a power series as an approximation for the combined restoring force of the beam and the magnet potential which was the assumption taken by Stanton et al. (2011). For this further simplification, the EOM for a single mode is

$$m\ddot{y}(L_p,t) + \mu\dot{y}(L_p,t) + \sum_{p=0}^{P} \beta_p y(L_p,t)^p = -\ddot{z}(t)\,, \tag{2.7}$$

where $y(x,t)$ is the displacement of the beam, m is the modal mass, μ is the damping, β_p is a restoring force coefficient, L_p is the location of the displacement measurement, and $\ddot{z}$ is the acceleration of the base. The parameters identified for the nonlinear beam and divided by the modal mass are $m = 1$, $\mu = 4.43$, $\beta_0 = 0.17$, $\beta_1 = -2090$, $\beta_2 = 1671$, $\beta_3 = 8.36 \times 10^8$, and $\beta_4 = -2.44 \times 10^9$. The remaining parameters measured from the setup are $L = 0.054$, $L_p = 0.032$, and $|\ddot{z}| = 0.93$. All of the simulations in this chapter whether for comparison to the experimental data or for comparison of weighting matrices use these parameters.

2.2 Harmonic Balance Parameter Identification

The HBID method identifies parameters using measurements of the displacement and applied force or acceleration. It is also possible to use HBID to estimate the parameters with only displacement measurements (Yasuda et al., 1988b). Using harmonic balance for the identification of parameters reverses the usual practice of predicting the response of a system with known parameters, forcing amplitudes, and forcing frequency (Yasuda et al., 1988b).

The Fourier coefficients of the steady state response at each forcing frequency and a predetermined number of harmonics are balanced. The Fourier coefficients of the displacement and forcing inputs can be readily found using the fast Fourier transform (FFT):

$$\text{FFT}\left\{x^p(t)\right\} = (X_0)^p + \sum_{m=1}^{M}\left(\sum_{n=1}^{\infty}\left((X_n^r)_m^p + j(X_n^j)_m^p\right)\mathrm{e}^{jn\Omega_m t}\right), \tag{2.8a}$$

$$\text{FFT}\left\{\ddot{z}^p(t)\right\} = (Q_0)^p + \sum_{m=1}^{M}\left(\sum_{n=1}^{\infty}\left((Q_n^r)_m^p + j(Q_n^j)_m^p\right)\mathrm{e}^{jn\Omega_m t}\right), \tag{2.8b}$$

where the superscript r and j indicate the real and imaginary components of the Fourier coefficient, respectively. The n^{th} harmonic of the Fourier coefficient is indicated by n, and the m^{th} forcing frequency is given by Ω_m. When finding Fourier

coefficients of the p^{th} power, each sample of the time series is raised to the p^{th} power, and the FFT is taken of the resulting time series.

Using the nomenclature in Eq. (2.8), each harmonic can be balanced into two rows where one row balances the real part (cosine terms), and the second row balances the imaginary part (sine terms) (Yasuda et al., 1988b). The response terms, x, are then assembled into an observation matrix $\mathbf{A}$, the forcing terms are placed into a column vector $\vec{Q}$, and the parameters are contained in a column vector $\vec{S}$ as shown by

$$\mathbf{A}\vec{S} = \vec{Q}\,. \tag{2.9}$$

A more explicit form of this equation is given by Eq. (2.10) in which multiple forcing frequencies are accounted from one to M, and each forcing frequency includes harmonics from one to n.

$$\begin{bmatrix} 0 & 0 & (X_0)^1 & \cdots & (X_0)^P \\ -\Omega_1^2(X_1^r)_1^1 & \Omega_1(X_1^j)_1^1 & (X_1^r)_1^1 & \cdots & (X_1^r)_1^P \\ -\Omega_1^2(X_1^j)_1^1 & -\Omega_1(X_1^r)_1^1 & (X_1^j)_1^1 & \cdots & (X_1^j)_1^P \\ \vdots & \vdots & \vdots & \ddots & \vdots \\ -n^2\Omega_1^2(X_n^r)_1^1 & \Omega_1(X_n^j)_1^1 & (X_n^r)_1^1 & \cdots & (X_n^r)_1^P \\ -n^2\Omega_1^2(X_n^j)_1^1 & -\Omega_1(X_n^r)_1^1 & (X_n^j)_1^1 & \cdots & (X_n^j)_1^P \\ -\Omega_2^2(X_1^r)_2^1 & \Omega_2(X_1^j)_2^1 & (X_1^r)_2^1 & \cdots & (X_1^r)_2^P \\ -\Omega_2^2(X_1^j)_2^1 & -\Omega_2(X_1^r)_2^1 & (X_1^j)_2^1 & \cdots & (X_1^j)_2^P \\ \vdots & \vdots & \vdots & \ddots & \vdots \\ -n^2\Omega_M^2(X_n^r)_M^1 & \Omega_M(X_1^j)_M^1 & (X_1^r)_M^1 & \cdots & (X_1^r)_M^P \\ -n^2\Omega_M^2(X_n^j)_M^1 & -\Omega_M(X_1^r)_M^1 & (X_1^j)_M^1 & \cdots & (X_1^j)_M^P \end{bmatrix} \begin{bmatrix} m \\ \mu \\ \beta_1 \\ \beta_2 \\ \vdots \\ \beta_P \end{bmatrix} = \begin{bmatrix} (Q_0)_1 \\ (Q_1^r)_1 \\ (Q_1^j)_1 \\ \vdots \\ (Q_n^r)_1 \\ (Q_n^j)_1 \\ (Q_1^r)_2 \\ (Q_1^j)_2 \\ \vdots \\ (Q_n^r)_M \\ (Q_n^j)_M \end{bmatrix} \tag{2.10}$$

The HBID method uses the least squares method to determine the parameters in $\vec{S}$, from the observation matrix $\mathbf{A}$ and the vector $\vec{Q}$. The weighted least squares method is given by

$$\vec{S} = \left(\mathbf{A}^T\mathbf{W}\mathbf{A}\right)^{-1}\mathbf{A}^T\mathbf{W}\vec{Q} \tag{2.11}$$

where $\mathbf{W}$ is a weighting matrix. The weighting matrix gives greater or less significance to each harmonic (observation) with the cosine and sine coefficients for each

harmonic given equal weight. Typical weighting schemes in the literature are based on the relative standard deviations of the observations. However, each observation in the HBID method has the same variance structure as detailed in Section 2.5.1. That is to say the variances of the rows of the observation matrix are the same, while the variances of the columns differ. For that reason, an effective weighting scheme for HBID cannot be based on differences of variances between observations.

The least squares method requires that the number of linearly independent rows in the observation matrix equal or exceed the number of parameters to be fitted (Kay, 1993). For linear systems with a single forcing frequency, these conditions may not exist especially when the magnitude of the response at the higher harmonics are small. In order to overcome this limitation for linear or weakly nonlinear systems, additional concurrent forcing frequencies must be added. In a nonlinear system, higher order harmonic responses are excited and only one forcing frequency is sufficient.

2.3 Experiments

Experiments were performed on two setups: first a weakly nonlinear beam with tip mass and secondly a nonlinear, bistable beam with tip mass. In both cases the base of the beam was fixed to a horizontally vibrating platform to limit the effect of gravity. The displacement of the beam was measured at 0.032 m from the base of the beam using a Micro-Epsilon optoNCDT LD1605-100 laser displacement measuring system. The acceleration of the platform was measured using a PCB 3713D1FD20G triaxial accelerometer. For all experiments, an external 500 hz analog filter was applied to the signal before the data was acquired at a 1000 hz sample rate.

2.3.1 Weakly Nonlinear Beam

In the weakly nonlinear beam experiment, a harmonic acceleration with three concurrent frequencies was applied to the platform. These frequencies remained constant while 5×10^5 data points were acquired. Experiments were run with concurrent frequencies of 12, 13, and 14 hz (frequency set one) and concurrent frequencies of 11, 13, and 15 hz (frequency set two). The amplitude of the side frequencies (11, 12, 14, and 15) were about one quarter of the magnitude at 13 hz. Please see Table 2.1 for the magnitudes of the acceleration at 13 hz. The following analysis was restricted to the first beam mode, since the natural frequency of the second mode was over 100 hz and was not excited.

The ideal number of restoring force coefficients (parameters) and Fourier coefficients are not known a priori. For a single DOF system such as the one in Fig. 2.1, the identified mass is a convenient check to determine the number of parameters and Fourier coefficients if the acceleration is used in the $\vec{Q}$ vector. The number of parameters and Fourier coefficients are increased until the identified mass equals the actual mass of the system which is similar to the approach taken by Yasuda et al. (1988a). However, in a continuous system, the modal mass is often not known, and in that case no convenient value is known to determine when the HBID method has converged. In order to overcome this difficulty, the modal mass was calculated using increasing numbers of parameters and Fourier coefficients and plotted in a 3D plot. Figure 2.4 shows the modal mass calculated for combinations of two to eight parameters and two to eight Fourier coefficients for the acceleration amplitude of 1.08m/s^2 using frequency set one. Convergence is taken to be the smallest number of parameters and Fourier coefficients where the plot flattens out, that is where the modal mass does not significantly change by increasing the number of parameters and Fourier coefficients. For the case shown in Fig. 2.4, two Fourier coefficients and

three parameters are required.

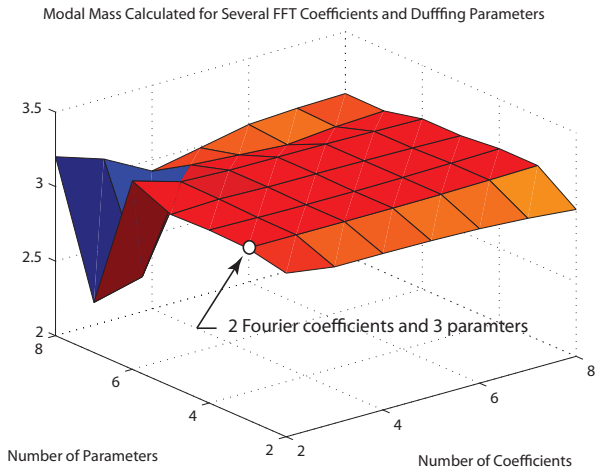

FIGURE 2.4: Modal mass for two to eight parameters and two to eight Fourier coefficients for frequency set one and a magnitude of 1.08m/s^2. Two Fourier coefficients and three parameters are required for convergence.

The HBID method was used to identify the system parameters including modal mass, damping, and the restoring force coefficients for the weakly nonlinear beam. Fewer data points were required if the noise can be filtered from the data. However, the method was applied directly to the noisy data with no digital filtering to demonstrate that such filtering is not necessary. Table 2.1 provides a summary of the modal masses (dimensionless), damping coefficients, natural frequencies, and the number of coefficients and parameters required for convergence for each experiment. Even though all of the experiments required more than one parameter, the stiffness from each experiment was determined to be linear (only one restoring force coefficient required). When the restoring force was plotted using all the restoring force coefficients and using only the first restoring force coefficient, both lines were nearly identical over the range of experimental displacements (see Fig. 2.5 for an example using frequency set one and the acceleration amplitude of 1.08m/s^2).

In order to determine the natural frequency of the physical system, the base

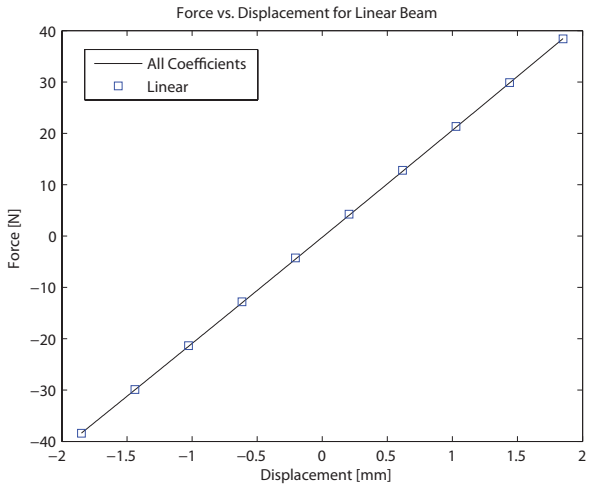

FIGURE 2.5: Comparison of the restoring force using all restoring force coefficients and the first restoring force coefficient for frequency set one and an acceleration amplitude of 1.08m/s^2.

Table 2.1: Parameters identified for the weakly nonlinear beam. Frequency set one includes the frequencies 12, 13, and 14 hz, while frequency set two includes the frequencies 11, 13, and 15. The amplitude of the 13 hz forcing frequency is given; the side frequencies have about one quarter of this magnitude.

Freq. Set	Acc. Amp. $\left[\frac{\text{m}}{\text{s}^2}\right]$	Modal Mass	Damping ζ	ω_1 $\left[\frac{\text{rad}}{\text{s}}\right]$	Coeff./ Param.
1	0.557	3.16	0.026	81.7	5/3
1	1.080	3.15	0.027	81.2	2/3
1	1.610	3.10	0.029	80.9	2/3
2	0.549	3.08	0.026	81.7	2/3
2	1.080	3.13	0.027	81.2	2/3
2	1.560	3.09	0.028	80.8	2/3

frequency was swept from 5 to 100 hz and from 100 to 5 hz. The magnitude of the acceleration was maintained constant over each frequency sweep. Three acceleration magnitudes were selected for the sweeps: 0.25 m/s^2, 0.50 m/s^2, and 1.0 m/s^2. The results of these six sweeps are given in Table 2.2 where the "Forward" column is the natural frequency found with a sweep from 5 to 100 hz and the "Backward" column is the natural frequency found with a sweep from 100 to 5 hz. The natural frequency

of 81.3 identified using the average of the results from the HBID method is less than 5% different from the largest natural frequency found using a sweep (forward sweep with an amplitude of 0.25 m/s^2). Thus, there is good agreement between the HBID method and frequency sweeps of the system.

Table 2.2: Measured natural frequencies of the weakly nonlinear beam system using a forward sweep (from 5 to 100 hz) and a backward sweep (from 100 to 5 hz).

Amplitude [m/s^2]	Forward [rad/s]	Backward [rad/s]
0.25	85.1	82.8
0.50	83.6	82.1
1.00	82.8	81.3

Finally, the modal mass calculated using the HBID method was compared with the Euler-Bernoulli model. The beam equation in Eq. (2.6) is for a uniform beam, while the experimental beam is laminated near the base and solid polymer near the tip. Therefore, the predicted modal mass and the modal mass found using parameter identification are not expected to perfectly agree.

The following measurements were made of the experimental beam to calculate the first modal mass defined by $1/Q_n$, where Q_n is defined in Eq. (2.6). The length between beam base and tip mass is $L = 0.054$ m; the distance between beam base and the measured point is $x_p = 0.032$ m; the tip mass is $m = 0.0053$ kg, and the first eigenvalue is $\alpha_1 = 8.06$. The average mass density per length of the beam is $\rho A = 0.0012$ kg/m. The average mass density was measured by weighing the laminated and polymer sections of the beam together and dividing by the total length of both sections.

Using these parameters and the beam mode from Eq. 2.4, the modal mass was calculated to be $1/Q_n = 2.39$. The average modal mass of 3.12 identified by the HBID method is remarkably close to the estimate by the beam theory considering that the beam theory assumed a uniform beam. This similarity indicates that the

method of plotting modal masses to determine the number of parameters and Fourier coefficients is a good strategy.

2.3.2 Nonlinear Bistable Beam

In the bistable beam experiment, one magnet is embedded in the tip mass, and a second magnet is attached to the platform. Figure 2.6 shows the experimental setup for the bistable beam. A single harmonic acceleration was applied in three different experiments at frequencies of 5, 6, and 7 hz. In each experiment the forcing frequency remained constant while 5×10^5 data points were acquired. The following analysis was restricted to the first beam mode, since the second mode has a frequency over 100 hz and was not excited.

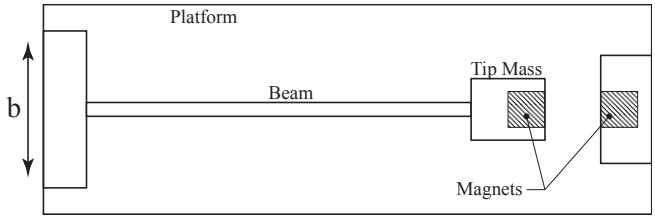

FIGURE 2.6: Top view of the experimental setup of the nonlinear beam with base acceleration b. One magnet is attached to the tip mass of the beam, and the second is fixed to the moving base.

To determine the required number of parameters and Fourier coefficients for the bistable beam, the same 3D plotting method presented in the Weakly Nonlinear Beam section was used. For each of the three frequencies, four to seven parameters and four to ten Fourier coefficients were plotted. Convergence was again taken to be the smallest number of parameters and Fourier coefficients where the plot flattened out.

In Table 2.3 the forcing frequency, the amplitude at which the base was forced, the identified modal mass, the identified damping, and the number of Fourier coefficients and parameters required for convergence are listed for each experiment. The drop

in damping with frequency suggests that the system contains hysteretic damping. Hysteretic damping can be modeled by

$$c(\omega) = \frac{\eta}{|\omega|} \tag{2.12}$$

where η is a damping coefficient for constant hysteretic damping (Gaul et al., 1985). Using a linear fit, the damping for the bistable beam was found to be $\mu = 0.19\ \frac{\text{N·s}}{\text{kg·m}}$ for the viscous damping and $\eta = 132\ \frac{\text{N}}{\text{kg·m}}$ for the hysteretic damping. The overall damping was assumed to be constant at each driving frequency, while the effect of the hysteretic damping is important for changes in driving frequencies. The restoring force coefficients identified from the 5 hz experiment were $\beta_0 = 0.17$, $\beta_1 = -2090$, $\beta_2 = 1671$, $\beta_3 = 8.36 \times 10^8$, and $\beta_4 = -2.44 \times 10^9$. The fifth coefficient β_5 was about -3, but it did not appreciably affect the simulation and was therefore discarded.

Table 2.3: Parameters identified for the bistable beam.

Freq. [hz]	Acc. Amp. $[\frac{\text{m}}{\text{s}^2}]$	Modal Mass	Damping $[\frac{\text{N/kg}}{\text{m/s}}]$	Coeff./ Param.
5	4.32	4.94	4.43	7/5
6	4.05	5.02	3.59	6/5
7	2.32	4.79	3.25	6/5

To determine if the identified parameters accurately model the system, frequency sweeps were compared between the experimental data and simulations using the parameters identified above. Both the physical system and simulations were swept forward (5 to 50 hz) and backward (50 to 5 hz) at constant amplitudes of 2.0 and 3.0 m/s^2. In the following plots, only the frequencies up to 20 hz are presented to provide a more convenient comparison since no significant change in response occurred between 20 and 50 hz. In each figure the response is plotted vs. the frequency with all data points given by gray lines and the response at the peak of the forcing amplitude given by black dots.

The results from the 2.0 m/s^2 amplitude sweeps are shown in Fig. 2.7. Little hysteresis is apparent at this amplitude, and the simulations show good agreement with the experimental results. The response in the backward sweep has a slightly larger amplitude for both the experimental data and simulation when compared to the forward sweep.

The results from the 3.0 m/s^2 amplitude sweeps are shown in Fig. 2.8. The forward sweep simulation shows good agreement with the experimental results. However, the backward experimental sweep end in a stable high amplitude response at frequencies below the region of chaos. While the simulation shows agreement with the frequency ranges, this high amplitude response is not predicted by the simulation. This discrepancy is likely due to coexisting solutions at the lower frequencies.

2.4 Reduced Phase Space

It is of interest to determine what regions of the phase space must be visited by the system to accurately identify the parameters. In the case of HBID and double-well systems, Yasuda et al. (1988b) successfully identified parameters for a response that traversed both wells. However, if data is only available from small oscillations in either one or both wells, it would be advantageous to know if such data could be relied upon to accurately identify the parameters of the system.

For the system described in Section 2.1.3, simulations were run with small oscillations contained in either well, and parameters were estimated using HBID. Plots of the restoring force parameters estimated using HBID are compared to the actual restoring force of the model in Fig. 2.9. Using data that consists of small oscillations within a single well provides a good estimate of the restoring force locally but fails to provide a good estimate of the restoring force globally. However, if data from both wells is combined into a single data set, then a good estimate of all the parameters

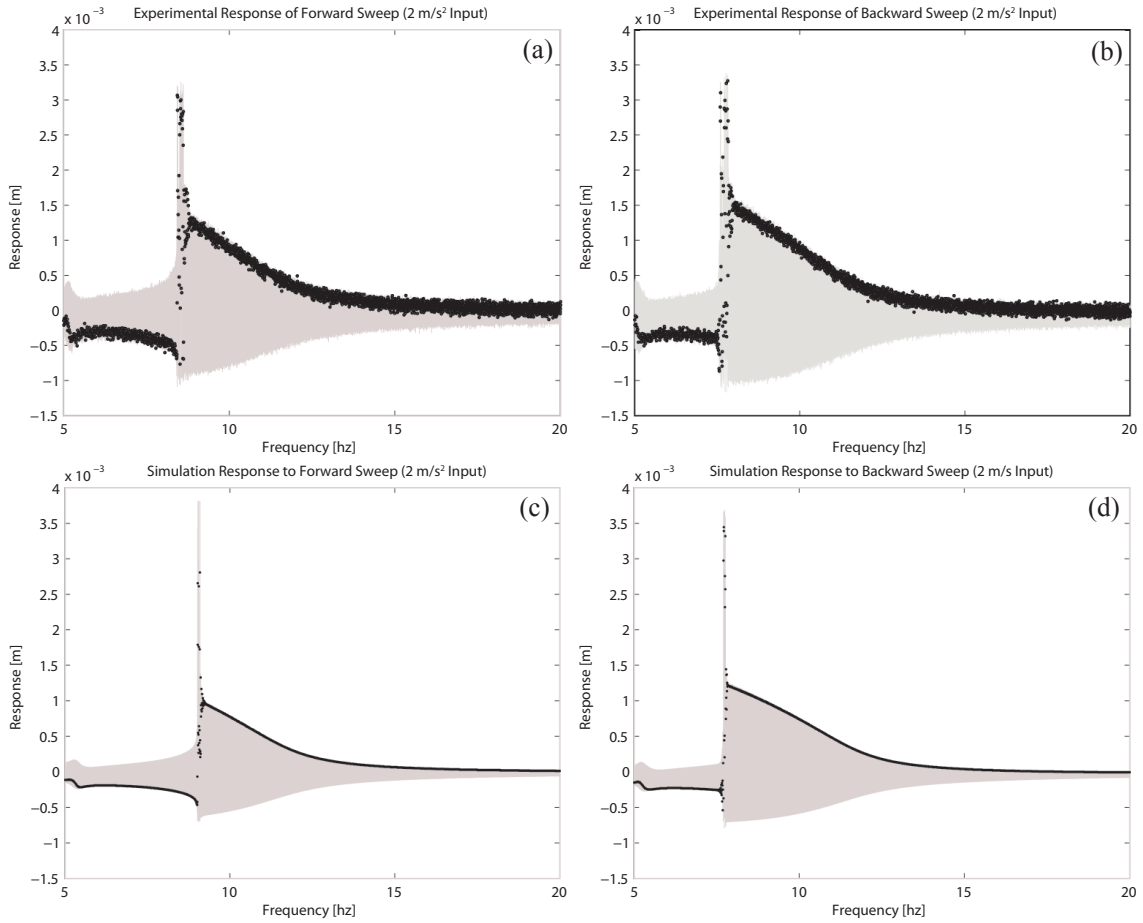

FIGURE 2.7: Bistable beam response for forward (5 to 20 hz) and backward (20 to 5 hz) sweeps with a amplitude of 2.0 m/s^2. The dots show the response at the peak of the platform acceleration. Experimental results for forward and backward sweeps are shown in graphs (a) and (b), respectively. Simulation results for forward and backward sweeps are shown in graphs (c) and (d), respectively.

results. In this chapter, this combined data set will be referred to as a hybrid data set. The total normalized error for the hybrid data shown in Fig. 2.9 is 0.019 which is an excellent fit.

To generate the hybrid data set, an equal number of data points were arbitrarily selected from both single well data sets and added without windowing. The effect of noise on this hybrid data set is explored in Section 2.6.3. It should be noted that the hybrid data set will be more sensitive to noise in general because the amplitude

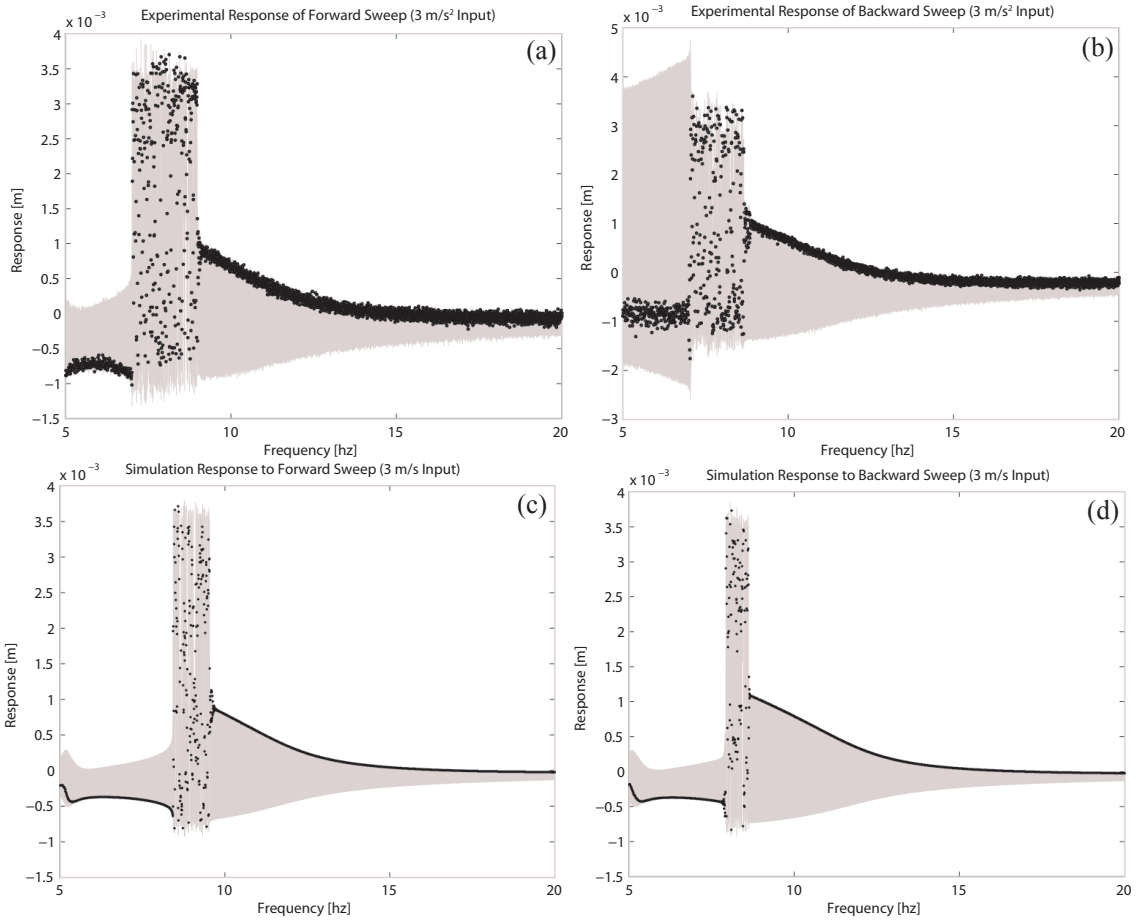

FIGURE 2.8: Bistable beam response for forward (5 to 20 hz) and backward (20 to 5 hz) sweeps with a magnitude of 3.0 m/s^2. Experimental results for forward and backward sweeps are shown in graphs (a) and (b), respectively. Simulation results for forward and backward sweeps are shown in graphs (c) and (d), respectively.

of the responses are smaller than those in the full amplitude data set.

2.5 Weighting Matrix Approach

In the typical implementation of the HBID method, an identity weighting matrix is used to equally weight all harmonics. However, the accuracy of the HBID method can be improved by constructing a weighting matrix that takes advantage of knowledge about the variance of the noise. This section introduces the exponential and SNR weighting matrices and the approach taken to compare the weighting matrices.

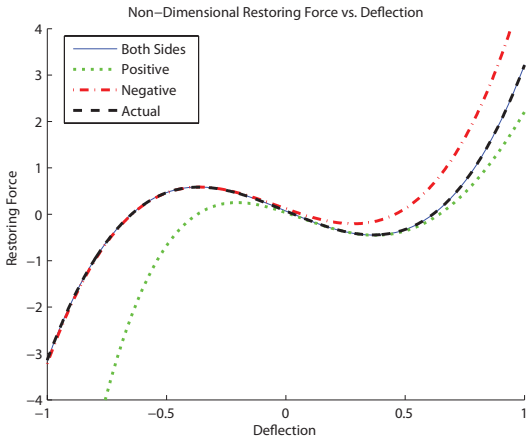

FIGURE 2.9: Comparison of normalized restoring force identified using parameters identified with small oscillations in the positive well (dot), negative well (dash-dot), hybrid data (solid), and the actual parameters (dash).

2.5.1 Weighting Matrices

A typical weighting strategy for the Least Squares Estimator (LSE) is to weight each observation by the inverse of the variance. Using this weighting scheme, the LSE becomes the Best Linear Unbiased Estimator (BLUE), and if the noise is Gaussian, the LSE becomes the Minimum Variance Unbiased (MVU) estimator (Kay, 1993). However, the HBID method cannot be improved using this weighting scheme for two reasons. First, the forcing Fourier coefficients are calculated from the same time series, and therefore, the variances of the Fourier coefficients are equal (Balogh et al., 2002). The position Fourier coefficients are similarly calculated from a single time series. In the case of equal weights for all observations, the weighting matrix becomes equivalent to the identity matrix and reduces to an unweighted LSE. Second, the variances of the position Fourier coefficients associated with each restoring force parameter are not the same. This difference in variance occurs because the Fourier coefficients are calculated by raising the time series to the corresponding power before taking the FFT.

Therefore, a different weighting strategy is required if the HBID method is to be

improved. Two strategies were chosen that weight observations based on the magnitude of the response at the respective observation harmonic. The typical analytical methods to determine estimator performance quickly becomes intractable. Therefore, it is necessary to compare the weighting strategies using a numerical method. The identity matrix and a weighting matrix with randomly generated weights were selected to be the baselines for the comparison.

The first weighting scheme selected was an exponential decay. While identifying parameters from a physical system using HBID, it was found empirically that using an exponential weighting strategy improved the consistency of the identified parameters from one set of data to another. The exponential weighting strategy weights the first harmonic at unity and reduces the weight exponentially to $e^{-1/\tau}$ at the last harmonic; a value of $1/\tau = 6$ was chosen for the comparisons in this chapter. It is supposed that this weighting strategy improves the performance of the HBID method by weighting the lower harmonics, which are expected to have a larger Signal to Noise Ratio (SNR), greater than the higher harmonics which are expected to have a smaller SNR.

The second weighting scheme is referred to as the SNR method. The SNR method uses the square root of the SNR of each harmonic and normalizes the results with the largest SNR. The SNR method is a further improvement in that weights are based on the relative SNRs of the response at each harmonic. The SNR method was developed because it was suspected that harmonics with low SNRs reduce the accuracy of the HBID method. The method used to determine the SNR of each harmonic is included in the following section.

2.5.2 Noise and Errors

Gaussian, uniform, and Laplacian noise were selected to add to the simulated data. Gaussian and uniform noise are commonly encountered in physical systems. Least squares estimates of Fourier coefficients in Laplacian noise will over-estimate the

variance by a factor of two (van den Bos, 1989). It is therefore expected that performance of the the SNR weighting matrix will be most affected by the Laplacian noise. For each noise distribution, the noise is added to the position response of the simulated data.

For experimental data, the variance of the data may not be know in advance. The SNR weighting matrix was chosen in this experimental vein assuming the variance was unknown a priori. In order to determine the SNR matrix, the variance of the simulated data must was estimated using the long series approach taken by Balogh et al. (2002). In this approach, the entire data series is used, and the variance of the Fourier coefficients are given by:

$$\hat{\sigma^2} = \frac{1}{2((M/2-1)-2K)} \sum_{m=1,m\neq k}^{M} |X_m|^2 \,, \tag{2.13}$$

where M is the total number of data points, K is the number of signal channels, X_m are the Fourier coefficients, and k are the indexes of the signal channels (Balogh et al., 2002). An iterative approach was taken to implement the variance calculation. The initial variance was calculated using all channels, but subsequent variance calculations were performed with the signal channels (X_k) removed. Channels with a magnitude greater than three times the standard deviation were identified as signals. The overall variance of the times series is given by $\sigma^2 = \hat{\sigma}^2(2((M/2-1)-2K)$. The SNR of each harmonic can then be calculated by finding the magnitude of the Fourier coefficients, the overall variance, and the following equation:

$$\mathrm{SNR}_n = \frac{|X_n|^2}{2\sigma^2} \,, \tag{2.14}$$

where SNR_n is the SNR of the n^{th} harmonic. The SNR weighting matrix is created by taking the square root of the SNRs of each harmonic and normalizing by the largest SNR.

For each noise and variance, a Monte Carlo simulation was performed using 1000 unique noise vectors. The parameters were determined using the same noise vectors for each of the four weighting matrices. In order to determine the best weighting matrix for a particular noise and variance, the following error norm was selected

$$E_p = \frac{1}{\sqrt{2+P+1}}\sqrt{\left(\frac{m_e - m}{m}\right)^2 + \left(\frac{\mu_e - \mu}{\mu}\right)^2 + \sum_{p=0}^{P}\left(\frac{\beta_{pe} - \beta_p}{\beta_{pe}}\right)^2}, \tag{2.15}$$

where m_e is the actual mass, μ_e is the actual damping, β_{pe} is the actual p^{th} restoring force coefficient, and $P+1$ is the total number of restoring force coefficients. The total error norm for all the simulations could be calculated by first averaging the parameters from all the simulations. However, the error norms from each of the simulations were chosen to determine the overall error norm. This choice reflects the reality that parameters are most likely to be determined by a few sets of data rather than averaging a large number of data sets. This choice also means that the variance of the calculated parameters is equally as important as the magnitude of the error. For example, if only one set of data is available, the weighting matrix with the lowest variance may provide the best estimate of the parameters.

2.5.3 Propagated Uncertainty

An alternative method to determine the affect of the weighting matrices on the performance of the HBID is error propagation. The change in the error can then be compared for HBID implementations using each of the proposed weighting matrices. The weighting matrix that results in the lowest error is expected to be the best option for identifying the parameters. Typically, one of the benefits of using an error propagation method is an analytical expression between error and the standard error of the data. However, the HBID method is too complex to result in an analytical expression. The functional approach for error propagation was used instead which

is given by

$$\alpha_z = \left| f(\bar{A} + \alpha_A) - f(\bar{A}) \right| , \tag{2.16}$$

where α_z is the propagated standard error of the function, $\bar{A}$ is a given measurement, and α_A is the standard error of the data (Hughes and Hase, 2010). When implemented for the HBID method, α_z is the standard deviation of each parameter, $\bar{A}$ is a vector of the parameters, and α_A is the standard deviation of the noise. The choice of standard deviation rather than standard error follows the choice to average error means as mentioned in Sec. 2.5.2. For Fourier coefficients of the time series taken to a power, the standard deviation of the associated power must be used. A Gaussian distribution was chosen for the error propagation, but the same calculation can be made for both the uniform and Laplacian distributions.

Figure 2.10 provides a comparison of the propagated variance using the identity, exponential, and SNR weighting matrices. For each weighting matrix, the standard deviation of the parameters for each SNR was calculated using Eq. (2.16). The standard deviation of the total error was calculated by inserting the standard deviation of the parameters into the error norm of Eq. (2.15). Figure 2.10 indicates both the exponential and SNR weighting schemes are clearly expected to improve the performance of the HBID method.

2.6 Weighting Matrix Simulations

Each of the results in the following sections were generated from the base excited system parameters given in Section 2.1.3. Simulations were sampled at a rate of 1000 Hz and were run for 500 seconds before reordering data to ensure steady state conditions. In each case, the forcing period was 0.2 seconds. Simulations were run without noise, and separately generated noise vectors were added to the time data before the HBID method was applied. For each run, a new noise vector was generated

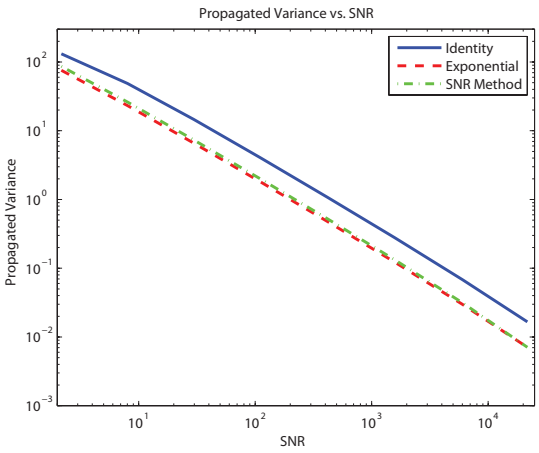

FIGURE 2.10: Comparison of the propagated variance using identity (solid), exponential (dash), and SNR Method (dash-dot) weighting matrices in Gaussian noise vs. the SNR.

and added to the simulated data and a new Random weighting matrix was generated. The four weighting matrices were applied in the HBID method on each noise vector.

2.6.1 Increased Noise

This section describes the analyses using increasing amplitudes of Gaussian, uniform, and Laplacian noise. The same simulation data was used for each data point, and the response visited both wells. The simulation had a duration of 500 seconds and a forcing amplitude of $|\ddot{z}| = 4.6$. Each analysis includes a set of 1000 HBID runs for eight different standard deviations. The same standard deviations are used for each noise distribution and are listed in Table 2.4.

The total normalized error and its variance for Gaussian noise are given in Fig. 2.11. In graph (a) the normalized error defined by Eq. (2.15) is plotted for parameters identified by each of the four weighting matrices. As expected the errors using the random weighting matrix are much larger than the other weighting matrices. Both the exponential and SNR weighting matrices show a clear improvement over the identity weighting matrix with the SNR scheme providing the best perfor-

Table 2.4: Standard deviations used for each noise distribution analysis. The SNR is calculated using the first harmonic which has an amplitude of 0.002083.

Std. Dev.	1.0×10^{-3}	5.2×10^{-4}	2.7×10^{-4}	1.4×10^{-4}
SNR	2.2	8.0	30	110

Std. Dev.	7.2×10^{-4}	3.7×10^{-5}	1.9×10^{-5}	1.0×10^{-5}
SNR	420	1,600	6,000	22,000

mance. The variance results in graph (b) also demonstrate that the SNR scheme improves the performance over the other weighting matrices.

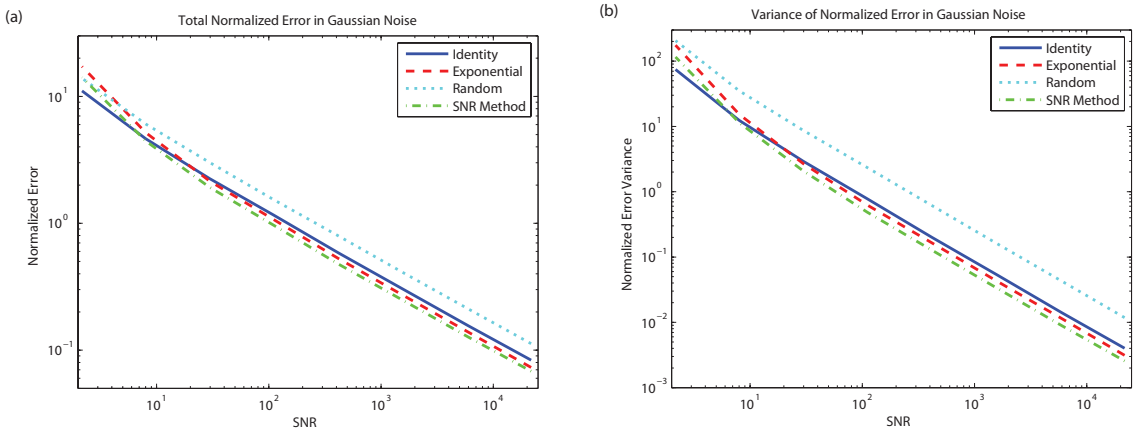

FIGURE 2.11: Comparison of identity (solid), exponential (dash), random (dot), and SNR Method (dash-dot) weighting matrices in Gaussian noise. Graph (a) shows the total normalized error for each weighting matrix vs. the SNR, and graph (b) shows the variance vs. the SNR.

Figure 2.12 provides a breakdown of the normalized error of the mass, damping, and combined restoring force parameters in Gaussian noise. While the SNR weighting matrix has a superior performance for the overall normalized error, the identity weighting matrix has lower errors for the damping and the mass at large SNRs. However, the error associated with the restoring force is much larger than either the mass or the damping, and therefore the restoring force error drives the overall

error. As with the total error, the SNR weighting matrix estimates restoring force parameters with the lowest average error of all four weighting matrices. The results of the Gaussian analysis for mass, damping, and restoring force are representative of the other noise distributions.

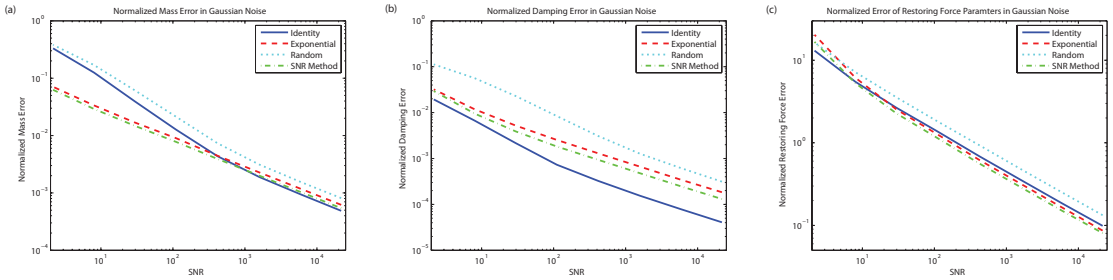

FIGURE 2.12: Comparison of identity (solid), exponential (dash), random (dot), and SNR Method (dash-dot) weighting matrices in Gaussian noise. Graph (a) shows the normalized error for the mass parameter for each weighting matrix, graph (b) shows the normalized error for the damping parameter for each weighting matrix, and graph (c) shows the total normalized error for the restoring force parameters.

Since the largest component of the total error is due to the restoring force parameters, examining these parameters in more detail will provide insight into what total error is acceptable. Figure 2.13 compares nondimensionalized restoring force curves for the four largest sets of Gaussian noise with the actual parameters. The restoring force curves were generated by averaging the parameters estimated using the SNR weighting scheme, non-dimensionalizing the parameters, and plotting 1000 points. For the non-dimensional analysis, $L = 0.0025$ was chosen for the length and $\omega = 2\pi/0.2$ for the frequency. Two interesting discoveries are made by observing Fig. 2.13. First, total normalized error of about two or less is a reasonable level of error. Second, the initial relative fluctuations of total error between the different weighting matrices is due to inaccuracies in the estimated parameters with normalized errors greater than two. Therefore, when comparing the results of the weighting schemes, accurate comparisons can only be made for normalized errors of about two or less. In the case of Fig. 2.11, the comparison is valid for SNRs of about 30 or

greater (standard deviations of 2.7×10^{-4}).

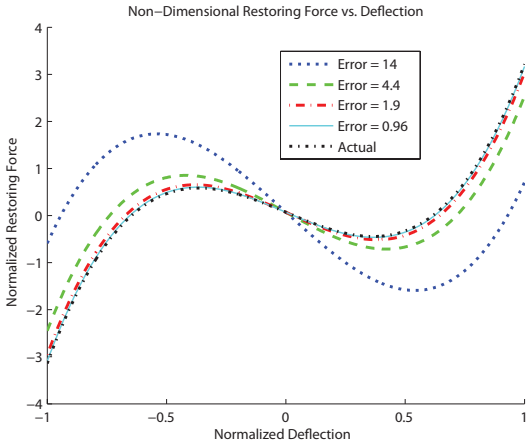

FIGURE 2.13: Comparison of the average non-dimensional restoring force parameters in Gaussian noise identified using the HBID method with the SNR weighting matrix and the actual non-dimensional parameters. The non-dimensional analysis was performed using $L = 0.0025$ for the length and $\omega = 2\pi/0.2$ for the frequency. The errors correspond to the four largest levels of noise from Table 2.4.

The total normalized error and its variance for uniform noise are given in Fig. 2.14. In graph (a) the normalized error is plotted for parameters identified by each of the four weighting matrices. The results are similar to the Gaussian noise, and as expected the errors using the random weighting matrix are much larger than the other weighting matrices. Both the exponential and SNR weighting matrices show a clear improvement over the identity weighting matrix with the SNR weighting scheme providing the best performance. The variance results in graph (b) also demonstrate that the SNR weighting scheme improves the performance over the other weighting matrices. Comparisons are valid for SNRs of about 30 and greater.

The total normalized error and its variance for Laplacian noise are given in Fig. 2.15. In graph (a) the normalized error is plotted for parameters identified by each of the four weighting matrices. It might be expected that the performance of the SNR weighting would be negatively affected by the Laplacian distribution since the variance calculations from the noisy data will be over estimated. However,

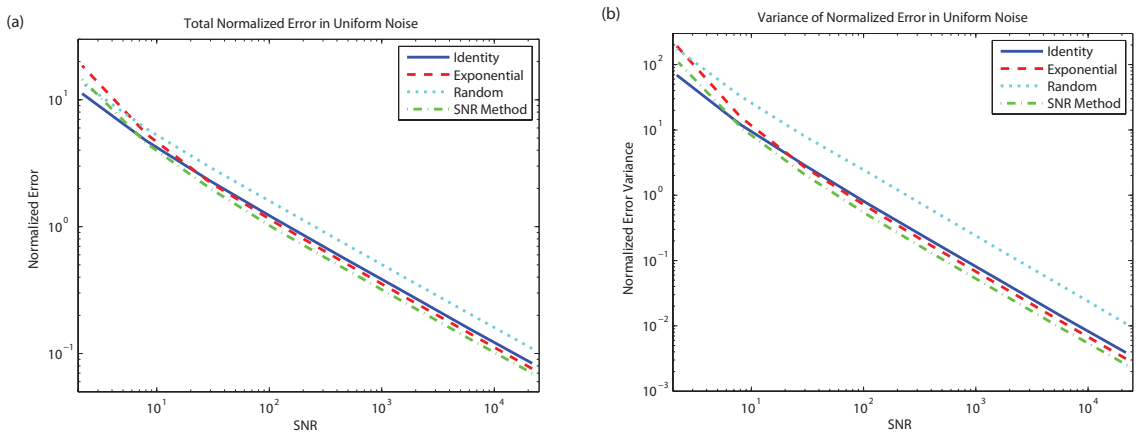

FIGURE 2.14: Comparison of identity (solid), exponential (dash), random (dot), and SNR Method (dash-dot) weighting matrices in uniform noise. Graph (a) shows the total normalized error for each weighting matrix vs. the SNR, and graph (b) shows the variance vs. the SNR.

no significant changes are observed from the Gaussian and uniform noise results. As expected the errors using the random weighting matrix are much larger than the other weighting matrices. Both the exponential and SNR weighting matrices show a clear improvement over the identity weighting matrix with the SNR weighting scheme providing the best performance. The variance results in graph (b) also demonstrate that the SNR weighting scheme improves the performance over the other weighting matrices. Comparisons are valid for SNRs of about 30 and greater.

2.6.2 Reduced Data Set

This section describes the result of reducing the number of data points in Gaussian noise. The additive Gaussian noise in each set of Monte Carlo runs has a standard deviation of 1.4×10^{-4} which corresponds to an SNR of 110. This level of noise was selected because it is the value for which the identity, exponential, and SNR weighting matrices all generate normalized errors of less than two. The number of data points in each reduced data set is given in Table 2.5. The simulated data points were acquired from the same data used in Section 2.6.1. The number of Monte

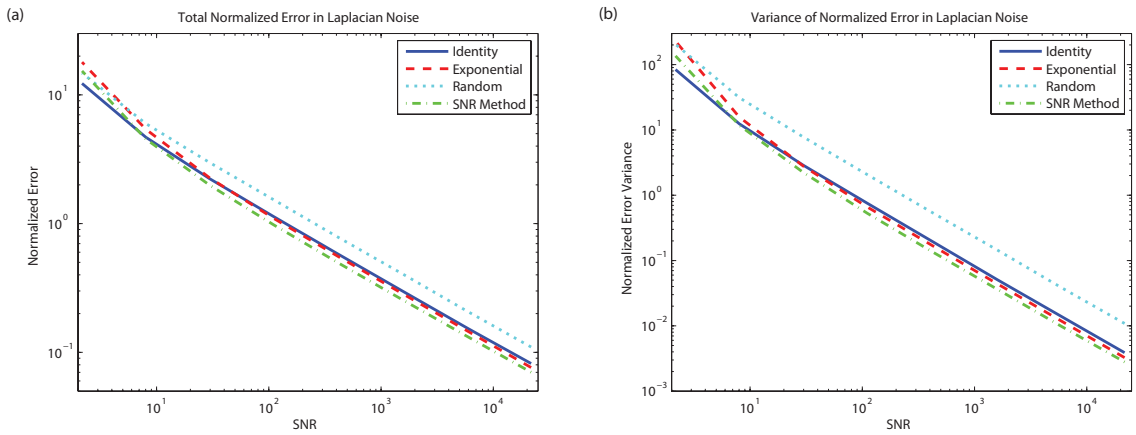

FIGURE 2.15: Comparison of identity (solid), exponential (dash), random (dot), and SNR Method (dash-dot) weighting matrices in Laplacian noise. Graph (a) shows the total normalized error for each weighting matrix vs. the SNR, and graph (b) shows the variance vs. the SNR.

Carlo runs for each reduced data set was chosen so that the number of data points multiplied by the number of runs were all equal to 5×10^8.

Table 2.5: Number of cycles, simulated data points, and Monte Carlo runs for each data set. Each forcing period (cycle) has a total of 200 data points.

No. of Cycles	2,500	1,250	625	313	156	78
No. of Data Points	500,000	250,000	125,000	62,500	31,250	15,625
Monte Carlo Runs	1,000	2,000	4,000	8,000	16,000	32,000

The total normalized error and its variance for the reduced Gaussian noise data sets vs. the number of cycles used are given in Fig. 2.16. In graph (a) the normalized error is plotted for parameters identified by each of the four weighting matrices. For a low number of cycles (less than about 400), the error is large (greater than two) and the parameters cannot be identified with any of the weighting schemes. At larger cycles (greater than about 600), the parameters can be identified and the SNR weighting is the best option of the four. The variance results in graph (b) also demonstrate that the SNR scheme improves the performance over the other

weighting schemes.

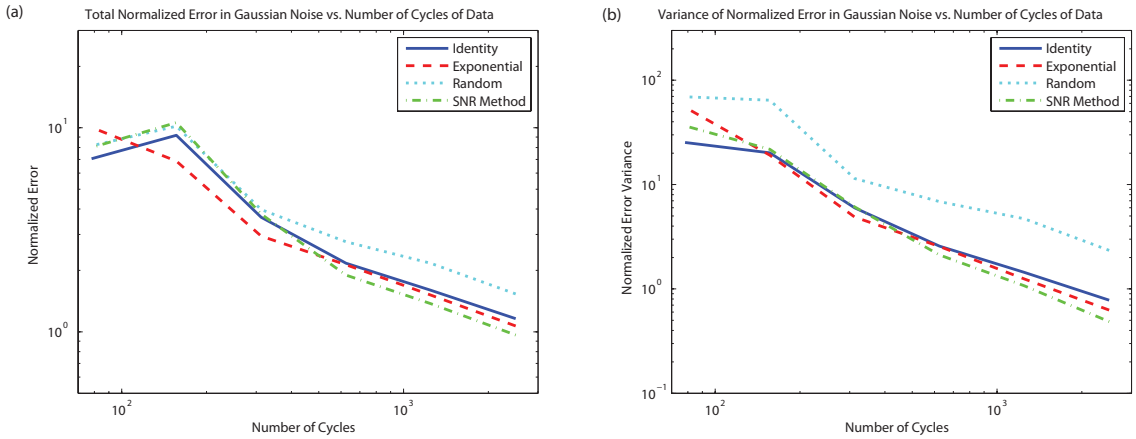

FIGURE 2.16: Comparison of identity (solid), exponential (dash), random (dot), and SNR Method (dash-dot) weighting matrices in Gaussian noise for an increasing number of data points. Graph (a) shows the total normalized error for each weighting matrix vs. the SNR, and graph (b) shows the variance vs. the SNR. The sample rate was 200 data points per cycle and Gaussian noise had a standard deviation of 1.4×10^{-4} which corresponds to an SNR of 110.

2.6.3 Reduced Phase Space

This section describes the results of using Gaussian noise and reduced phase space simulations. The simulation data is the hybrid data set consisting of two separate simulations arbitrarily combined. Both simulations have a duration of 250 seconds, a forcing amplitude of $|\ddot{z}| = 1.5$, and a response that remains within its respective well. Increasing levels of Gaussian noise were added, and the parameters were estimated using the identity, exponential, random, and SNR weighting matrices.

The reduced phase space analysis consists of a set of 1000 HBID runs in Gaussian noise for the eight different standard deviations which are listed in Table 2.6. It should be noted that while the SNRs used for this analysis are similar to the full response, the standard deviation of the noise is less than the full response. Therefore, using a reduced phase space will be more sensitive to noise than data which transverses a larger portion of the phase space.

Table 2.6: Standard deviations used for the Monte Carlo runs for the reduce phase space analysis. The SNR is calculated using the first harmonic which has an amplitude of 9.614×10^{-5}.

Std. Dev.	5.0×10^{-5}	2.6×10^{-5}	1.3×10^{-5}	6.9×10^{-6}
SNR	1.8	6.8	27	97

Std. Dev.	3.6×10^{-6}	1.9×10^{-6}	9.7×10^{-7}	5.0×10^{-7}
SNR	360	1,300	4,900	18,000

The total normalized error and its variance for Gaussian noise in the reduced phase space are given in Fig. 2.17. In graph (a) the normalized error is plotted for parameters identified by each of the four weighting matrices. As expected, the errors using the random weighting matrix are much larger than the other weighting matrices. Both the exponential and SNR weighting matrices show a clear improvement over the identity weighting matrix which is consistent with the other analyses. However, instead of the SNR weighting providing the best performance, the exponential method results in a nearly identical improvement in performance. The variance results in graph (b) also demonstrate that the exponential and SNR weightings improve the performance over the identity weighting matrix equivalently.

In order to understand why the SNR weighting improves performance over the exponential weighting for the full phase space but not for the reduced phase space, the Fourier coefficients of both time series must be examined. In Fig. 2.18 the Fourier coefficients of the full and reduced phase space are plotted for the first seven harmonics along with the exponential weighting. For the full phase space, the exponential weighting strategy weights the second harmonic more than the third even though the magnitude of the the second harmonic is relatively small. If harmonics with low SNRs reduce the overall accuracy of the HBID method, one would expect the

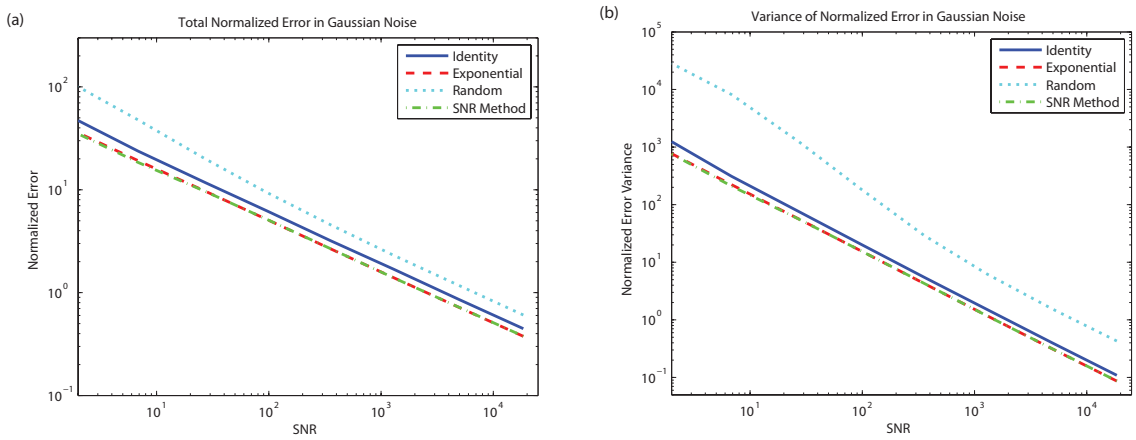

FIGURE 2.17: Comparison of identity (solid), exponential (dash), random (dot), and SNR Method (dash-dot) weighting matrices in Gaussian noise for a reduced phase space. Graph (a) shows the total normalized for each weighting matrix vs. the SNR, and graph (b) shows the variance vs. the SNR. The data is a hybrid combination of small responses about each well.

SNR weighting scheme to be superior to the exponential weighting scheme in this case since the SNR matrix greatly reduces the influence of the second harmonic. In the case of the reduced phase space, both the exponential and SNR methods weight the first and second harmonics greater than the remaining harmonics. Since both weighting schemes produce similar weighting matrices for this second case, it makes sense that both schemes result in a similar improvement of performance over the identity matrix. These two results tend to confirm the premise that harmonics with low SNRs reduce the overall accuracy of the HBID method.

2.7 Conclusions

This chapter presents experimentally identified parameters of a weakly nonlinear, base excited, beam energy harvester. In order to identify parameters for a weakly nonlinear system, a method to incorporate multiple concurrent forcing frequencies was demonstrated. In addition, an experimental approach to determine the number of restoring force coefficients (parameters) and Fourier coefficients required for con-

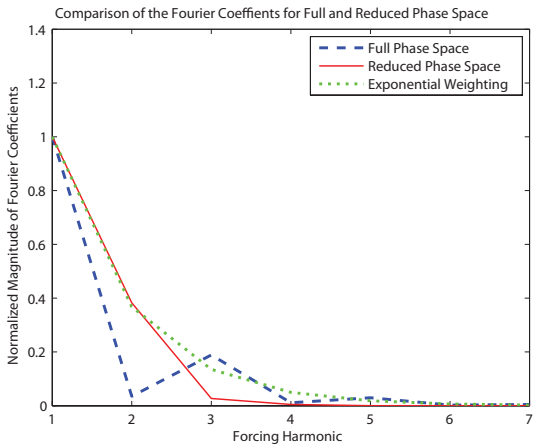

FIGURE 2.18: Normalized amplitudes of the Fourier coefficients of the full and reduced phase space for the first seven harmonics. The exponential weighting is overlayed for comparison. The SNR weighting is proportional to the harmonics for both data sets.

vergence was introduced. This method is comprised of plotting the modal mass for different combinations of parameters and Fourier coefficients. Combinations where no significant change in modal mass occurred were selected when the number of parameters and Fourier coefficients were increased. This method successfully identified the number of duffing parameters for the weakly nonlinear system.

Then, the experimentally identified parameters of a nonlinear, bistable, base excited beam energy harvester were presented. The number of the restoring force coefficients was determined using the same method introduced for the weakly nonlinear energy harvester. The accuracy of the parameters identified were demonstrated by comparing frequency sweeps of both simulations and experimental data.

Next, this chapter compared the effects of weighting matrices on the accuracy of parameter estimation using the HBID method. The exponential and SNR weighting strategies were introduced and compared with the baseline identity and random schemes for accuracy in identifying parameters. Parameters using all four schemes were compared for increasing noise levels in Gaussian, normal, and Laplacian distri-

butions. In addition, the four schemes were compared for reduced number of forcing cycles and for a reduced phase space.

In each of the increasing noise simulations, the identified parameters using the SNR weighting scheme were found to have the best accuracy for all three noise distributions. The exponential scheme was also found to have improved the accuracy of the identified parameters over the baseline schemes. The maximum normalized error for accurately identified parameters was about two. To further compare the different weighting schemes, Table 2.7 lists the maximum standard deviation of the noise for which each weighting scheme produced a normalized error of two. The associated minimum SNR required by each weighting scheme was also included. The comparison demonstrates that the SNR weighting scheme reduces the minimum required SNR between 19% to 26% compared to the identity weighting matrix.

Table 2.7: Comparison of the maximum level of noise allowable and minimum SNR required for each weighting matrix in Gaussian, Laplacian, and uniform noise corresponding to a normalized error of two. The standard deviations of the noise and associated SNRs were interpolated from the data plotted in Figs. 2.11, 2.14, and 2.15.

	Weighting	Error	Std. Dev.	SNR
Gaussian	Identity	2	2.40×10^{-4}	38
	Exponential	2	2.52×10^{-4}	34
	Random	2	1.81×10^{-4}	66
	SNR	2	2.78×10^{-4}	28
Uniform	Identity	2	2.36×10^{-4}	39
	Exponential	2	2.44×10^{-4}	37
	Random	2	1.84×10^{-4}	64
	SNR	2	2.70×10^{-4}	30
Laplacian	Identity	2	2.43×10^{-4}	37
	Exponential	2	2.40×10^{-4}	38
	Random	2	1.82×10^{-4}	65
	SNR	2	2.71×10^{-4}	30

For the reduced number of data points comparison, the SNR weighting scheme again was found to improve the accuracy of the identified parameters over the other weighting schemes. The exponential scheme also improved the accuracy of the identified parameters over the baseline schemes. To further contrast the different weighting schemes, Table 2.8 lists the minimum number of cycles for which each weighting scheme produces a normalized error of two. The comparison in the table demonstrates that the SNR weighting scheme reduces the required number of forcing cycles by 33% over those estimated using the identity weighting matrix.

Table 2.8: Comparison of minimum number of forcing cycles for each weighting matrix in Gaussian noise which corresponds to a normalized error of two. The minimum number of cycles were interpolated from the data in Fig. 2.16.

Weighting	Error	Cycles
Identity	2	810
Exponential	2	759
Random	2	1580
SNR	2	608

Finally, this chapter explored whether the HBID method can identify parameters using a reduced phase space which has received little attention in the literature. Parameters were identified for simulations in which the response remained in either of the two wells of the system. It was found that the restoring force parameters identified from either well did not accurately model the global behavior of the system. However, when time series data from both wells were arbitrarily combined, the identified parameters accurately identified the restoring force parameters of the simulation. Subsequently, Gaussian noise was added to the combined time series to compare the four weighting schemes. As in the other comparisons, the SNR weighting scheme improved the accuracy of the identified parameters over the baselines. Unexpectedly, the exponential weighting scheme performed equally as well as the

SNR scheme. It was shown based on the Fourier coefficients, that the reduced phase space simulation was a unique case in which the both SNR and exponential weighting schemes produce nearly equivalent weighting matrices. Therefore, this results is consistent with the premise that harmonics with low SNRs reduce the overall accuracy of the HBID method. In addition, it should be noted that arbitrarily adding time series data is the worst case scenario. Windowing the data or other strategic choices may further improve this method.

3

Minimizing error in the logarithmic decrement method

Early descriptions of the logarithmic decrement method date back to at least 1860 in viscosity experiments performed by Helmholtz and Piotrowski (Whetham, 1890). The logarithmic decrement method for estimating friction is now nearly ubiquitous and included in many textbooks (Meirovitch, 2001). The method has been used to estimate structural damping Fang and Lyons (1996), damping in cantilever beams (Liao and Wells, 2011), and plates (Saito and Yaguchi, 1982). Other researchers have used the method to approximate damping in the vibration of heat exchanger tubes (Grover and Weaver, 1978) and turbine blades (Sinha, 2004).

For all the applications of the log decrement method, there appear to be few examples of formal uncertainty analyses of the method in the literature. Kestin and Khalifa (1976) performed an error analysis on the log decrement method when applied to a torsional oscillation. A least squares analysis was performed by Wilcox and Crawford (1968), and the analysis also included estimates such as amplitude. Mezzetti (1979) provided an error analysis of an automated system for determining the log decrement. Missing from all of these analyses is a general uncertainty analysis,

especially regarding the effect of the number of periods used in the calculation. It is intuitive to increase the number of periods between peak measurements to improve the estimate of the period. However, it is not always clear at what point the errors in measuring progressively smaller peaks outweighs the advantage of increasing the number of periods between measurements. In this chapter, the effect of both increasing the number of periods and measurement noise on the uncertainty of the damping ratio are discussed.

The content of this chapter is organized as follows. First, an uncertainty analysis is performed on the log decrement method for uncertainties in the period and measurements of the displacement. Next, dimensionless examples are presented for typical damping ratios and measurement errors. Finally, general conclusions are drawn including a guide in the form of a figure for typical systems.

3.1 Uncertainty Analysis

The equation of motion for a linear oscillator or small oscillations about a nonlinear equilibrium are often represented by

$$\ddot{x} + 2\zeta\omega_n\dot{x} + \omega_n^2 x = 0\,, \tag{3.1}$$

where $x(t)$ is the displacement of the oscillator, ζ is the damping ratio, ω_n is the natural frequency of the system, and the over-dot represents a derivative with respect to time. The logarithmic decrement method is a commonly used method to estimate the damping of systems adequately described by Eq. 3.1. The method presumes the response of a system using the solution to Eq. 3.1 with the form

$$x(t) = A\mathrm{e}^{-\zeta\omega_n t}\cos(\omega_d t - \phi)\,, \tag{3.2}$$

where A is the amplitude of the response, ω_d is the frequency of the damped response, $\omega_d = \omega_n\sqrt{1-\zeta^2}$, and ϕ is the phase shift. Figure 3.1 shows an example of the

typical response of Eq. 3.2 as an oscillation with an exponential decay in the peaks. Throughout this chapter, the system response will be assumed to be dimensionless so that $\omega_n = 1$.

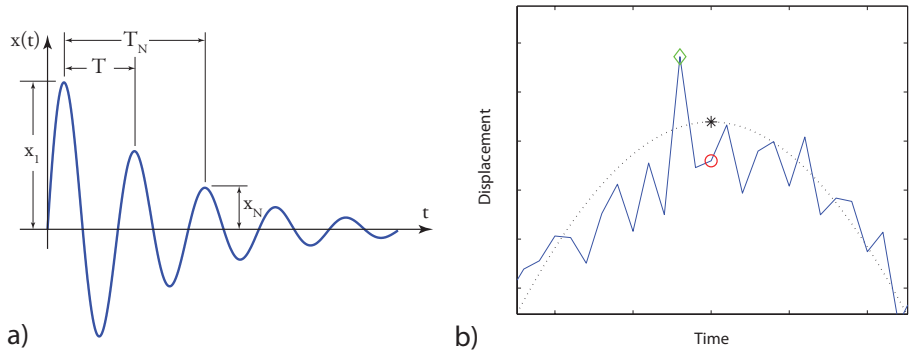

FIGURE 3.1: Figure (a) shows an example of the measurements taken in a logarithmic decrement analysis. In this case the period T_N is twice the damped period T, so $N = 2$. Figure (b) shows the actual response and noisy response as dotted and solid curves, respectively. Points on the actual response (star) and on the noisy response (circle and diamond) are also shown.

The log decrement method relates the damping ζ to the response peaks through

$$\zeta(\delta_N, N) = \frac{(\delta_N/(2\pi N))}{\sqrt{1 + (\delta_N/(2\pi N))^2}}, \tag{3.3}$$

where $\delta_N = \ln(x_1/x_N)$ is the logarithmic decrement, x_1 is the magnitude of the first peak, and x_N is the magnitude of the peak N periods later (Meirovitch, 2001, chap. 2). Figure 3.1(a) provides an example of how the peaks and periods are measured from the data.

Figure 3.1(b) highlights the effect of uncertainty on peak selection. In the figure, the response of the system without noise is shown as a dotted curve, and the peak is indicated by the star. Without noise, the damping can be calculated accurately with a single period ($N = 1$). When noise is added to the measured response, as shown by the solid curve, the point selected as the peak is likely to have error in both the magnitude and period as shown by the diamond. If the error in determining

the peak was due only to displacement uncertainty, the point represented by the circle would be chosen. However, such a selection implies that the period or the location of the peaks are known a priori, which is unlikely. In addition, experimental data is typically discretized in which case the data is frequently not available at the peaks leading to error in the measurement of the period. Therefore, one must contend with uncertainties in both the displacements and period measurements, but the measurements of the period in Eq. (3.3) are implicit. To apply uncertainty propagation, it is necessary to have an explicit representation of the measurements of both amplitude and period. This expression is given by

$$\zeta(x_1, x_N, T, T_N) = \frac{\frac{\ln(x_1/x_N)}{2\pi T_N/T}}{\sqrt{1 + \left(\frac{\ln(x_1/x_N)}{2\pi T_N/T}\right)^2}}, \tag{3.4}$$

where $T = 2\pi/\omega_d$ is the period of the damped vibration and T_N is the duration of the number of damped periods between peaks. Please note that in all of the equations T and T_N correspond to the period of the damped response and not to the period of the natural frequency.

Using uncertainty propagation, the uncertainty of the damping U_ζ is related to the measurements by

$$U_\zeta^2 = \left(\left(\frac{\partial \zeta}{\partial x_1}\right)^2 + \left(\frac{\partial \zeta}{\partial x_N}\right)^2\right) U_x^2 + \left(\left(\frac{\partial \zeta}{\partial T}\right)^2 + \left(\frac{\partial \zeta}{\partial T_N}\right)^2\right) U_T^2, \tag{3.5}$$

where U_x is the uncertainty of the displacement measurement taken as a fraction of the first peak and U_T is the uncertainty of the measured period taken as a fraction

of the period. The partial derivative terms that appear in Eq. 3.5 are given by

$$\left(\frac{\partial\zeta}{\partial x_1}\right)^2 = \frac{16\pi^4 T^2 T_N^4}{x_1^2\left(4\pi^2 T_N^2 + T^2\ln(x_1/x_N)^2\right)^3}\,,$$

$$\left(\frac{\partial\zeta}{\partial T}\right)^2 = \frac{16\pi^4 T_N^4\ln(x_1/x_N)^2}{\left(4\pi^2 T_N^2 + T^2\ln(x_1/x_N)^2\right)^3}\,,$$

$$\left(\frac{\partial\zeta}{\partial x_N}\right)^2 = \frac{16\pi^4 T^2 T_N^4}{x_N^2\left(4\pi^2 T_N^2 + T^2\ln(x_1/x_N)^2\right)^3}\,,\text{ and}$$

$$\left(\frac{\partial\zeta}{\partial T_N}\right)^2 = \frac{16\pi^4 T^2 T_N^2\ln(x_1/x_N)^2}{\left(4\pi^2 T_N^2 + T^2\ln(x_1/x_N)^2\right)^3}\,. \tag{3.6}$$

A great deal can be learned about the sensitivity of the log decrement method to noise by plotting the partials from Eq. (3.6). Plots of the partials versus N are given in Fig. 3.2 for $\zeta = 0.01$ and $\zeta = 0.10$ for a non-dimensional system. In both cases, the ideal number of periods is more than unity, but increasing the number of periods indefinitely does not continue to improve the estimate. This makes sense physically; because as the peaks become smaller, it becomes more difficult to determine where the peak occurs.

3.2 Nondimensional Examples

In this section, the effects of U_x, U_T, and N on the uncertainty of the damping ratio is explored using dimensionless simulations. A damping ratio range of $0.01 \leqslant \zeta \leqslant 0.10$ was chosen since this range is often observed experimentally. A displacement uncertainty range of $0.01 \leqslant U_x \leqslant 0.10$ was chosen for the analysis which is implemented as a fraction of x_1. It should be noted that U_x represents the effects of noise and quantization errors in experimental data. A period uncertainty range of $0.01 \leqslant U_T \leqslant 0.05$ was chosen for the analysis which is implemented as a fraction of T. Both of these ranges represent uncertainties expected to be typically encountered in experiential data.

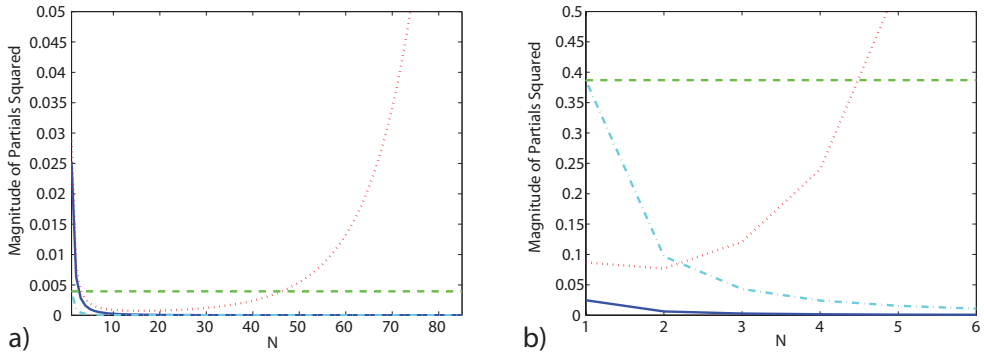

FIGURE 3.2: Magnitude of the partials for Eq. (3.6) are shown for N periods between measurements with $\left(\frac{\partial \zeta}{\partial x_1}\right)^2$, $\left(\frac{\partial \zeta}{\partial x_n}\right)^2$, $\left(\frac{\partial \zeta}{\partial T}\right)^2$, and $\left(\frac{\partial \zeta}{\partial T_n}\right)^2$ as solid, dotted, dashed, and dash-dotted curves, respectively. Plot (a) shows the results for $\zeta = 0.01$, and plot (b) shows the results for $\zeta = 0.10$. In both cases, increasing the number of periods initially provides an improvement, but it actually increases the error in the estimate for too many periods.

For the first analysis, U_T and ζ are held constant, while U_x and N are varied. The uncertainty of the damping ratio is calculated which results in a three-dimensional plot. Figure 3.3(a) shows the lowest U_ζ occurs as a trough, and the uncertainty increases with fewer or with more periods than $N \approx 18$. The trough shape is shown more clearly in Fig. 3.3(b) as three cross-sections cut with constant U_x. It is interesting to note that as U_x decreases, the range of N for minimum U_ζ broadens.

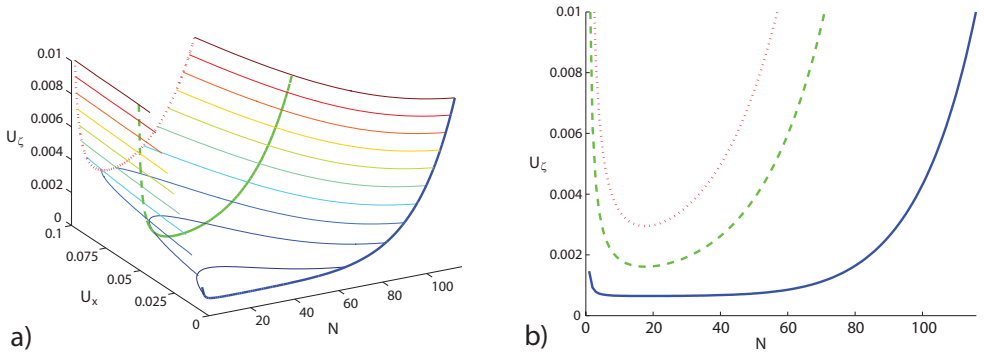

FIGURE 3.3: Magnitude of the damping uncertainty for $\zeta = 0.01$ and $U_T = 0.01$. Plot (a) shows the change in the uncertainty for increasing U_x and N. Plot (b) shows the uncertainty in the damping for $U_x = 0.005$, 0.052, and 0.1 as solid, dashed, and dotted curves, respectively.

Figure 3.4 provides the same plots for a damping ratio of $\zeta = 0.10$. However, in this case the ideal number of periods is either three or four, depending on the magnitude of U_x. To gauge the effect of U_T, the analysis in Figs. 3.3 and 3.4 has been repeated for $U_T = 0.05$, and the cross-section plots are presented in Fig. 3.5 for comparison. Figure 3.5(a) shows the cross-section for $\zeta = 0.01$ and Fig. 3.5(b) shows the cross-section for $\zeta = 0.10$. The increase in U_T raises the damping uncertainty across the board but has only a small impact on the ideal number of periods in each case. It appears that besides N, the damping ratio itself has the largest effect on the ideal number of periods (i.e. N for which U_ζ is minimized).

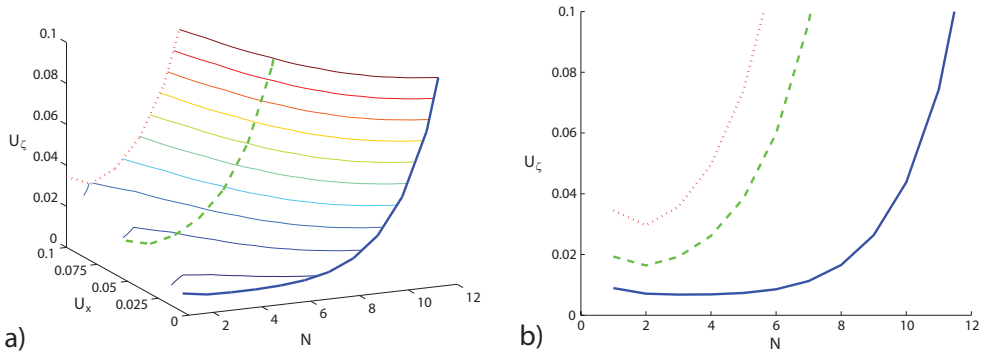

FIGURE 3.4: Magnitude of the damping uncertainty for $\zeta = 0.10$ and $U_T = 0.01$. Plot (a) shows the change in uncertainty for increasing U_x and N. Plot (b) shows the uncertainty in the damping for $U_x = 0.005$, 0.052, and 0.1 as solid, dashed, and dotted curves, respectively.

In order to evaluate the effect of damping on the ideal number of periods, U_x and U_T were held constant, and ζ and N were varied. Figure 3.6(a) shows the resulting U_ζ in a three dimensional plot. Again, a trough is formed with the lowest U_ζ representing the ideal number of periods. The trough shape is more clearly shown in Fig. 3.6(b) with cross-sections cut for three different damping ratios.

Ideally, these observations could be summarized into a single figure. However, since this would require a four dimensional plot, compiling such a representation is not straight forward. The approach used was to generate analyses for a damping

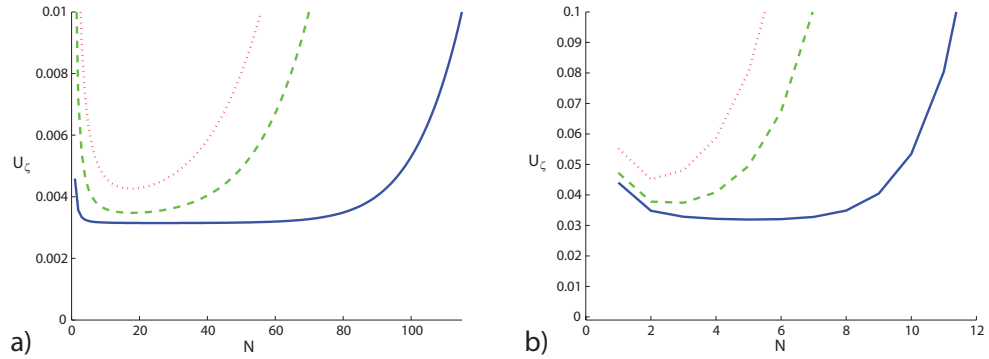

FIGURE 3.5: Magnitude of the damping uncertainty for $U_T = 0.05$. Plot (a) shows the damping uncertainty for $\zeta = 0.01$ and $U_x = 0.005$, 0.052, and 0.1 as solid, dashed, and dotted curves, respectively. Plot (b) shows the damping uncertainty for $\zeta = 0.10$ and $U_x = 0.005$, 0.052, and 0.1 as solid, dashed, and dotted curves, respectively.

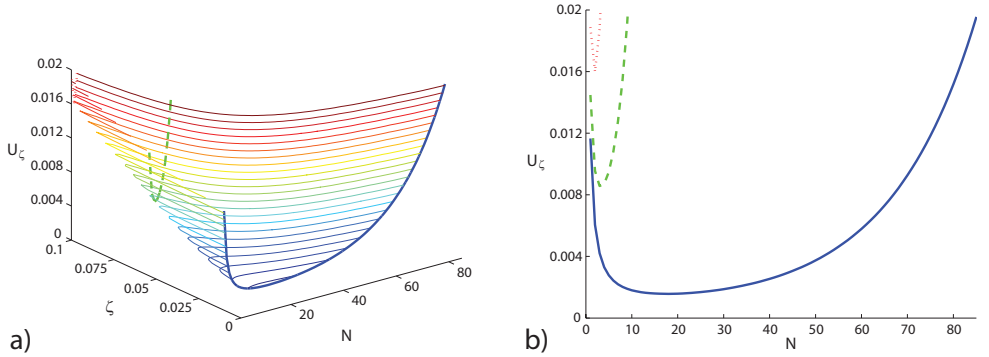

FIGURE 3.6: Magnitude of the damping uncertainty for $U_x = 0.05$ and $U_T = 0.01$. Plot (a) shows the change in the uncertainty for increasing ζ and N. Plot (b) shows the uncertainty of the damping for $\zeta = 0.01$, 0.054, and 0.1 as solid, dashed, and dotted curves, respectively.

ratio range of $0.01 \leqslant \zeta \leqslant 0.10$ with combinations of 100 values of displacement uncertainty in the range of $0.01 \leqslant U_x \leqslant 0.10$ and 100 values of period uncertainty in the range of $0.01 \leqslant U_T \leqslant 0.05$. For each value of ζ, the ideal number of periods was recorded for all 10,000 possible combinations. The minimum and maximum ideal number of periods were then recorded for each ζ. This procedure enabled the creation of the compact two-dimensional plot shown in Fig. 3.7, which highlights the range of the ideal number of periods for each damping ratio. Since the measurement

uncertainties are not required, Fig. 3.7 can be used as a guide to quickly determine the ideal number of periods in log decrement calculations.

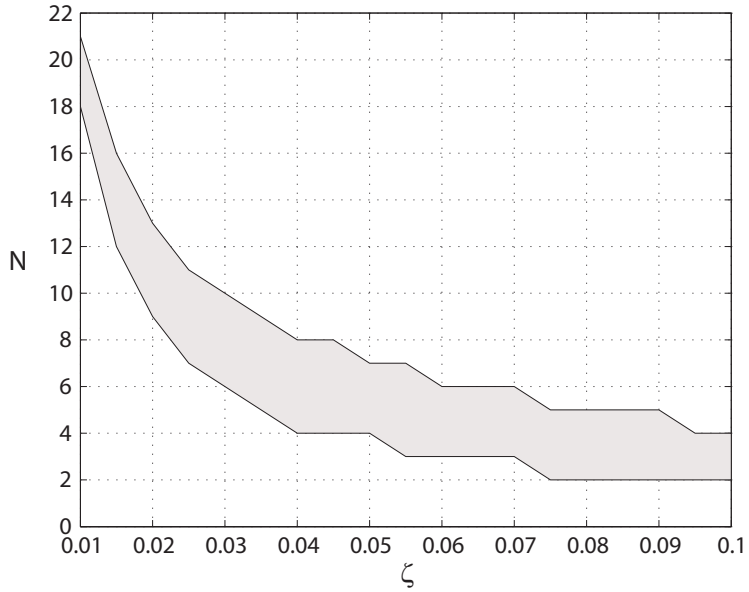

FIGURE 3.7: The ideal number of periods plotted over a range of damping ratios. The shaded portion highlights the range of periods that will reduce U_ζ for a given ζ. The plot was created using values of U_x between 0.01 and 0.10, and values of U_T between 0.01 and 0.05.

To illustrate how to use the guide on experimental data, refer to the data provided in Fig. 3.8. The damping ratio was initially estimated to be about 0.01, so the number of periods included in the calculation was $N = 18$ based on Fig. 3.7. The damping was then found to be $\zeta = 0.007 \pm 0.001$ with the damping uncertainty determined from Fig. 3.3 with $U_x = 0.003$ and $U_T < 0.01$ estimated from the data. Fig. 3.8 also further illustrates how increasing the number of periods in the log decrement calculation eventually reduces the accuracy of the estimate as the response ultimately becomes indistinguishable from the noise.

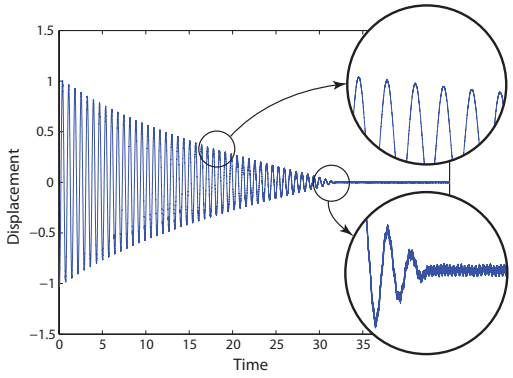

FIGURE 3.8: Scaled response of an experimental oscillator with the parameters $\zeta = 0.007 \pm 0.001$, $U_x = 0.003$, and $U_T < 0.01$ determined using the log decrement method.

3.3 Conclusions

The intent of this chapter is to deepen the understanding of the well known logarithmic decrement method. An uncertainty analysis was presented in which the uncertainty of the damping ratio was found in terms of the uncertainty of the displacement and the period. In addition, new insights are quantified for the effect of the number of periods on the damping ratio uncertainty. Specifically, increasing the number of periods from unity decreases the damping uncertainty, but there is a limit on the number of periods which can be included before the uncertainty begins to increase. Several examples were provided to further demonstrate the role of the damping on the damping ratio uncertainty. These examples revealed that the larger the damping, the fewer number of periods should be included in the calculation.

Finally, a guide to determine the number of periods to use for a particular damping ratio calculation was presented in Fig. 3.7. This figure is accurate for damping ratio ranges of $0.01 \leqslant \zeta \leqslant 0.10$, displacement uncertainty ranges of $0.01 \leqslant U_x \leqslant 0.10$, and period uncertainties ranges of $0.01 \leqslant U_x \leqslant 0.05$. The uncertainties U_x and U_T are scaled by the initial peak x_1 and the period, respectively. For noise with a Gaussian distribution, the uncertainty U_x can be determined from the standard deviation

of the noise and the initial peak. Changes in ζ, U_x, and U_T had the effect of raising the upper bound of the shaded area in Fig. 3.7 but had little affect on the lower bound of the shaded area. Therefore, this guide can be used as rule of thumb for parameters outside the specified ranges. This is reasonable because the increase of the upper bound is associated with a broadening of the minimum U_ζ for which the lower bound still tends to provide a good estimate of the ideal number of periods.

4

Delay Differential Equations

Several recent works have proposed discretization methods to ascertain the stability properties of both autonomous and non-autonomous DDEs. For example, several works have described a semi-discretization approach, which divides the timeline into short intervals on which an approximate analytical solution can be obtained (Insperger and Stépán, 2002; Insperger and Stépán, 2004; Insperger et al., 2008). The collection of the approximate analytical solutions is then used to create a finite-dimensional transition matrix, which approximates the infinite-dimensional monodromy operator of the DDE. Collocation methods have also appeared in the literature using either Chebyshev or LGL points to construct a dynamic map that approximates the DDE (Boyd, 2001). As yet another example, the Temporal Finite Element Analysis (TFEA) method has been used to study the stability of equilibria of DDEs (Mann and Patel, 2010). This method discretizes the time interval of interest into a finite number of temporal elements. The original DDE is then transformed into the form of a discrete map whose characteristic multipliers determine stability. While the original versions of this approach focused solely on h-convergence, by increasing the order of the trial function polynomials, more recent versions, referred to as spec-

tral element methods, have demonstrated both p- and hp-convergence methodologies (Khasawneh and Mann, 2011b).

Although the semi-discretization, collocation, and spectral element methods have all been used to study various DDEs, a comparison among these methods has yet to appear in the literature. In contrast to recent works on the spectral element method (Khasawneh and Mann, 2011b; Khasawneh et al., 2011b; Khasawneh and Mann, 2011a; Khasawneh et al., 2011a) which sought to develop this technique, the focus of this chapter is to compare and contrast the features of the three techniques along with their performance. In particular, the convergence rate and the computational time required to generate a converged stability diagram are compared using three numerical studies.

The content of this chapter is organized as follows. The next section describes the assumptions and equations required to implement each method, followed by the section which discusses the criteria used to compare the methods and how the criteria was implemented. Three numerical studies are then presented which include a ship stability model, the delayed damped Mathieu equation, and a helicopter rotor control problem. Finally, the conclusions of the numerical study are presented.

4.1 Description of methods

A general delay differential equation can be written in the state-space form according to

$$\dot{\mathbf{x}}(t) = \mathbf{A}(t)\mathbf{x}(t) + \mathbf{B}(t)\mathbf{x}(t-\tau), \tag{4.1}$$

where $\mathbf{x}$ is a d-dimensional vector, $\mathbf{A}(t)$ and $\mathbf{B}(t)$ are the $d \times d$ system matrices, and τ is a positive delay. Equation (4.1) can describe the dynamics of a linear delay oscillator, or it can represent the linearization of a nonlinear system about an equilibrium position. Two specific cases of DDEs are of special interest: the

autonomous DDE case (i.e. $\mathbf{A}(t) = \mathbf{A}$, $\mathbf{B}(t) = \mathbf{B}$) and the non-autonomous case where the coefficients are time periodic with the period T (i.e. $\mathbf{A}(t) = \mathbf{A}(t+T)$, $\mathbf{B}(t) = \mathbf{B}(t+T)$). The case $\tau = T$ is of special interest in science and engineering and it appears in a wide variety of applications such as machining. This chapter focuses on describing stability analysis techniques for DDEs such as Eq. (4.1) for both autonomous and time-periodic DDEs with $\tau = T$.

The stability analysis of the equilibria of DDEs can be performed using Floquet theory. This approach investigates the spectrum of the monodromy operator which maps the history segment of $[-\tau, 0]$ one period ahead onto $[-\tau+T, T]$ which becomes $[0, T]$ for the case where $\tau = T$, see Fig. 4.1a. However, the monodromy operator acts on an infinite dimensional state space: the space of continuous functions. Therefore, in general, it is not possible to deal directly with the eigenvalues of the monodromy operator. Instead, the eigenvalues of the monodromy operator are approximated with the eigenvalues of a finite dimensional matrix called the monodromy matrix. The monodromy matrix $\mathbf{U}$ represents the linear map

$$\mathbf{x}_{k+1} = \mathbf{U}\mathbf{x}_k \tag{4.2}$$

between the discretized state-space over the segment $[-T, 0]$ denoted by the vector $\mathbf{x}_k$ and those over the segment $[0, T]$, represented by the vector $\mathbf{x}_{k+1}$, see Fig. 4.1b. As the discretization is refined, the size of $\mathbf{U}$ is increased while more eigenvalues are well approximated. The eigenvalues of the monodromy matrix form an approximation to the Floquet multipliers of the monodromy operator. These eigenvalues determine the local asymptotic stability of Eq. (4.1) and the loss of stability according to the criteria shown in Fig. 4.2. The period can be discretized into a uniform mesh as shown in Fig. 4.3a, or a non-uniform mesh such as the pseudo spectral meshes shown in Fig. 4.3b and Fig. 4.3c. Uniform meshes typically have a low order polynomial of fixed degree, and increasing the accuracy of the approximation is accomplished

by increasing the number of intervals. Increasing the number of uniform intervals, sometimes referred to as "h-convergence," reduces the error on the order of $O\left[\frac{1}{n}\right]$ for a linear convergence where n is the number of intervals (Boyd, 2001). A pseudo spectral mesh however, increases the accuracy of the approximation by increasing the order of polynomial rather than the number of intervals. Increasing the order of polynomial, sometimes referred to as "p-convergence," reduces the error on the order of $O\left[\left(\frac{1}{n}\right)^n\right]$ for an "exponential" convergence where n is the order of the polynomial (Boyd, 2001). In addition, pseudo spectral meshes can be split into several elements for spectral element methods that have "hp-convergence."

Each method described in this section provides a scheme to obtain a finite dimensional approximation for the infinite dimensional monodromy operator. Specifically, the semi-discretization approach, the spectral element method, and the collocation approach are described. All the methods are based on discretizing the state-space of Eq. (4.1) to obtain a monodromy matrix $\mathbf{U}$. The eigenvalues obtained from $\mathbf{U}$ are then used to ascertain the stability of Eq. (4.1) based on the criteria in Fig. 4.2.

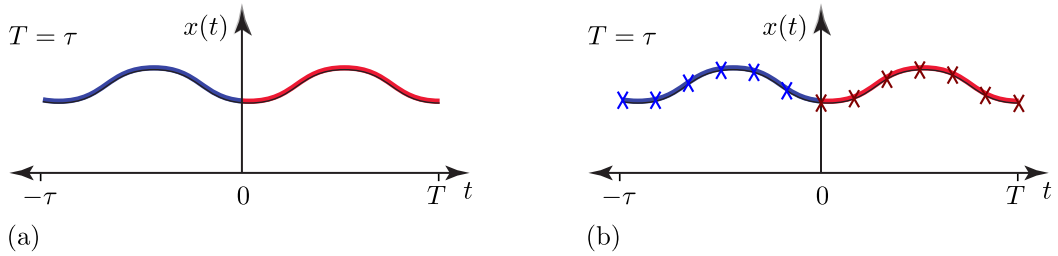

FIGURE 4.1: Mapping of the history segment on $[-\tau, 0]$ one period ahead onto $[-\tau + T, T]$. Figure (a) shows the continuous state-space whereas Fig. (b) shows a discretization of the state-space.

4.1.1 Semi-discretization

The semi-discretization approach approximates the DDE using a system of linear, first order, ordinary differential equations (ODEs). This method is capable of solving a wide class of DDEs, including autonomous and non-autonomous equations

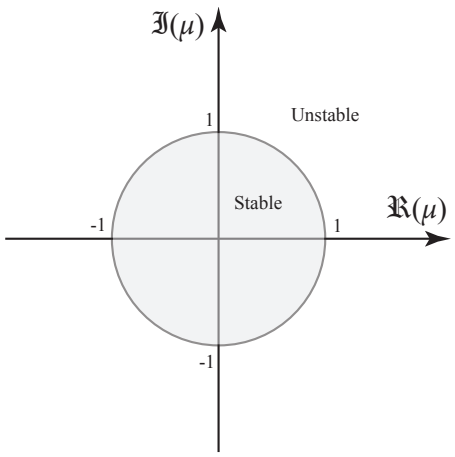

FIGURE 4.2: The stability criteria for the dynamic map in Eq. (4.2). The system is asymptotically stable if all the eigenvalues of U lie within the unit circle in the complex plane, unit circle shown shaded.

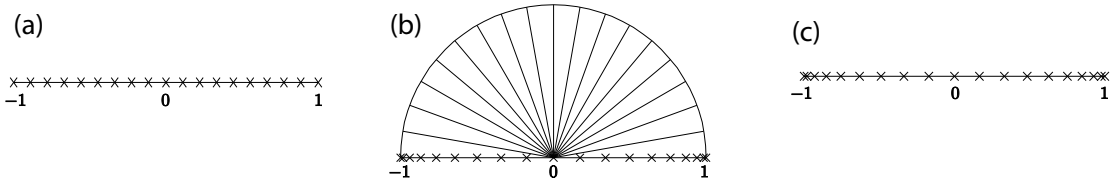

FIGURE 4.3: Some of the common choices for discretization mesh t_i. Figure (a) shows an equi-spaced grid where $t_i = -1 + ih$ and $h = \frac{2}{n}$. Figure (b) shows a Chebyshev grid of the first kind where $t_i = \cos(\frac{\pi i}{n})$. Figure (c) shows a Legendre-Gauss-Lobatto (LGL) grid where t_i equals the i^{th} root of $(1-t^2)L_n'(t) = 0$, and $L_n(t)$ is the n^{th} order Legendre polynomial.

(Insperger and Stépán, 2002). To illustrate the basic steps of semi-discretization, consider the general non-autonomous DDE in Eq. (4.1) where the current states and the delayed states are given by the vectors $\mathbf{x}(t)$ and $\mathbf{x}(t-\tau)$, respectively.

The first step in semi-discretization is to discretize the period T into equal intervals of Δt according to

$$\Delta t = \frac{T}{k}\,, \tag{4.3}$$

where k is the number of intervals used. The choice of T is obvious for non-autonomous systems; however, for autonomous systems, the period may be arbitrarily chosen as the duration of the delay $T = \tau$. Another choice for autonomous

systems is to use a period of $T = \Delta t = \tau/k$.

Next, a closer look is taken at how time is discretized as demonstrated in Fig. 4.4. Three intervals are highlighted: (1) the current interval between nodes t_i and t_{i+1}, (2) the interval one period prior to the current interval between nodes t_{i-k} and t_{i-k+1}, and (3) the interval nearest to the delay τ between nodes t_{i-r} and t_{i-r+1}. The most general case is shown where the delay is not equal to the period, and the delay can also be shorter than the period.

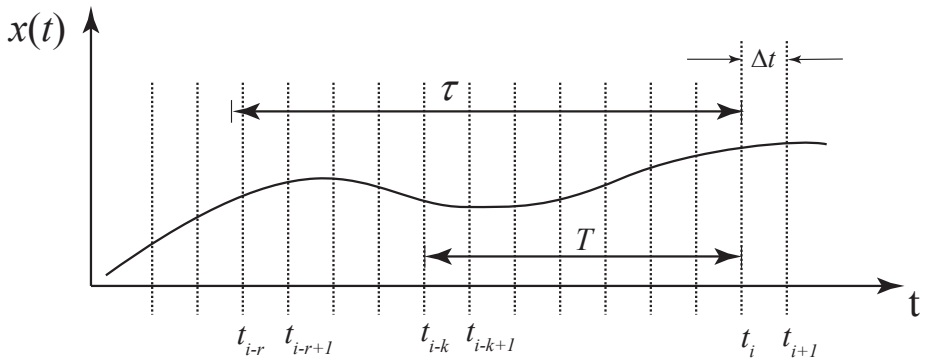

FIGURE 4.4: Semi-discretization intervals for the state x. Note that the intervals are all of equal duration.

The delay interval t_{i-r} to t_{i-r+1} is the interval whose beginning is closest to the delay, and the delay interval may or may not contain the beginning of the delay. The delay interval is found by defining r, the beginning of the delay interval, by

$$r = \text{round}\left(\frac{\tau}{\Delta t} + \frac{p}{2} - \frac{1}{2}\right), \tag{4.4}$$

where p is the order of the semi-discretization. The first order semi-discretization method will be considered in this chapter as second and higher orders do not significantly improve convergence properties if the time periodic terms are approximated by piecewise constants (Insperger et al., 2008). It should be noted that while the first order semi-discretization employs a larger order polynomial than the zeroth order version, the polynomial order remains constant while the number of intervals is

increased in order to improve the approximation. Therefore, the semi-discretization method exhibits h-convergence even for the higher order implementations.

If the intervals defined above are small enough, the time-periodic matrix $\mathbf{A}(t)$ can be approximated by the average value over the interval. For example, during the i^{th} interval, $\mathbf{A}(t)$ can be approximated by

$$\mathbf{A}_i = \frac{1}{\Delta t} \int_{t_i}^{t_{i+1}} \mathbf{A}(t)\, \mathrm{d}t\,, \tag{4.5}$$

where $\mathbf{A}_i$ is the time average over the interval i for $\mathbf{A}(t)$. Averaging the time dependent coefficient removes the time dependency of $\mathbf{A}$ over the small intervals of duration Δt. Additional linearization is performed by estimating the states $\mathbf{x}$ by a polynomial over the delay interval (Insperger et al., 2008). This second assumption increases the fidelity of the approximation, and an analytical solution is still available. After applying these small interval assumptions, the DDE is approximated over each interval by a series of linear ODEs of the form

$$\dot{\mathbf{x}}(t) = \mathbf{A}_i \mathbf{x}(t) + \mathbf{B}(t)\mathbf{u}(t)\,, \tag{4.6}$$

where $\mathbf{u}(t)$ is a polynomial that estimates the value of the states $\mathbf{x}$ over the interval at the delay. For first order semi-discretization, the polynomial is

$$\mathbf{u}(s) = \left(\frac{s}{\Delta t} - \frac{\tau - r\Delta t}{\Delta t}\right) \mathbf{x}\left((i-r+1)\Delta t\right) + \left(\frac{\Delta t - s}{\Delta t} - \frac{\tau - r\Delta t}{\Delta t}\right) \mathbf{x}\left((i-r)\Delta t\right)\,, \tag{4.7}$$

where s is the local time within the delay interval and varies from 0 to Δt. The variable s can be replaced by $t - i\Delta t$ in order to make $\mathbf{u}(s)$ a function of t. This function can be viewed as the sum of two lines as shown in Fig. 4.5. In this interpretation, the lines have either a positive or negative slope of $\frac{1}{\Delta t}$, and the offsets are weighting

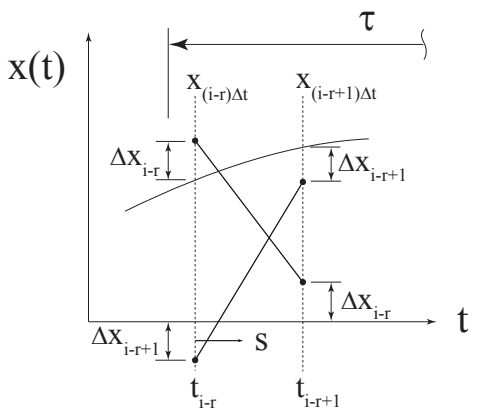

FIGURE 4.5: Linear estimation of the state x in the delay interval for first order semi-discretization. The weighting factor $\Delta x_{i-r} = -\frac{\tau - r\Delta t}{\Delta t} x_{(i-r)\Delta t}$ and $\Delta x_{i-r+1} = -\frac{\tau - r\Delta t}{\Delta t} x_{(i-r+1)\Delta t}$. The local time s is zero at t_{i-r} and equal to Δt at t_{i-r+1}.

factors. In Fig. 4.5 the weighting factor $\Delta x_{i-r} = -\frac{\tau - r\Delta t}{\Delta t} x\left((i-r)\Delta t\right)$ in the first term of Eq. 4.7, and $\Delta x_{i-r+1} = -\frac{\tau - r\Delta t}{\Delta t} x\left((i-r+1)\Delta t\right)$ in the second term.

The solution of Eq. (4.6) for any interval can be found (Brogan, 1991) as

$$\mathbf{x}(t) = \mathrm{e}^{\mathbf{A}_i(t-t_i)}\mathbf{x}_i + \int_{t_i}^{t} \mathrm{e}^{\mathbf{A}_i(t-s)}\mathbf{B}(s)\mathbf{u}(s)\,\mathrm{d}s\,, \tag{4.8}$$

where s is the local time within the interval, t_i is the time at the beginning of the interval, $\mathbf{x}_i$ is the value of the states at t_i, and $\mathbf{u}(s)$ is the approximated state from Eq. (4.7). The solution is valid inside of the entire interval, but only the values of the state at the end of the interval are needed to map states from the beginning of the interval to its end. If the matrix $\mathbf{B}$ is constant, then Eq. (4.8) can be integrated analytically for the values of $\mathbf{x}$ at the end of the interval. The resulting solution is

given by

$$\mathbf{x}_{i+1} = \mathrm{e}^{\mathbf{A}_i \Delta t}\mathbf{x}_i + \mathbf{R}_{i,1}\mathbf{x}_{i-r+1} + \mathbf{R}_{i,0}\mathbf{x}_{i-r}, \tag{4.9a}$$

$$\mathbf{R}_{i,1} = \mathbf{B}\left(-\mathbf{A}_i^{-1} + \frac{1}{\Delta t}\left(-\mathbf{A}_i^{-2} + (\tau - r\Delta t)\mathbf{A}_i^{-1}\right)\right)\left(\mathbf{I} - \mathrm{e}^{\mathbf{A}_i \Delta t}\right), \tag{4.9b}$$

$$\mathbf{R}_{i,0} = \mathbf{B}\left(\mathbf{A}_i^{-1} + \frac{1}{\Delta t}\left(\mathbf{A}_i^{-2} - (\tau - (r-1)\Delta t)\mathbf{A}_i^{-1}\right)\right)\left(\mathbf{I} - \mathrm{e}^{\mathbf{A}_i \Delta t}\right), \tag{4.9c}$$

where $\mathbf{I}$ is the identity matrix, and Δt has replaced $t_{i+1} - t_i$ (Insperger et al., 2008). The solution is only valid if the inverse of $\mathbf{A}$ exists. For the zeroth order semi-discretization, the state $\mathbf{x}$ during the delay interval is a constant, estimated by the value of the state at the delay x_{i-r}. The resulting value for $\mathbf{R}_{i,1}$ is zero and $\mathbf{R}_{i,0} = \mathbf{B}\left(\mathrm{e}^{\mathbf{A}_i \Delta t} - \mathbf{I}\right)\mathbf{A}_i^{-1}$ for the zeroth order case and a constant $\mathbf{B}$ (Insperger et al., 2008).

The next step is to systematically construct a discrete map for each interval, mapping the values at the beginning of each interval to its end. This relationship is defined by

$$\mathbf{x}_{i+1} = \mathbf{M}_i \mathbf{x}_i, \tag{4.10}$$

where $\mathbf{x}_{i+1}$ is a column vector of the states at the end of each interval and $\mathbf{x}_i$ is a column vector of the states at the beginning of each interval. The matrix $\mathbf{M}_i$ maps the states at the beginning of the interval to the states at the end of the interval and can be written out as

$$\mathbf{M}_i = \begin{bmatrix} \mathrm{e}^{\mathbf{A}_i \Delta t} & \mathbf{0} & \cdots & \mathbf{R}_{i,1} & \mathbf{R}_{i,0} \\ \mathbf{I} & \mathbf{0} & \cdots & \mathbf{0} & \mathbf{0} \\ \mathbf{0} & \mathbf{I} & \cdots & \mathbf{0} & \mathbf{0} \\ \vdots & \vdots & \ddots & \vdots & \vdots \\ \mathbf{0} & \mathbf{0} & \cdots & \mathbf{I} & \mathbf{0} \end{bmatrix}. \tag{4.11}$$

As can be seen in Eq. (4.11), the top row enforces the relationship between $\mathbf{x}_{i+1}$ and $\mathbf{x}_i$ defined in Eq. (4.9)a. The remainder of the matrix equates like terms from

vectors $\mathbf{x}_{i+1}$ and $\mathbf{x}_i$. The size of the matrix $\mathbf{M}_i$ is determined by the variable r and the degree of freedom of the system of delay equations.

Finally, using the relationship $\mathbf{M}_i$ between the beginning and the end of each interval, the relationship between the beginning and end of the period may be calculated. This is accomplished by multiplying the mapping matrix $\mathbf{M}_i$ of each interval from the beginning of the period to its end (Insperger and Stépán, 2004) as shown by

$$\mathbf{x}_{k+1} = \mathbf{M}_{r-1}\mathbf{M}_{r-2}...\mathbf{M}_0\mathbf{x}_k = \mathbf{U}\mathbf{x}_k. \tag{4.12}$$

The resulting product is the monodromy matrix $\mathbf{U}$. The eigenvalues of the monodromy matrix $\mathbf{U}$, also known as the characteristic multipliers, indicate the stability of the system.

4.1.2 Spectral element

The spectral element method approximates the solution to DDEs based on the method of weighted residuals. In the spectral element method, the time-line is discretized with nodes as shown in Fig. 4.6. In the most general case, the spectral element method may include multiple elements in each period for hp-convergence. However, for simplicity, the following explanation will assume one element per period for p-convergence. Note that increasing the number of nodes leads to significantly quicker convergence than increasing the number of elements, so for most cases there is no loss of performance due to this simplification.

The Legendre-Gauss-Lobatto (LGL) points will be used for the spectral element implementation in this chapter, but Chebyshev points could be used instead. The LGL points create a non-uniform mesh which allows a large number of nodes to be used in each period. If equi-distributed points were used instead, increasing the number of nodes would lead to ill-conditioned systems, especially for meshes of eight or more nodes (Berrut and Trefethen, 2004). The LGL nodes are computed from the

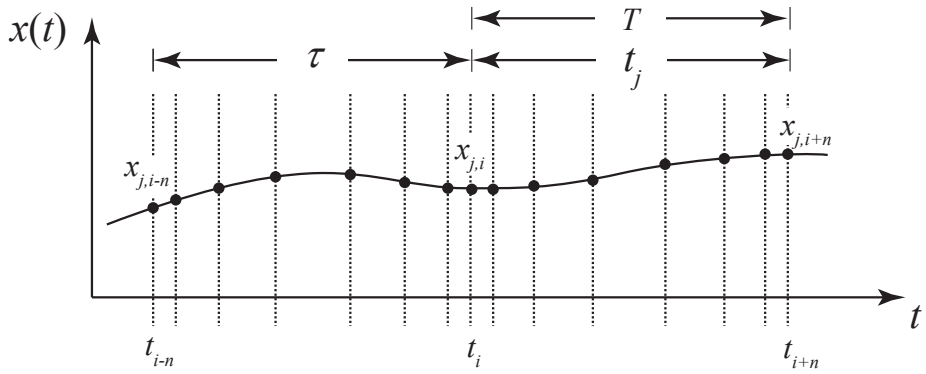

FIGURE 4.6: Spectral element mesh for the state x. Note that the mesh is non-uniform.

roots of the polynomial $(1-u^2)L'_n(u)$ where $L_n(u)$ is the n^{th} order Legendre function, $L'_n(u)$ is the first derivative of $L_n(u)$ with respect to u, and u ranges between -1 and 1. The LGL nodes must be shifted to the arbitrary interval $[a, b]$ of the period through the relation

$$\tilde{u} = \frac{b-a}{2}u + \frac{b+a}{2}, \tag{4.13}$$

where $u \in [-1, 1]$ and $\tilde{u} \in [a, b]$.

The solution is approximated at each grid point using polynomial trial functions for each period according to

$$\mathbf{x}_j(t) = \sum_{i=1}^{n+1} \mathbf{x}_{j,i}\, \phi_i(\eta), \tag{4.14a}$$

$$\mathbf{x}_j(t-\tau) = \sum_{i=1}^{n+1} \mathbf{x}_{j,i-n}\, \phi_i(\eta)\,, \tag{4.14b}$$

where $\mathbf{x}_{j,i}(t)$ is the vector of discretized states of the element j, $\phi_i(\eta)$ is the trial function, and η is the normalized local time for each element. The normalized local time η is defined as $\eta = \sigma/t_j$ where σ is the local coordinate of the element j, and t_j is the duration of the element.

The trial functions ϕ_i can be found using the barycentric Lagrange formula

$$\phi_i(t) = \frac{\frac{\rho_i}{t-t_i}}{\sum_{j=1}^{n+1} \frac{\rho_j}{t-t_j}}\,, \tag{4.15}$$

and the barycentric weights are given by

$$\rho_i = \frac{1}{\prod_{k=1,k\neq i}^{n+1} (t_i - t_k)},\ k = 1, 2, \ldots, n+1\,. \tag{4.16}$$

Computing $\phi_i(t)$ only requires the mesh information. In this chapter, a barycentric form of the Lagrange representation is used. The effect of rounding errors, which is directly related to the stability of the formula, has been discussed in Higham (2004). To summarize the results of Higham, the barycentric formula is numerically stable if a good set of interpolation points is chosen. Specifically, error bounds grow slowly as the number of interpolation points (order of the interpolating polynomial) is increased. Since the Legendre-Gauss-Lobatto points were used, which constitute a set with good interpolation properties, the error grows slowly with the degree of the polynomial. All calculations in this chapter used the standard unit roundoff of floating point arithmetic in Matlab which is approximately equal to 10^{-16}.

The trial functions obtained from Eq. (4.15) have two useful properties. First, they are independent of the data or the function being approximated. This means that once the trial functions are obtained for a certain mesh, they can be reused to approximate any continuous function on the same mesh. Second, at the i^{th} mesh point, the i^{th} trial function is equal to unity, whereas all the other trial functions are equal to zero. This is expressed by the equation

$$\phi_i(t_k) = \delta_{i,k},\ t_k \in \{t_i\}_{i=1}^{n+1}\,, \tag{4.17}$$

where δ is the Kronecker delta. The barycentric formula can also be used to obtain the derivative of the trial functions at the interpolation nodes according to

$$\phi_i'(t_k) = \begin{cases} \frac{\rho_i/\rho_k}{t_i - t_k}, & i \neq k \\ \sum_{i=0, i\neq k}^{n+1} \frac{-\rho_i/\rho_k}{t_i - t_k}, & i = k. \end{cases} \tag{4.18}$$

Equation (4.18) is useful for approximating the derivatives of the states at the mesh point. For example, assume that the vector of states is given by $\mathbf{z}$. Then, if the barycentric Lagrange formula is used to approximate $\mathbf{z}$ on a mesh $\{t_i\}$, then the derivative $\mathbf{z}'$ on $\{t_i\}$ is given by

$$\mathbf{z}' = \mathbf{D}\mathbf{z}, \tag{4.19}$$

where $D_{ki} = \phi_i'(t_k)$.

The approximation of the continuous states $\mathbf{x}(t)$ is made up of the coefficients $\mathbf{x}_{j,i}$ (the values of $\mathbf{x}(t)$ at the nodes) and the trial functions $\phi_i(\eta)$. The indices i and j refer to the node and element, respectively. Substituting the approximate solution into Eq. (4.1) gives

$$\sum_{i=1}^{n+1} \left(\frac{1}{t_j} \mathbf{x}_{j,i}\, \phi_i'(\eta) - \mathbf{A}(t_\eta)\mathbf{x}_{j,i}\, \phi_i(\eta) - \mathbf{B}(t_\eta)\mathbf{x}_{j,i-n}\, \phi_i(\eta) \right) = \text{error}\,, \tag{4.20}$$

where $t_\eta = (\eta + j - 1)t_j$, the prime indicates a derivative with respect to η, and the error term is associated with the approximation procedure.

The approximation error in Eq. (4.20) can be minimized by multiplying the approximate solution by a set of independent test functions and setting the integral over the duration of the element equal to zero. This is called the method of weighted residuals which also generates enough equations to create the dynamic map (Reddy, 1993). The spectral element method uses Legendre polynomials for the test functions. Further, to keep the resulting matrices square, the number of the test functions

is always one less than the number of the trial functions. Assuming that the index of the test functions $\psi(\eta)$ is p, the weighted expression of Eq. (4.20) becomes

$$\int_0^1 \left(\frac{1}{t_j} \mathbf{x}_{j,i}\, \phi_i'(\eta) - \mathbf{A}(t_\eta)\mathbf{x}_{j,i}\, \phi_i(\eta) - \mathbf{B}(t_\eta)\mathbf{x}_{j,i-n}\, \phi_i(\eta) \right) \psi_p(\eta)\, \mathrm{d}\eta = 0. \tag{4.21}$$

Applying each test function in turn, the resulting equations for each element can be combined into a global matrix equation. The resulting expression for the global matrix with one element for each period and $n+1$ nodes is

$$\begin{bmatrix} \mathbf{I} & \mathbf{0} & \dots & \mathbf{0} & \mathbf{0} \\ \mathbf{N}^1_{j,i} & \mathbf{N}^1_{j,i+1} & \dots & \mathbf{N}^1_{j,i+n-1} & \mathbf{N}^1_{j,i+n} \\ \mathbf{N}^2_{j,i} & \mathbf{N}^2_{j,i+1} & \dots & \mathbf{N}^2_{j,i+n-1} & \mathbf{N}^2_{j,i+n} \\ \vdots & \vdots & \ddots & \vdots & \vdots \\ \mathbf{N}^n_{j,i} & \mathbf{N}^n_{j,i+1} & \dots & \mathbf{N}^n_{j,i+n-1} & \mathbf{N}^n_{j,i+n} \end{bmatrix} \begin{bmatrix} \mathbf{x}_{j,i} \\ \mathbf{x}_{j,i+1} \\ \vdots \\ \mathbf{x}_{j,i+n-1} \\ \mathbf{x}_{j,i+n} \end{bmatrix} = \begin{bmatrix} \mathbf{0} & \mathbf{0} & \dots & \mathbf{0} & \mathbf{I} \\ \mathbf{P}^1_{j,i-n} & \mathbf{P}^1_{j,i-n+1} & \dots & \mathbf{P}^1_{j,i-1} & \mathbf{P}^1_{j,i} \\ \mathbf{P}^2_{j,i-n} & \mathbf{P}^2_{j,i-n+1} & \dots & \mathbf{P}^2_{j,i-1} & \mathbf{P}^2_{j,i} \\ \vdots & \vdots & \ddots & \vdots & \vdots \\ \mathbf{P}^n_{j,i-n} & \mathbf{P}^n_{j,i-n+1} & \dots & \mathbf{P}^n_{j,i-1} & \mathbf{P}^n_{j,i} \end{bmatrix} \begin{bmatrix} \mathbf{x}_{j,i-n} \\ \mathbf{x}_{j,i-n+1} \\ \vdots \\ \mathbf{x}_{j,i-1} \\ \mathbf{x}_{j,i} \end{bmatrix}, \tag{4.22}$$

where $\mathbf{I}$ is the $d \times d$ identity matrix. The expressions for the matrices $\mathbf{N}$ and $\mathbf{P}$ populating the global matrices are

$$\mathbf{N}^p_{ji} = \int_0^1 \Big(\frac{1}{t_j} \mathbf{I} \phi_i'(\eta) - \mathbf{A}(t_\eta)\phi_i(\eta) \Big) \psi_p(\eta)\, \mathrm{d}\eta \tag{4.23a}$$

$$\mathbf{P}^p_{ji} = \int_0^1 \mathbf{B}(t_\eta)\phi_i(\eta)\psi_p(\eta)\, \mathrm{d}\eta\,, \tag{4.23b}$$

where both matrices are of dimension $d \times d$.

The integrals in Eq. (4.23) are integrated using a LGL quadrature which estimates an integral by replacing it with a weighted summation of the function values at the LGL points. Denoting the integrand resulting from the weighted residual method by

$f(\eta)$, the corresponding expression for the LGL quadrature is

$$\int_0^1 f(\eta)\,\mathrm{d}\eta \approx \sum_{k=1}^{n+1} w_k f(\eta_k), \tag{4.24}$$

where η_k are the Legendre points shifted from the interval $[-1,1]$ to $[0,1]$ using Eq. (4.13), $f(\eta_k)$ are the values of $f(\eta)$ evaluated at the LGL points (Parter, 1999), and w_k are the LGL quadrature weights given by the equation

$$w_k = \begin{cases} \frac{2}{n(n+1)} & k = 1, n+1 \\ \frac{2}{n(n+1)(L_n(\eta_k))^2}, & \text{otherwise}\,. \end{cases} \tag{4.25}$$

Equations (4.24) and (4.25) are used to evaluate the integrals in Eq. (4.23) which are then used to populate the corresponding global matrices. Applying the LGL quadrature rule to these integrals and using the properties of the trial functions yields

$$\mathbf{N}^p_{ji} = \sum_{k=1}^{n+1} \left(\frac{1}{t_j}\mathbf{I}\phi_i'(\eta_k)\psi_p(\eta_k)w_k\right) - \mathbf{A}(t_\eta)\psi_p(\eta_i)w_i \tag{4.26a}$$

$$\mathbf{P}^p_{ji} = \mathbf{B}(t_\eta)\psi_p(\eta_i)w_i. \tag{4.26b}$$

Equation (4.22) can be used to define a dynamic map that has the same form as Eq. (4.2). This map is given by

$$\mathbf{H}\mathbf{x}_k = \mathbf{G}\mathbf{x}_{k-1}, \tag{4.27}$$

where the subscripts k and $k-1$ refer to the current and the previous periods, respectively. The monodromy matrix can be calculated by $\mathbf{U} = \mathbf{H}^{-1}\mathbf{G}$, and the stability of this system can be determined by the eigenvalues of $\mathbf{U}$.

4.1.3 Legendre collocation method

The Legendre collocation method is a weighted residual method similar to the spectral element method (Boyd, 2001). In the Legendre collocation method, the time-line is discretized with nodes as shown in Fig. 4.7. While the spectral element method minimizes the error element-wise, the Legendre collocation method minimizes the error point-wise. The Legendre collocation method uses the same LGL mesh, trial functions ϕ_i of Eq. (4.15), and trial function derivatives ϕ_i' of Eq. (4.18) as the spectral element method. To demonstrate the difference between the Legendre collocation method and the spectral element method, consider again Eq. (4.21). The key difference between the two methods is the choice of the test functions $\psi_p(\eta)$. The test functions in the Legendre collocation method are the Dirac delta functions at the mesh nodes. These functions are described by

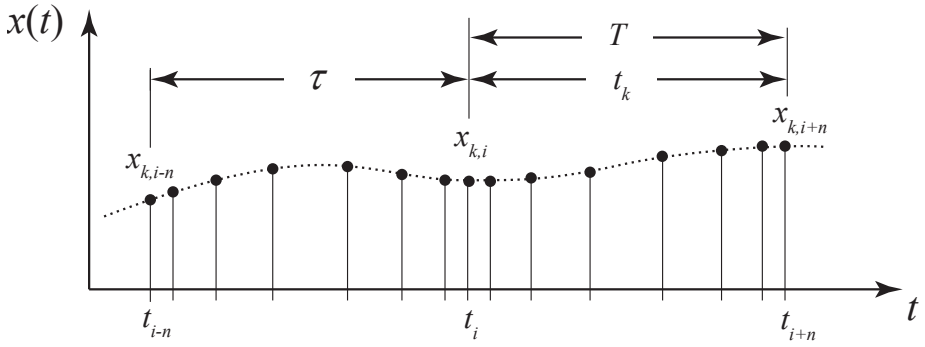

FIGURE 4.7: Legendre collocation element mesh for the state x. Note that the mesh is non-uniform.

$$\{\psi_p(\eta)\}_{p=1}^{N} = \{\delta(\eta - \eta_p)\}_{p=1}^{N}, \tag{4.28}$$

where $\{\eta_p\}$ is the set of collocation points and $\delta(\eta - \eta_p)$ is the Dirac delta function. In this chapter LGL points for the collocation points are used, but it is possible to use Chebyshev points instead. Therefore, by examining Eq. (4.21) for this choice of

ψ_p, it becomes clear that the collocation approach requires the DDE to be satisfied at the set of mesh nodes. Specifically, using the collocation approach on Eq. (4.1) gives

$$\hat{\mathbf{D}}\mathbf{x}_k = \hat{\mathbf{M}}_A\mathbf{x}_k + \hat{\mathbf{M}}_B\mathbf{x}_{k-1}, \tag{4.29}$$

where $\mathbf{x}_k$ contains the values of the states in the present period, and $\mathbf{x}_{k-1}$ contains the values of the states in the previous period. $\hat{\mathbf{M}}_A$ is a $q(N+1)$ matrix with entries

$$\hat{\mathbf{M}}_A = \begin{bmatrix} \mathbf{A}(t_0) & \mathbf{0}_q & \dots & & \mathbf{0}_q \\ \mathbf{0}_q & \mathbf{A}(t_1) & & & \vdots \\ \vdots & & \ddots & & \\ & & & \mathbf{A}(t_{N-1}) & \mathbf{0}_q \\ \mathbf{0}_q & \dots & & \mathbf{0}_q & \mathbf{0}_q \end{bmatrix} \tag{4.30}$$

where $\mathbf{A}(t_i)$ is the value of $\mathbf{A}(t)$ evaluated at the i^{th} collocation point. Similarly, $\hat{\mathbf{M}}_B$ has the entries

$$\hat{\mathbf{M}}_B = \begin{bmatrix} \mathbf{B}(t_0) & \mathbf{0}_q & \dots & & \mathbf{0}_q \\ \mathbf{0}_q & \mathbf{B}(t_1) & & & \vdots \\ \vdots & & \ddots & & \\ & & & \mathbf{B}(t_{N-1}) & \mathbf{0}_q \\ \mathbf{0}_q & \dots & & \mathbf{0}_q & \mathbf{I}_q \end{bmatrix}. \tag{4.31}$$

The matrix $\hat{\mathbf{D}}$ is calculated from the matrix $\mathbf{D}$ in Eq. (4.19). $\mathbf{D}$ is first shifted to the interval $[a, b]$ with the scaling factor $2/(b-a)$. The spectral differentiation matrix, which is defined as the Kronecker product $\mathbb{D} = \mathbf{D} \otimes \mathbf{I}_q$, is then calculated using the shifted $\mathbf{D}$. $\hat{\mathbf{D}}$ is a modified version of the spectral differentiation matrix $\mathbb{D}$, that is multiplied by $2/\tau$ to shift to the interval $[0, \tau]$, and the last q rows are changed to $[\mathbf{I}_q\mathbf{0}_q \dots \mathbf{0}_q]$. The change in the last q rows serves to enforce the continuity condition that the states are equal at the end of one period and the beginning of the next.

Equation (4.29) can be rewritten in the form $\mathbf{x}_k = \mathbf{U}\mathbf{x}_{k-1}$, where $\mathbf{U}$ is the monodromy matrix given by $\mathbf{U} = (\hat{\mathbf{D}} - \hat{\mathbf{M}}_A)^{-1}\hat{\mathbf{M}}_B$. Equation (4.28) reveals that the

collocation method is a special case of the weighted residual approach. Since spectral element and collocation methods adopt different strategies to reduce the error, the test functions used in Eq. (4.21) define the resulting analysis technique.

4.2 Criteria for Comparison

In this chapter, the performance of each method is compared by generating stability diagrams of DDE systems. Generating such a diagram, especially at the border of stable and unstable regions, requires a good approximation of the maximum eigenvalue of the monodromy operator in a reasonable amount of computational time. Therefore, the criteria of comparison used in this chapter is the convergence of the maximum eigenvalues and the computational time required to generate a converged stability diagram for each method.

To reach convergence, the calculated eigenvalues must approach the largest eigenvalues of the monodromy operator as the finite divisions of the period are reduced. The smallest monodromy matrix required to accurately estimate the monodromy operator is directly proportional to the computational dimension of each method which is the number of collocation points in the Legendre collocation method, the number of intervals in the semi-discretization method, and the number of mesh points in the spectral element method. Only one element is used for both the Legendre collocation and spectral element methods. In the following numerical studies, the computational dimension was increased from three to $N_{\max} = 50$ for each method. For each computational dimension, the approximate maximum eigenvalue for one point on the stability diagram is calculated. The error measure used for the convergence is the absolute error

$$\epsilon_{\text{stability}} = |\lambda - \mu_*| \ , \tag{4.32}$$

where $\lambda = \max |\mu|$ is the approximation of the maximum eigenvalue, whereas μ_* is

the reference maximum eigenvalue obtained with the Legendre collocation approach ($\mu_* = \max(|\mu(N_{\max})|)$). The absolute error is plotted as a function of the computational dimension, and the rate at which each method approaches convergence is compared. In the following studies, convergence is defined as the computational dimension at which the absolute error calculated by Eq. (4.32) is zero within the standard unit roundoff of floating point arithmetic in Matlab which is approximately equal to 10^{-16}.

To compare the computational time of each method, the average time required to calculate the converged stability diagram five times was recorded for each numerical study. For each method, the smallest computational dimension required to achieve convergence was used, which is equivalent to the smallest monodromy matrix required. All three methods were programmed as their "full" algorithm and in the same basic code structure. No computational tricks or optimization techniques were used in order to provide the best comparison. The implementation of zeroth order semi-discretization used for the comparisons was compared with the zeroth order code provided by Insperger and Stépán (2004) (small changes were made to Insperger's code such as using matrix division instead of "inv" and initializing vectors). The code provided by Insperger includes matrix truncation, but the average computation time of 271.1 seconds was found to be nearly identical to the average of 273.6 seconds required by the code used in the study for identical parameters. Since all three methods can be improved by various techniques, the comparisons provided in this chapter are believed to be fair and accurate. In addition, the computational times reported are intended for a comparison of the efficiency of each method and not as an absolute measure. It is expected that advances in computer technology will increase the computational speeds of each method, but will not significantly change the relative speed between methods. Each method was programmed in Matlab R2010b and run on a Windows 7 PC with an Intel(R) Core(TM) i5 CPU @2.26GHz with

4GB of installed memory.

4.3 Numerical Studies

In this section, numerical studies for a ship stability model, the delayed damped Mathieu equation, and a helicopter rotor control stability problem are presented. For all three studies, a brief description of the physical representation, the key parameters, and the $\mathbf{A}(t)$ and $\mathbf{B}(t)$ state space matrices for Eq. (4.1) are given. Then, the results of the numerical comparisons for the three methods are presented. These results include stability diagrams of the systems, convergence plots, and tables comparing the computational performance.

4.3.1 Ship stability

Ships can be stabilized by the "activated tanks method" where a ballast is displaced between tanks by means of an axial propeller pump. The pump is controlled by instruments responsive to the ship's angular motion. The phase of the moving ballast is displaced so that the ballast concentration is at a maximum in a tank which rises in space (due to rolling) when the angular velocity is also at its maximum. When the pump begins to work beyond its capacity, the resulting cavitation results in a delayed damping term and the following delay differential equation

$$\ddot{x}(t) + k\dot{x}(t) + K\dot{x}(t-\tau) + \omega_0^2 x(t) = a\sin\omega t\,, \tag{4.33}$$

where x is the roll motion, and K is the damping associated with the stabilizing equipment (Minorsky, 1942, 1962). A variational equation can be obtained from Eq. (4.33) by substituting $x = x_p + \xi(t)$ and subtracting the periodic motion x_p. Nondimensionalizing this equation results in

$$\xi''(\eta) + \alpha\xi'(\eta) + \beta\xi'(\eta - \hat{\tau}) + \xi(\eta) = 0\,, \tag{4.34}$$

where η is dimensionless time ($\eta = \omega_0 t$), $\hat{\tau}$ is a dimensionless delay, a prime represents a derivative with respect to η, $\alpha = k/\omega_0$, and $\beta = K/\omega_0$ (Minorsky, 1962). The state space matrices $\mathbf{A}$ and $\mathbf{B}$ are given by

$$\mathbf{A} = \begin{bmatrix} 0 & 1 \\ -1 & -\alpha \end{bmatrix}, \quad \mathbf{B} = \begin{bmatrix} 0 & 0 \\ 0 & -\beta \end{bmatrix}. \tag{4.35}$$

The stability diagram for this system is shown in Fig. 4.8a with a 100x100 grid in α, β parameter space. The stability diagram was generated using each method with nearly identical results. The semi-discretization method generated a diagram that had a slightly larger stable region than the other two methods. The stability diagram shown was created with the spectral element method using twelve mesh points.

The convergence plot shown in Fig. 4.8b was created using the point $(\alpha, \beta) = (20, 20)$ which is in the stable region. This point was selected due to its sensitivity to convergence and its proximity to the stability border. The results are summarized in Table 4.1 with the spectral element method converging with the smallest computational dimension of twelve mesh points. The semi-discretization method, however, does not converge when using less than 50 intervals or even up to 200 intervals. A line was fitted to the absolute error of the semi-discretization method using least squares and found that more than 1×10^7 intervals are required for convergence. The convergence rate of both the zeroth and first order semi-discretization methods are compared in Fig. 4.9. While the first order method does have slightly improved convergence properties over the zeroth method, both clearly converge linearly.

The results of the relative computational time comparison are summarized in Table 4.1 with the Legendre collocation method requiring the least amount of time at 12.0 seconds. Since the semi-discretization method does not converge when using less than 50 intervals in this case, any choice of intervals less than 50 would be arbitrary. Twenty-one intervals were selected which is the same number of collocation points required by the Legendre collocation method to converge.

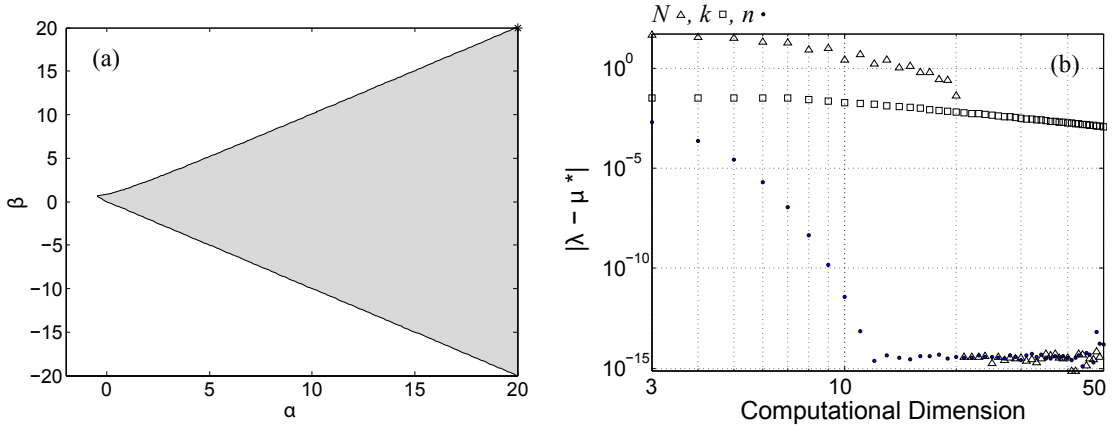

FIGURE 4.8: The stability diagram for Equation (4.34) and the convergence plots for the point $(\alpha, \beta) = (20, 20)$. In graph (a) the stable region is shaded, the unstable region is unshaded, and the point used for the convergence is indicated with a star. Graph (b) shows the convergence of the maximum eigenvalue as a function of the computational dimension of (1) the Legendre collocation method (triangles), (2) the semi-discretization method (squares), and (3) the spectral element method (dots).

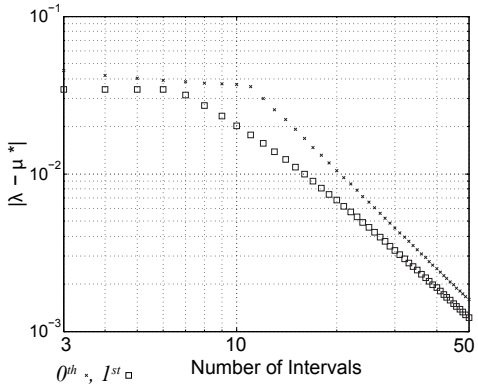

FIGURE 4.9: Convergence plot for the point $(\alpha, \beta) = (20, 20)$ comparing the zeroth and first order semi-discretization methods. The graph shows the convergence of the maximum eigenvalue as a function of the computational dimension of (1) the zeroth order semi-discretization method (x's) and (2) the first order semi-discretization method (squares). Notice both methods show linear convergence rate, but neither method reaches convergence in the plot (convergence occurs at about 1×10^{-15}).

Table 4.1: For the ship stability in Eq. (4.34), the minimum computational dimension required to achieve convergence and the computational time required to calculate the stability diagram is summarized.

Method	Computational Dimension	Computational Time (sec)
Semi-discretization	21+	47.1
Spectral element	12	15.6
Legendre collocation	21	12.0

4.3.2 Delayed damped Mathieu equation

The delayed damped Mathieu Equation (DDME) is an adaptation of the original equation proposed by Mathieu in the study of elliptical membranes (Mann and Patel, 2010). The DDME has become a standard equation for comparing and evaluating delay methods. The equation in its full form of

$$\ddot{x}(t) + \kappa\dot{x}(t) + \left(\delta + \epsilon \cos\left(\frac{2\pi t}{T}\right)\right) x(t) = bx(t-\tau) \tag{4.36}$$

is a second order, linear, non-autonomous, single-delayed differential equation. The state space matrices, $\mathbf{A}(t)$ and $\mathbf{B}(t)$, for the DDME are given by

$$\mathbf{A} = \begin{bmatrix} 0 & 1 \\ -\left(\delta + \epsilon \cos\left(\frac{2\pi t}{T}\right)\right) & -\kappa \end{bmatrix}, \quad \mathbf{B} = \begin{bmatrix} 0 & 0 \\ b & 0 \end{bmatrix}. \tag{4.37}$$

The DDME is commonly used because it contains many of the intricacies faced by delayed methods in a concise form. In addition, closed form stability charts are available for the DDME which makes it attractive for validating numerical methods (Insperger and Stepan, 2002, 2003).

The DDME can be viewed as a more complex form of a simple oscillator. From this point of view, κ represents the damping coefficient, and δ represents the stiffness coefficient. The additional term $\epsilon \cos\left(\frac{2\pi t}{T}\right)$ represents a periodic fluctuation of the stiffness coefficient with a period of T. The final delay term $bx(t-\tau)$ can be viewed as

delayed feedback or hysteresis. In the following comparisons, a damping coefficient κ of 0.1, a delay τ and period T of 2π, and an amplitude ϵ of 2 are included.

The stability diagram for this system is shown in Fig. 4.10a with a 100x100 grid in δ, b parameter space. The stability plot was generated using each method with nearly identical results. The stability plot shown was created with the spectral element method using twenty-four mesh points.

The convergence plot shown in Fig. 4.10b was created using the point $(\delta, b) = (5, 1)$. This point was selected due to its proximity to the stability border. The results are summarized in Table 4.2 with the spectral method converging with the smallest computational dimension of twenty-four mesh points. The semi-discretization method does not converge when using less than 50 intervals or even up to 200 intervals. The results of the relative computational time comparison are summarized in Table 4.2 with the Legendre collocation method requiring the least amount of time at 44.6 seconds. Since the semi-discretization method does not converge with fewer than 50 intervals, the same number of intervals (thirty-eight) was selected as collocation points used by the Legendre collocation method.

Table 4.2: For the DDME in Eq. (4.36), the minimum computational dimension required to achieve convergence and the computational time required to calculate the stability diagram is summarized.

Method	Computational Dimension	Computational Time (sec)
Semi-discretization	38+	123.0
Spectral element	24	68.3
Legendre collocation	38	44.6

4.3.3 Helicopter rotor

Time periodic equations are used to model the flapping of an individual rotor blade in the forward motion of helicopters, and several studies have investigated the stability

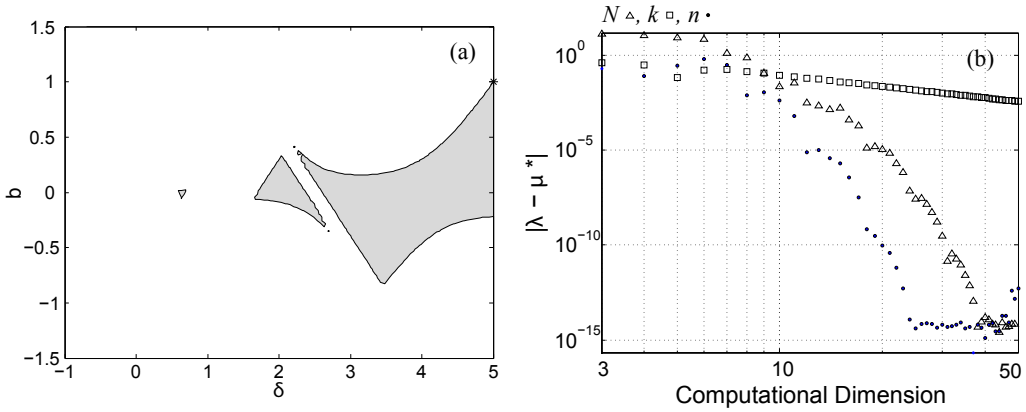

FIGURE 4.10: The stability diagram for Equation (4.36) and the convergence plots for the point $(\delta, b) = (5, 1)$. In graph (a) the stable regions are shaded, the unstable regions are unshaded, and the point used for the convergence is indicated with a star. Graph (b) shows the convergence of the maximum eigenvalue as a function of the computational dimension of (1) the Legendre collocation method (triangles), (2) the semi-discretization method (squares), and (3) the spectral element method (dots).

of helicopter blades in forward motion. The focus in these studies was on designing a control scheme that would attenuate the vibrations (flapping) of the rotor blade. The attenuation of these vibrations improves the ride comfort, reduces fatigue in the rotor, and protects the aircraft's equipment from damage (Arcara et al., 2000).

One control strategy is to control the rotor using measurements obtained from each rotor blade individually. For example, Pandyian and Sinha used Liapunov-Floquet transformation to design an algorithm that controlled the helicopter's individual blade flapping motion (Pandiyan and Sinha, 1999). Arcara et al. designed an individual blade control framework based on the measurements of the acceleration, or the vibratory loads each blade transmits to the rotor hub, taken at various locations on each blade (Arcara et al., 2000).

In this study, a delay feedback strategy is explored as a possible alternative for controlling flapping in helicopter blades based on the model in Pandiyan and Sinha (1999). However, instead of using the blade pitch as the control input, a control term is introduced based on the flapping of the blade on the previous rotor revolution.

The resulting variational equation for the flapping of the rotor blade with a delayed feedback is

$$\dot{\theta}(t) = \mathbf{A}(t)\theta(t) + \mathbf{B}(t)\theta(t-T)\,, \tag{4.38}$$

where the over dot denotes a differentiation with respect to time, $\theta(t)$ is the flapping of the rotor blade about the periodic solution, and $T = 1$ is the period of one rotor revolution. The matrix $\mathbf{A}(t)$ is the system matrix while $\mathbf{B}(t)$ is the matrix of gains associated with the delayed feedback term. The elements of the matrices $\mathbf{A}(t)$ and $\mathbf{B}(t)$ can be written as

$$\mathbf{A} = \begin{bmatrix} 0 & 1 \\ -(2\pi)^2\left\{1 + \omega_F^2 + \gamma\left(\frac{\mu}{6}\cos 2\pi t + \frac{\mu^2}{8}\sin 4\pi t\right)\right\} & -2\pi\gamma\left(\frac{1}{8} + \frac{\mu}{6}\sin 2\pi t\right) \end{bmatrix},$$

$$\mathbf{B} = \begin{bmatrix} 0 & 0 \\ c_1 & c_2 \end{bmatrix}, \tag{4.39}$$

where ω_F is the non-rotating flap frequency, γ is the Lock number (the ratio of the aerodynamic forces to inertia forces in the blade), μ is the rotor advance ratio of the forward speed to the rotor tip speed, and c_1 and c_2 are the gains for the feedback control signal. Following Pandiyan and Sinha (1999), the design parameters are $\omega_F = 0.4$ rad/s, $\gamma = 5$, and $\mu = \{0.3, 0.75, 1.2\}$. The stability of the system is studied in the gains parameter space (c_1, c_2).

The stability diagrams for this system are shown in Fig. 4.11a, c, and e with a 100x100 grid in $c1$, $c2$ parameter space for all three plots. The stability plot was generated using each method with nearly identical results. The semi-discretization method generated a diagram that had a slightly smaller stable region than the other two methods. The stability plots shown were created with the spectral element method using twenty, twenty-seven, and twenty-nine mesh points for $\mu = 0.3$, $\mu = 0.75$, $\mu = 1.2$, respectively.

The convergence plots shown in Fig. 4.11b, d, and f were created using the points $(c1, c2) = (0, 4.25)$, $(c1, c2) = (0, 3)$, and $(c1, c2) = (0, 1)$, respectively. These points were selected due to their proximity to the stability border. In Fig. 4.11f, collocation points were plotted up to sixty to demonstrate convergence more clearly. The spectral method converges with the smallest computational dimension for each set of parameters as summarized in Table 4.3. The semi-discretization method, however, does not converge with fewer than 50 intervals or even up to 200 intervals for any of the values of μ.

The of results of the relative computational time comparison are summarized in Table 4.3. For each set of parameters, the Legendre collocation method requires the least amount of time. Since the semi-discretization method does not converge when using less than 50 intervals, the same number of collocation points required by the Legendre collocation method to reach convergence were selected.

Table 4.3: The minimum computational dimension to achieve convergence and the computational time required to calculate the stability diagram for Equation (4.38). The computational time for each method was calculated for the associated computation dimension in the table.

	Method	Computational Dimension	Computational Time (sec)
$\mu = 0.3$	Semi-discretization	35+	115.2
	Spectral element	20	41.9
	Legendre collocation	35	38.0
$\mu = 0.75$	Semi-discretization	42+	184.1
	Spectral element	27	88.7
	Legendre collocation	42	57.0
$\mu = 1.2$	Semi-discretization	45+	200.9
	Spectral element	29	101.3
	Legendre collocation	45	66.6

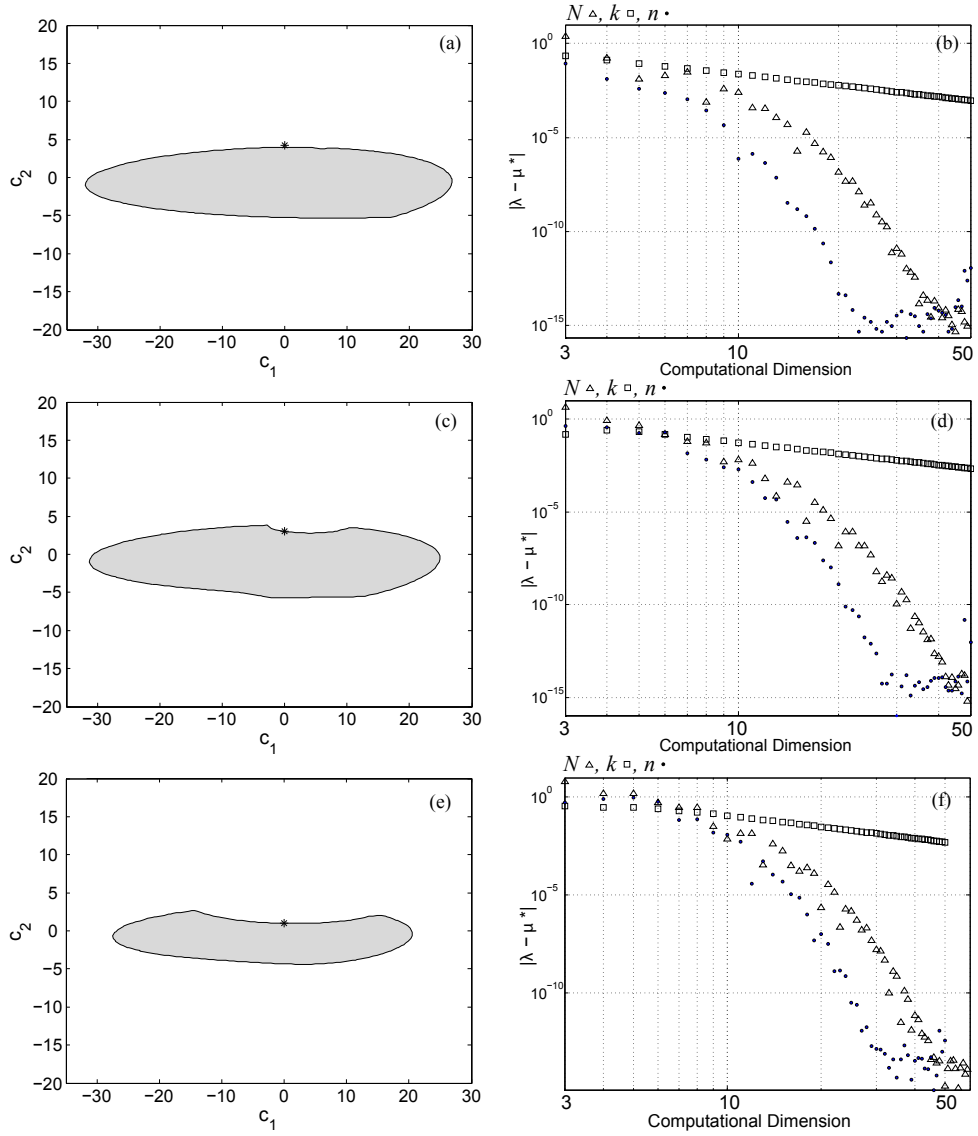

FIGURE 4.11: The stability diagrams for Eq. (4.38) with $\mu = 0.3$ (a), $\mu = 0.75$ (c), and $\mu = 1.2$ (e). The convergence plots for the (c_1, c_2) points are (0,4.25) for $\mu = 0.3$ (b), (0,3.0) for $\mu = 0.75$ (d), and (0,1.0) for $\mu = 1.2$ (f). In graphs (a), (c), and (e) the stable regions are shaded, the unstable regions are unshaded, and the point used for the convergence is indicated with a star. Graphs (b), (d), and (f) show the convergence of the maximum eigenvalue as a function of (1) the number of collocation points in the Legendre collocation method (triangles), (2) the number of intervals in the semi-discretization method (squares), and (3) the order of the Lagrange trial functions of the spectral element method (dots).

4.4 Conclusions

In this chapter, the implementations of the semi-discretization, spectral element, and Legendre collocation methods were presented and contrasted. While each of these methods has been used to study various DDEs, a comparison among these methods has yet to appear in the literature. The methods were compared for relative convergence rate and computational time using three numerical studies consisting of a ship stability example, the delayed damped Mathieu equation, and a helicopter rotor control problem.

The semi-discretization method is based on discretizing the period and delay into uniform intervals. Because this method relies on increasing the number of uniform intervals to reach convergence, it was expected that the method will converge at a linear rate (i.e. "h-convergence") even for higher order implementations. Both the spectral element and Legendre collocation methods rely on increasing the order of the polynomials to achieve convergence. It was therefore expected that these methods will converge exponentially (i.e. "p-convergence"). Both expectations were realized in the numerical studies. The semi-discretization method demonstrated a linear rate of convergence, while both the spectral element and Legendre collocation methods converged at an exponential rate.

Three numerical studies with second order, continuous, linear, single-delayed differential equations were used to compare the convergence rate and the relative computational time between the Legendre collocation, semi-discretization, and spectral element methods. The spectral element method was found to have the quickest convergence rate for all three studies, but the Legendre collocation method had the shortest computational time. The semi-discretization method did not converge when using less than 50 intervals for any of the numerical studies and required the longest computational for all three studies.

In cases where the convergence rate is the most important aspect, the spectral element method should clearly be used. In the studies, the spectral element method converged with about a 36% smaller computational dimension than the Legendre collocation method. In computational terms, a quicker convergence rate leads to using less memory for calculations. Smaller computational dimensions results in smaller monodromy matrices which leads to using less memory. Memory usage is an important factor for high dimensional systems or complicated systems that require a finer mesh.

In cases where memory is not an issue, the Legendre collocation method becomes attractive because of its relative speed. The Legendre collocation method requires fewer calculations than the spectral element method and therefore tends to require less computational time. For all three studies, the Legendre collocation method was about 10% to 56% faster than the spectral element method.

In this chapter all examples assumed that the delay was equal to the period (i.e. $\tau = T$). Systems do exists where the delay is several periods long, distributed, or arbitrary. For instance, the DDME in Section 4.3.2 can be implemented using long or arbitrary delays. However, including long, distributed, or arbitrary delays complicates the comparison between the methods and are out of the scope of this chapter. The semi-discretization method (Insperger and Stpn, 2011) and spectral element method (Khasawneh and Mann, 2010) are capable of handling long, distributed, and arbitrary delays. The authors are not aware of a paper extending the Legendre collocation method to arbitrary delays, but it could be extended by implementing the same techniques used for the spectral element method. Future studies in which long, distributed, and arbitrary delays are compared would be a welcome follow-up.

Excerpts reprinted from Journal of Sound and Vibration, Vol 331(17), Dennis J. Tweten, Genevieve M. Lipp, Firas A. Khasawneh, and Brian P. Mann, "On the comparison of semi-analytical methods for the stability analysis of delay differential

equations," Pages No. 40574071, Copyright (2012), with permission from Elsevier.

5

Chaos Control of Forced Systems

Controlling chaos via the stabilization of unstable periodic orbits (UPOs) embedded in strange attractors was first demonstrated by Ott et al. (1990) and is often referred to as OGY control. Shortly thereafter the method of using delayed feedback to stabilize UPOs was introduced by Pyragas (1992). In the initial implementation of delayed feedback control (DFC), a proportional feedback from a single delay was utilized to stabilize a UPO. This method works well to stabilize period-1 UPOs, but the method often fails to stabilize orbits with longer periods (Pyragas, 1995). In addition, DFC has been used for steady-state control in chaotic systems. However, in recent years, alternative approaches such as multiple delay feedback control (MDFC), have been demonstrated to be more effective in stabilizing steady-states (Scholl and Schuster, 2008).

To improve the DFC method, Socolar introduced the extended delayed feedback control (EDFC) method which uses an infinite number of delays while still implemented with a single delay line (Socolar et al., 1994). The EDFC method has been demonstrated to stabilize UPOs with larger periods (Socolar et al., 1994; Pyragas,

1995). The key to analyzing either method is to determine the Floquet exponents (FEs) of the UPO while under the influence of control. The chief method to calculate the FEs in these first papers was an integration technique by Benettin (Pyragas, 1995; Benettin et al., 1979). The Benettin method is used to identify the largest one or two FEs, but because it relies on increasing the duration of integration to improve accuracy, it is not ideal. In addition, the Benettin method does not provide the imaginary part of the FE.

Advanced techniques using Floquet theory and variational methods have resulted in both approximate (Just et al., 1997) and exact (Pyragas, 2006) methods to determining the FEs of UPOs. These methods greatly improve the ease of determining the FEs by simplifying the delay differential equations (DDEs) into non-autonomous ordinary differential equations (ODEs) (Pyragas, 2006). However, the resulting simplification requires one to solve a transcendental eigenproblem. The fact that the variation ODE has non-autonomous coefficients is an additional complication. Pyragas and Just attempted to overcome these complications by assuming the form of the FEs (Pyragas, 2006; Just et al., 1997). However, this method is mainly limited to UPOs resulting from period-doubling bifurcations and low dimensional systems (Pyragas, 2006). Another recent approach using variational equations was introduced by Tamaševičius et al. (2007). In this method, the time dependent transcendental eigenproblem is reduced to a time independent transcendental eigenproblem by using the time average of the stabilized UPO, but it is limited to weakly nonlinear, symmetrical systems (Tamaševičius et al., 2007).

Rather than simplifying the DDEs to ODEs, the DDEs can be solved directly. Analytical solutions to DDEs for weakly nonlinear systems have been developed using the Lambert function (Amann et al., 2007). In addition, a number of numerical methods have recently been added to the literature including the semi-discretization (Insperger et al., 2008), collocation (Butcher and Bobrenkov, 2011), and spectral

element (Khasawneh and Mann, 2011b) methods. Each of these numerical techniques has been compared using the delayed Mathieu equation (Tweten et al., 2012) for which analytical solutions have been developed (Insperger and Stepan, 2002).

In this chapter, a new method for determining the FEs of UPOs stabilized by EDFC is introduced which is an adaptation of the spectral element method. The spectral element method approximates the infinite dimensional solution to delay differential equations (DDEs) with a finite dimensional solution. The spectral approach does not require any assumptions regarding the form of the FE, determines both the real and imaginary parts of the FEs, and can be applied to highly nonlinear and high-dimensional systems. In addition, the spectral method can be used to analyze systems whose UPOs arise from bifurcations other than period doubling. The spectral approach requires numerical integration over the period of the UPO but utilizes quadrature weights which are calculated only once.

This chapter is organized in the following way. The first section provides a brief overview of the EDFC method followed by a section describing the implementation of the spectral element method. Simulated examples are then presented using an experimental approach to demonstrate how the EDFC and the spectral element method can be implemented for experiments. Finally, the conclusions are presented.

5.1 Extended Delayed Feedback Control

In many chaotic systems, the EDFC method is capable of stabilizing UPOs by applying proportional delayed feedback. The power of the feedback approaches zero once the desired UPO is stabilized (Pyragas, 2006). A nonlinear system can be defined by

$$\dot{\mathbf{x}} = \mathbf{f}(\mathbf{x}, t)\,, \tag{5.1}$$

where $\mathbf{x}$ is a vector of d states and $\mathbf{f}$ is a function of those states and time.

In order to predict whether a particular UPO can be stabilized using the EDFC method, the nonlinear equations must be represented in the variational form

$$\delta\dot{\mathbf{x}} = \mathbf{A}(t)\delta\mathbf{x}\,, \tag{5.2}$$

$$\mathbf{A}(t) = \mathbf{Df}(\mathbf{x}_o(t), t)\,, \tag{5.3}$$

where $\mathbf{x}_o(t)$ is the UPO, $\delta\mathbf{x}$ is the deviation from the UPO, and $\mathbf{A}$ is the $d\times d$ Jacobian. Both the UPO and the Jacobian are periodic with period T that is $\mathbf{x}_0(t) = \mathbf{x}_0(t+T)$ and $\mathbf{A}(t) = \mathbf{A}(t+T)$, respectively. Using Floquet theory, the deviation $\delta\mathbf{x}$ can be represented by

$$\delta\mathbf{x} = \mathbf{u}(t)\mathrm{e}^{\lambda t}\,, \tag{5.4}$$

where $\mathbf{u}(t) = \mathbf{u}(t+T)$ is a periodic solution and λ is the FE (Pyragas, 2006). An UPO has at least one positive FE.

The feedback is applied by an external feedback $\mathbf{F}(t)$ defined by

$$\delta\dot{\mathbf{x}} = \mathbf{A}(t)\delta\mathbf{x} + \mathbf{F}(t)\,, \tag{5.5}$$

$$\mathbf{F}(t) = \mathbf{K}\left[(1-R)\sum_{r=1}^{\infty} R^{r-1}\mathbf{x}(t-r\tau) - \mathbf{x}(t)\right], \tag{5.6}$$

where $\mathbf{K}$ is the matrix of proportional gains and R determines the influence of previous delays on the feedback (Pyragas, 1995). Note that if $R = 0$, EDFC reduces to DFC in which only a single delay affects the control. The matrix $\mathbf{K}$ can include feedback from and apply control to all the states; however, in many cases control is applied using only one state.

The EDFC method may have difficulty stabilizing UPOs with an odd number of FEs with positive real parts; however, it has been demonstrated that this is not a true limitation of the EDFC method (Fielder et al., 2007; Just et al., 2007). Adding an additional FE with a positive real part has been shown to overcome this difficulty (Tamaševičius et al., 2007). Hovel and Socolar (2003) demonstrated limitations of

the EDFC method in the presence of latencies in the delay signal. The EDFC method is not strictly limited to stabilizing systems with small Lyapunov exponents, but the range of gains that stabilize systems with large Lyapunov exponents can be very limited (Just et al., 1999b).

5.2 Spectral Element Method

The spectral element method is a numerical technique of approximating the infinite dimensional solution of DDEs by a finite dimensional system (Khasawneh and Mann, 2011b). The method is based on the method of weighted residuals and is a convenient way of determining the stability of delay systems.

A general DDE for a linearized or variational system with multiple delays is given by

$$\dot{\mathbf{x}}(t) = \mathbf{A}(t)\mathbf{x}(t) + \sum_{r=1}^{n_\tau} \mathbf{B}_r(t)\mathbf{x}(t-\tau_r), \tag{5.7}$$

where $\mathbf{x}(t)$ is a column vector of d states, $\mathbf{A}(t)$ is the $d \times d$ Jacobian, τ_r is the duration of the r^{th} delay, the delay matrices $\mathbf{B}_r(t)$ are the dependencies of the states on the delayed states $\mathbf{x}(t-\tau_r)$, n_τ is the number of delays, and τ_{n_τ} is the duration of the longest delay. In general, the Jacobian $\mathbf{A}(t)$ will be a function of the UPO of interest which makes the DDE non-autonomous. In addition, the Jacobian and the delay matrices $\mathbf{B}_r$ are periodic so that $\mathbf{A}(t) = \mathbf{A}(t+T)$ and $\mathbf{B}_r(t) = \mathbf{B}_r(t+T)$. When control is implemented for more than one state or for cross coupling, the matrix $\mathbf{K}$ will have more than one non-zero entry. In either of these cases, the Jacobian will include gain terms in more than one element, and the delay matrices are created by premultipling a matrix of the delay terms on the diagonal with the matrix $\mathbf{K}$. The second example in Section 5.3 demonstrates this more general case.

The stability of a UPO can be determined from the eigenvalues of the monodromy operator of the system. The monodromy operator maps the delay states from the

segment $[-\tau_{n_\tau}, 0]$ to the current period $[0, T]$, and the operator's eigenvalues are the Floquet multipliers of the UPO. However, the monodromy operator acts on an infinite dimensional state space so it is impractical to deal with the operator directly (Khasawneh and Mann, 2011b). The spectral element method approximates the infinite dimensional monodromy operator with a finite dimensional monodromy matrix $\mathbf{U}$ (Khasawneh and Mann, 2011b). The monodromy matrix maps a finite number of states by

$$\mathbf{x}_m = \mathbf{U}\mathbf{x}_{m-1}\,, \tag{5.8}$$

where $\mathbf{U}$ maps the states $\mathbf{x}_{m-1}$ from the time segment $[-\tau_{n_\tau}, 0]$ onto the states $\mathbf{x}_m$ which includes the period $[0, T]$ (Khasawneh and Mann, 2011b). The spectral approach requires that the equations of the system be arranged in a variational form so that each state is the deviation from the UPO, and the monodromy matrix then becomes a function of the UPO. The eigenvalues of the monodromy matrix in this form $\mathbf{U}(t, \mathbf{x}_0(t))$ are the Floquet multipliers of the UPO which includes both real and imaginary terms. The Floquet multipliers are related to the FEs by

$$\mu = \exp(\lambda T)\,, \tag{5.9}$$

where λ is the FE and $\mathbf{x}_0(t)$ is the UPO.

The first step in applying the spectral element method to EDFC is to approximate the solution using polynomial trial functions ϕ_i given by

$$\mathbf{x}_j(t) = \sum_{i=1}^{n+1} \mathbf{x}_{j,i}\,\phi_i(\eta), \tag{5.10a}$$

$$\mathbf{x}_j(t - r\tau) = \sum_{i=1}^{n+1} \mathbf{x}_{j,i-rn}\,\phi_i(\eta)\,, \tag{5.10b}$$

where ϕ_i is the trial function, η is the local time normalized from 0 to 1 for the element j, r is a particular delay, and τ is the delay equal to the period of the

UPO (Khasawneh and Mann, 2010). The vector $\mathbf{x}_{j,i}(t)$ is the value of the states of the j^{th} element at the i^{th} node (Khasawneh and Mann, 2011b). A total of $n+1$ interpolation nodes are used for each element. In general, the spectral element method can be implemented with an arbitrary delay, but for forced systems the delays will be multiples of the forcing period. The solution can also be broken into multiple elements of arbitrary duration. However, while the notation for multiple elements is included in this chapter, the examples will be implemented with one element.

The Legendre-Gauss-Lobatto (LGL) points were selected for the interpolation nodes. The LGL nodes are computed from the roots of the polynomial $(1-u^2)L'_n(u)$ where $L_n(u)$ is the n^{th} order Legendre function, $L'_n(u)$ is the first derivative of $L_n(u)$ with respect to u, and u is on the segment $[-1,1]$ (Khasawneh and Mann, 2011b). The LGL nodes must therefore be shifted to be on the segment $[0,1]$ in order to be compatible with Eq. (5.10). The trial functions ϕ_i can be found using the barycentric Lagrange formula

$$\phi_i(t) = \frac{\frac{\rho_i}{t-t_i}}{\sum_{j=1}^{n+1} \frac{\rho_j}{t-t_j}}\,, \tag{5.11}$$

and the barycentric weights ρ_i given by

$$\rho_i = \frac{1}{\prod_{k=1,k\neq i}^{n+1} (t_i - t_k)},\ k = 1,2,\ldots,n+1\,, \tag{5.12}$$

where t_i and t_k represent time at the i^{th} and k^{th} nodes, respectively (Higham, 2004). The barycentric Lagrange interpolation used in Eq. (5.11) improves the numerical stability of larger meshes when compared to the more commonly used Lagrangian interpolation (Berrut and Trefethen, 2004). The trial functions have the useful prop-

erty

$$\phi_i(t_k) = \delta_{i,k}\,,\ t_k \in \{t_i\}_{i=1}^{n+1}\,, \tag{5.13}$$

which means the combined term $\mathbf{x}_{j,i}\,\phi_i(\eta)$ is the value of the states at each node. The derivatives of the trial functions can also be calculated using the barycentric formula as

$$\phi_i'(t_k) = \begin{cases} \frac{\rho_i/\rho_k}{t_i - t_k}, & i \neq k \\ \sum\limits_{i=0, i\neq k}^{n+1} \frac{-\rho_i/\rho_k}{t_i - t_k}, & i = k. \end{cases} \tag{5.14}$$

For a matrix $\mathbf{D}$ with elements $D_{ki} = \phi_i'(t_k)$, the derivative of a vector of states $\mathbf{z}$ on a mesh of LGL nodes is given by $\mathbf{z}\,' = \mathbf{D}\mathbf{z}$ (Khasawneh and Mann, 2011b).

A nonlinear DDE in variational form can now be approximated with polynomial test functions by substituting Eqs. (5.10)(5.13)(5.14) into Eq. (5.7). The method of weighted residuals is then used to minimize the error of the polynomial approximation by setting the approximate DDE to zero and integrating over the duration of each element (Khasawneh and Mann, 2011b). The method of weighted residuals requires multiplication of the approximate solution by a test function for which Legendre polynomials were selected. The resulting integration is given by

$$\begin{aligned} \int_0^1 \Bigg(& \frac{1}{t_j}\mathbf{x}_{j,i}\,\phi_i'(\eta) - \mathbf{A}(t_\eta)\mathbf{x}_{j,i}\,\phi_i(\eta) \\ & - \sum_{r=1}^{n_\tau} \mathbf{B}_r(t_\eta)\mathbf{x}_{j,i-rn}\,\phi_i(\eta) \Bigg)\,\psi_p(\eta)\,\mathrm{d}\eta = 0, \end{aligned} \tag{5.15}$$

where $\psi_p(\eta)$ is the p^{th} Legendre polynomial, η is the normalized time in each element, and $t_\eta = (\eta + j - 1)t_j$.

The speed of the integration is increased by using by using quadrature weights rather than symbolic integration. The numerical integration of a function by quadra-

ture weights is given by

$$\int_0^1 f(\eta)\,\mathrm{d}\eta \approx \sum_{k=1}^{n+1} w_k f(\eta_k), \tag{5.16}$$

where w_k is the quadrature weight and η_k is the localized time at the node k. For a grid of LGL points, the quadrature weights (Parter, 1999) are given by

$$w_k = \begin{cases} \frac{2}{n(n+1)} & k = 1, n+1 \\ \frac{2}{n(n+1)(L_n(\eta_k))^2}, & \text{otherwise}\,. \end{cases} \tag{5.17}$$

Quadrature weights are calculated in advanced and reused for each integration.

Implementing the method of weighted residuals with quadrature rates results the following equation

$$\begin{bmatrix} \mathbf{I} & \mathbf{0} & \dots & \mathbf{0} \\ \mathbf{N}^1_{j,i} & \mathbf{N}^1_{j,i+1} & \dots & \mathbf{N}^1_{j,i+n} \\ \mathbf{N}^2_{j,i} & \mathbf{N}^2_{j,i+1} & \dots & \mathbf{N}^2_{j,i+n} \\ \vdots & \vdots & \ddots & \vdots \\ \mathbf{N}^n_{j,i} & \mathbf{N}^n_{j,i+1} & \dots & \mathbf{N}^n_{j,i+n} \end{bmatrix} \begin{bmatrix} \mathbf{x}_{j,i} \\ \mathbf{x}_{j,i+1} \\ \vdots \\ \mathbf{x}_{j,i+n} \end{bmatrix} =$$

$$\begin{bmatrix} \mathbf{0} & \dots & \mathbf{0} & \mathbf{0} & \dots & \mathbf{0} & \mathbf{I} \\ \mathbf{P}^1_{j,i-rn} & \dots & \mathbf{P}^1_{j,i-rn+n} & \mathbf{P}^1_{j,i-n(r-1)+1} & \dots & \mathbf{P}^1_{j,i-1} & \mathbf{P}^1_{j,i} \\ \mathbf{P}^2_{j,i-rn} & \dots & \mathbf{P}^2_{j,i-rn+n} & \mathbf{P}^2_{j,i-n(r-1)+1} & \dots & \mathbf{P}^2_{j,i-1} & \mathbf{P}^2_{j,i} \\ \vdots & \ddots & \vdots & \vdots & \ddots & \vdots & \vdots \\ \mathbf{P}^n_{j,i-rn} & \dots & \mathbf{P}^n_{j,i-rn+n} & \mathbf{P}^n_{j,i-n(r-1)+1} & \dots & \mathbf{P}^n_{j,i-1} & \mathbf{P}^n_{j,i} \end{bmatrix} \begin{bmatrix} \mathbf{x}_{j,i-kn} \\ \vdots \\ \mathbf{x}_{j,i-rn+n} \\ \mathbf{x}_{j,i-n(r-1)+1} \\ \vdots \\ \mathbf{x}_{j,i-1} \\ \mathbf{x}_{j,i} \end{bmatrix}. \tag{5.18}$$

The matrices $\mathbf{N}$ and $\mathbf{P}$ are sub-matrices of matrices $\mathbf{H}$ and $\mathbf{G}$, respectively. The sub-matrix $\mathbf{I}$ is the $d \times d$ identity matrix. These elements are defined by

$$\mathbf{N}^p_{j,i} = \sum_{k=1}^{n+1} \left(\frac{1}{t_j} \mathbf{I} \phi_i'(\eta_k) \psi_p(\eta_k) w_k \right) - \mathbf{A}(t_\eta) \psi_p(\eta_i) w_i \tag{5.19a}$$

$$\mathbf{P}^p_{j,i-rn} = \mathbf{B}_r(t_\eta) \psi_p(\eta_i) w_i \tag{5.19b}$$

where all elements are $d \times d$ matrices (Khasawneh and Mann, 2011b). The indexes j refers to the j^{th} element, i to the i^{th} node, and p to the p^{th} order Legendre polynomial. The $\mathbf{N}$ matrices are defined by the upper half of Eq. (5.15) on the period $[0, T]$, and the $\mathbf{P}$ matrices are defined by the lower half of Eq. (5.15) on the delay periods. Equation (5.18) can be simplified to

$$\mathbf{H}\mathbf{x}_m = \mathbf{G}\mathbf{x}_{m-1}\,, \tag{5.20}$$

where $\mathbf{x}_m$ includes only the states in the period $[0, T]$ and $\mathbf{G}$ and $\mathbf{H}$ are of unequal size if more than one delay is included.

The final step to determine the FE of the DDEs in Eq. (5.7) is to construct the monodromy matrix $\mathbf{U}$ from Eq. (5.8). Using the matrices $\mathbf{G}$ and $\mathbf{H}$ and mapping identical states results in

$$\mathbf{U}(\mathbf{x}_0(t), t) = \begin{bmatrix} \mathbf{0}_{D_3 \times d \cdot E \cdot n} & \mathbf{I}_{D_3 \times D_3} & \mathbf{0}_{D_3 \times d} \\ & \mathbf{H}^{-1}\mathbf{G} & \end{bmatrix} \tag{5.21}$$

where $D_1 = d(1 + n \cdot E)$, $D_2 = d(n_\tau \cdot E \cdot n + 1)$, $D_3 = D_2 - D_1$, and the size of $\mathbf{H}^{-1}\mathbf{G}$ is $D_1 \times D_2$. The vector $\mathbf{x}_m$ includes states in the period $[0, T]$ and enough delay states to be of equal length as $\mathbf{x}_{m-1}$. The added delay states in $\mathbf{x}_m$ is required to make the monodromy matrix square. The additional states are mapped directly to the identical states in $\mathbf{x}_{m-1}$ through the identity matrix $\mathbf{I}_{D_3 \times D_3}$.

5.3 Examples

The analog implementation of the EDFC method incorporates an infinite number of delays for values of $R > 0$ using a single delay line. However, when applying the spectral approach to approximate a system with EDFC, only a finite number of delays is practical. The limitation of a finite number of delays is not intractable since the influence of longer delays decrease exponentially.

Keeping with an experimental approach, the number of grid points $n+1$ and number of delays n_τ for each example were chosen using the following strategy. Starting with the case $R = 0$ where only one delay is required, the number of grid points was increased until the plot of the maximal FE versus the gain no longer changed with additional grid points. At the maximal number of grid points, the approximation was considered converged. This number of grids points for plots were used for cases where $R > 0$. For each value of R, the number of delays n_τ were increased until the maximal Floquet exponent curve no longer changed with additional delays.

An experimental approach was also selected for extracting the UPOs from the simulated results. The equations were simulated for 5×10^5 units of time and sampled 100 times per forcing period. Potential UPOs were identified by using a procedure similar to the one proposed by Lathrop and Kostelich (1989). The absolute value of the difference of the states between the beginning and end of an orbit period where compared to a percentage of the maximum variation in each state. These comparisons were carried out for each data point for a subset of the total simulation. In cases where the difference of each state was less than 5% of the total range for each state, the time span was identified as a potential UPO. Identified UPOs were grouped by shape and period. The UPOs in each group were approximated by a Fourier series and the coefficients of the series were averaged. The resulting averaged Fourier series provided good approximations of the UPOs in each example.

It should be noted that the spectral element approach for EDFC is not limited to the Duffing equation. Systems based on the Duffing equation were chosen because they are well known and are common in physical systems. The equations for a

Duffing system under EDFC control is given by

$$\dot{x} = y \tag{5.22a}$$

$$\dot{y} = -\mu y + \beta_1 x - \beta_3 x^3 + a\cos(\Omega t) + F(x, y, t) \tag{5.22b}$$

where μ is the damping; β_1 and β_3 are the restoring force coefficients; a is the forcing amplitude; and Ω is the forcing frequency.

The first example is a Duffing system used by Pyragas (1995) to demonstrate the capability of EDFC to stabilize orbits that could not be stabilized by DFC. The control input for this example is

$$F(x, y, t) = K\left[(1 - R)\sum_{r=1}^{\infty} R^{r-1} y(t - r\tau) - y(t)\right], \tag{5.23}$$

where the control is based solely on the state y. The Jacobian $\mathbf{A}$ and the delay matrices $\mathbf{B}_r$ are given by

$$\mathbf{A} = \begin{bmatrix} 0 & 1 \\ \beta_1 - 3\beta_3 x_0^2(t) & -\mu - K \end{bmatrix}, \tag{5.24a}$$

$$\mathbf{B}_r = \begin{bmatrix} 0 & 0 \\ 0 & KR^{r-1}(1 - R) \end{bmatrix}, \tag{5.24b}$$

where $x_0(t)$ is the position of the desired UPO and r is the number of periods T in each delay. In Figs. 5.1a and 5.1b, the maximal Floquet exponent is plotted versus the gain K with $R = 0$, 0.2, 0.4, 0.6, and 0.8 for a period-1 and period-3 UPO, respectively. A total number of 55 nodes were used for the period-1 UPO and 60 nodes for the period-3 UPO. The UPO is plotted as an insert in the upper right corner of each figure with x as the independent variable and y as the dependent variable. Both figures show excellent agreement with Pyragas (1995). The control parameters that stabilized both UPOs are listed in Table 5.1. The stable gains were taken from Fig. 5.1 and rounded to the nearest hundredth.

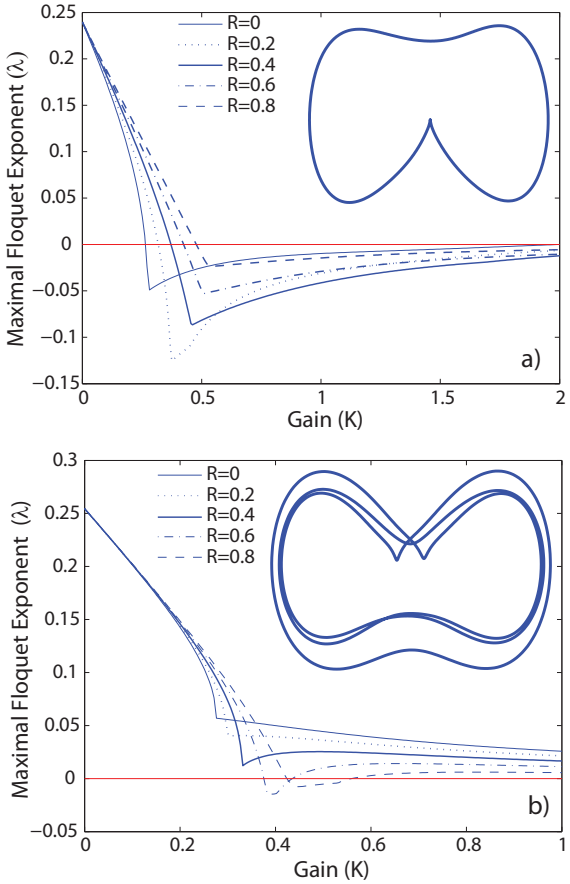

FIGURE 5.1: Example 1: Maximal Floquet exponent λ of the stabilized period-1 orbit in figure (a) and the period-3 orbit in figure (b) versus the gain K. The parameters for the system are $\beta_1 = 1$, $\beta_3 = 1$, $\mu = 0.02$, $a = 2.5$, and $\Omega = 1$.

The second example is taken from Tamaševičius et al. (2007) for which the period-1 UPO has an odd number of Floquet multipliers greater than unity. Tamasevicius introduced a clever method for adding an unstable mode by adding an additional state to the system (Tamaševičius et al., 2007). The updated state equations are given by

$$\dot{x} = y\,, \tag{5.25a}$$

$$\dot{y} = -\mu y + \beta_1 x - \beta_3 x^3 + a\cos(\Omega t) - KW + F(x, y, t)\,, \tag{5.25b}$$

$$\dot{W} = \lambda_c W - bF(x, y, t)\,, \tag{5.25c}$$

where W is the added state, b is an additional control gain, and λ_c is the positive,

Table 5.1: Control parameters which stabilized the period-1 and period-3 UPOs in Example 1. Stable gains were taken from Fig. 5.1 and rounded to the nearest hundredth.

Period-1					
R	0.0	0.2	0.4	0.6	0.8
K	0.27-1.99	0.32-2.00	0.37-2.00	0.43-2.00	0.48-2.00
Period-3					
R	0.0	0.2	0.4	0.6	0.8
K				0.38-0.43	0.43-0.56

real FE due to the added state (Tamaševičius et al., 2007). The addition of an unstable Floquet exponent is one strategy to stabilize the UPO using EDFC. The control input $F(x, y, t)$ is given by

$$F(x, y, t) = K \left[(1 - R) \sum_{r=1}^{\infty} R^{r-1} x(t - r\tau) - x(t) \right], \tag{5.26}$$

where the control is influenced by the delays of state x. The implementation of the matrix $\mathbf{K}$ is given by

$$\mathbf{K} = \begin{bmatrix} 0 & 0 & 0 \\ K & 0 & 0 \\ -Kb & 0 & 0 \end{bmatrix}, \tag{5.27}$$

and the Jacobian $\mathbf{A}$ and the delay matrices $\mathbf{B}_r$ are given by

$$\mathbf{A} = \begin{bmatrix} 0 & 1 & 0 \\ \beta_1 - 3\beta_3 x_0^2(t) & -\mu & -K \\ 0 & 0 & \lambda_c \end{bmatrix} - \mathbf{K}, \tag{5.28a}$$

$$\mathbf{B}_r = \mathbf{K} \begin{bmatrix} R^{r-1}(1 - R) & 0 & 0 \\ 0 & R^{r-1}(1 - R) & 0 \\ 0 & 0 & R^{r-1}(1 - R) \end{bmatrix}. \tag{5.28b}$$

Note that in this case of multiple gains and cross-coupling, the delay matrix $\mathbf{B}_r$ is created by premultipling the delay states with the matrix $\mathbf{K}$. Also note that in this

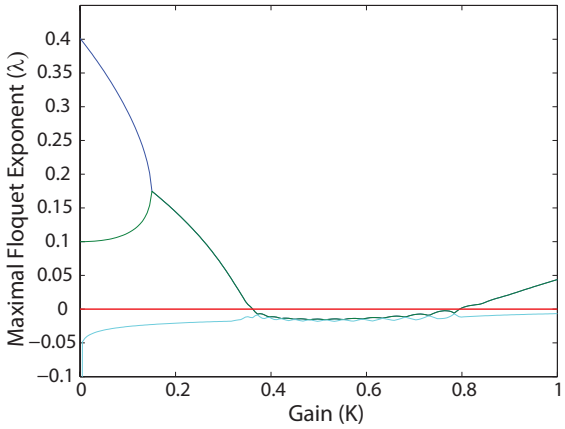

FIGURE 5.2: Example 2: Maximal Floquet exponent λ of the stabilized Period-1 orbit of the Duffing oscillator versus the gain K. The parameters for the system are $\beta_1 = 0.3$, $\beta_3 = 0.3$, $\mu = 0.3$, $a = 0.27$, $\Omega = 1$, $\lambda_c = 0.1$, $b = 0.2$, and $R = 0.9$.

example the gain K is used both as a coupling parameter in the Jacobian $\mathbf{A}$ and as a gain in the delay matrix $\mathbf{B}_r$. In Fig. 5.2 the three largest Floquet exponents are plotted versus the gain K with $R = 0.9$ for a period-1 UPO. A total number of 30 nodes were used in the spectral approach analysis. In this case the period-1 UPO is elliptical and is not shown. There is excellent agreement between the spectral element approach and the averaged UPO approach used by Tamaševičius et al. (2007).

The third and last example was selected to demonstrate the capability of the spectral approach to find the FEs of a UPOs for which previous methods are not fully capable of analyzing. For instance, the UPO in this example occurs in chaos arising from tori doubling which occurs after a Hopf bifurcation. Since a Hopf bifurcation does not tend to occur in a simple Duffing system (Kozlowski et al., 1995), a system with two identical, coupled Duffing oscillators studied by Kenfack (2003) was selected which also makes it a higher order system. The UPO, as shown in Fig. 5.3, is also non-symmetrical.

The equations for the identical coupled oscillators have the same form used in Eq. (5.22) with the first oscillator having the states x_1 and y_1 and the second oscillator

having the states x_2 and y_2. The only difference is a linear coupling element C between states x_1 and x_2. The implementation of the Jacobian $\mathbf{A}$ and the delay matrix $\mathbf{B}_r$ are given by

$$\mathbf{A} = \begin{bmatrix} 0 & 1 & 0 & 0 \\ \alpha_1 & -\mu - K & C & 0 \\ 0 & 0 & 0 & 1 \\ C & \alpha_2 & -\mu & 0 \end{bmatrix} \tag{5.29a}$$

$$\mathbf{B}_r = \begin{bmatrix} 0 & 0 & 0 & 0 \\ 0 & KR^{r-1}(1-R) & 0 & 0 \\ 0 & 0 & 0 & 0 \\ 0 & 0 & 0 & 0 \end{bmatrix}, \tag{5.29b}$$

where $\alpha_1 = \beta_1 - 3\beta_3 x_{10}^2(t) - C$, $\alpha_2 = \beta_1 - 3\beta_3 x_{20}^2(t) - C$, x_{10} is the path of the UPO for state x_1, and x_{20} is the path of the UPO for state x_2. Forcing and control are applied to the state y_1.

The stabilization of the period-1 UPO is show in Fig. 5.3 with the UPO for the states x_1 and y_1 plotted as an insert in the lower right corner. For this example the UPO was estimated from the system under EDFC. The maximal FE is plotted versus the gain K with $R = 0$, 0.2, 0.4, 0.6, and 0.8. A total number of 38 nodes were used in the spectral approach analysis. No changes to the spectral approach were required to accommodate the additional states or even the asymmetry. The control parameters that stabilized the period-1 UPO are listed in Table 5.2. The stable gains were taken from Fig. 5.3 and rounded to the nearest hundredth. A root locus plot of the case where $R = 0.6$ is given in Fig. 5.4.

In addition to the spectral approach, the Benettin method was used to analyze the case with $R = 0.6$. Results for gains stepped by 0.1 were plotted as stars in Fig 5.3. A total number of 200 to 400 delay states were required for the Benettin method to approach convergence at each gain, and the equations had to be integrated for at least 250 periods. Figure 5.3 shows good agreement between the spectral approach and the Benettin method.

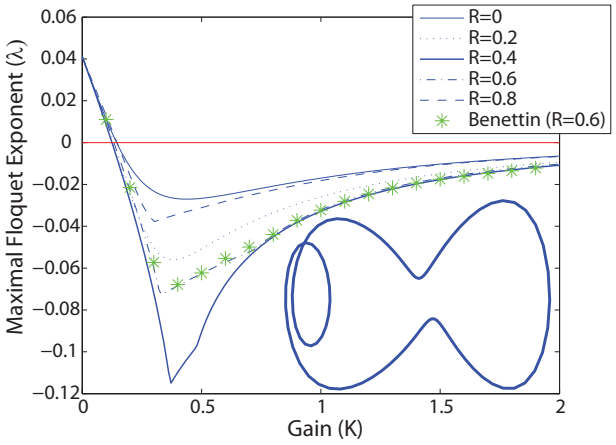

FIGURE 5.3: Example 3: Maximal Floquet exponent λ of the stabilized Period-1 orbit of the Coupled Duffing oscillators versus the gain K. The coupled oscillators have the identical parameters of $\beta_1 = 1$, $\beta_3 = 1$, $\mu = 0.1$, $C = 5$, $a = 15$, and $\Omega = 1.12$.

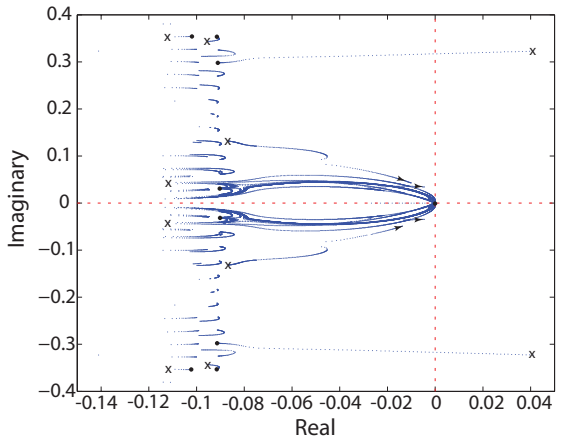

FIGURE 5.4: Example 3: Root Locus plot for the case $R = 0.6$. Crosses and black dots show the location of roots for $K = 0$ and $K \approx \infty$, respectively for a few FEs. The initially unstable FEs begin at $\Re(\lambda) = 0.0410$ and $\Im(\lambda) = \pm 0.323$.

Table 5.2: Control parameters which stabilized the period-1 UPO in Example 3. Stable gains were taken from Fig. 5.3 and rounded to the nearest hundredth.

R	0.0	0.2	0.4	0.6	0.8
K	0.15-2.00	0.13-2.00	0.13-2.00	0.14-2.00	0.15-2.00

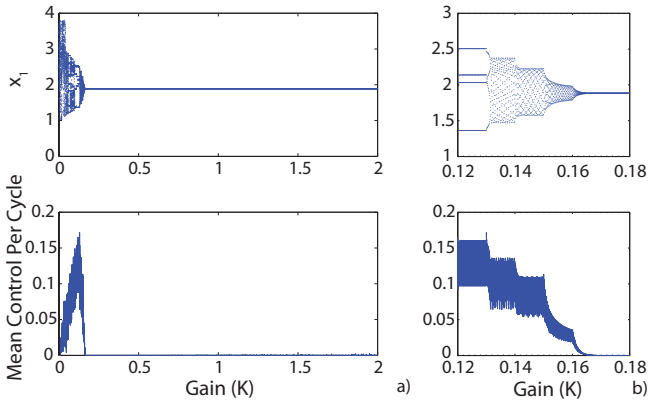

FIGURE 5.5: Example 3: Time response of the coupled Duffing oscillators versus the gain K for $R = 0.6$. Figure (a) shows the entire sweep of K from 0 to 2, while figure (b) shows the critical region between 0.12 and 0.18. The upper graphs show the response of the first oscillator sampled ten times per forcing period. The lower graphs show the absolute value of the control averaged over each period.

A simulation of the coupled Duffing system was performed with a value of $R = 0.6$. A sweep in gain K was performed from 0 to 2 and was stepped by 0.01 with 2000 units of simulation time at each step. The results in Fig. 5.5 show excellent agreement with the spectral approach. The spectral approach indicated a gain of about $K = 0.14$ was required for control. The simulation required a gain of $K = 0.151$ for control which was determined using a second, extended simulation with a single gain.

5.4 Conclusions

The spectral approach was introduced which is a new method to determine the FEs of UPOs stabilized by EDFC. The spectral approach approximates the infinite dimensional monodromy operator with a finite dimensional monodromy matrix. The

eigenvalues of the monodromy matrix are the Floquet multipliers from which the FEs can be determined. The advantage of the spectral approach is that DDEs can be solved directly without the complications that occur when the DDEs are simplified into ODEs. Unlike the existing analytical method used by Pyragas (2006), the spectral approach does not require any assumptions regarding the form of the FE and can be applied to highly nonlinear and high dimensional systems. The spectral approach also provides both the real and imaginary parts of the FE unlike the existing Benettin numerical method. Most importantly, the spectral element method can be used to analyze systems whose UPOs arise from bifurcations other than period-doubling.

The spectral approach was applied to Duffing system examples including UPOs stabilized by both DFC and EDFC. Also, an example of an UPO with an odd number of unstable FEs was stabilized after adding an unstable FE. The FEs calculated by the spectral approach were compared to results published using previously established methods. In both cases, the results of the spectral approach agreed well with the previously published results. Finally, the spectral element method was used to analyze a higher dimensional, asymmetrical system with a UPO in chaos arising from tori doubling. The resulting analysis agreed well with the numerical simulation.

6

Chaos Control with Arbitrary Delays

The typical approach for chaos control as introduced by Pyragas (1992) is implemented with a single delay. This delay is equal to the period of the unstable periodic orbit (UPO) of interest. For extended delayed feedback control (EDFC), an infinite number of delays are used, each of which are proportional to the UPO period (Pyragas, 1995). However, since the introduction of DFC, researchers have intentionally implemented arbitrary delays to control both UPOs (Nakajima and Ueda, 1998) and steady states via feedback control with multiple delays (MDFC) (Ahlborn and Parlitz, 2005). Physical limitations have also led to arbitrary delays being observed in experiments due to control loop latency (Sukow et al., 1997). The delays in each of these cases is arbitrary in the sense that the control delay is not equal to the period of the UPO, or in the case of the MDFC, there is no period. In this chapter, the spectral element method is applied to evaluate chaos control. The spectral approach is demonstrated to be a flexible method capable of analyzing multiple types of systems and control methods.

The method of half-period DFC was introduced by Nakajima and Ueda (1998)

as an effective method to control an UPO with an odd number of real characteristic multipliers greater than unity. The half-period method was introduced because it was assumed that such a system could not be controlled using DFC or EDFC (Nakajima and Ueda, 1998). While this assumption has since been disproved Just et al. (2007), such systems are still difficult to control without modifications, such as using a half-period delay. It is possible to analyze this system using the Benettin method (Pyragas, 1995), but the Benettin approach is not capable of determining the imaginary terms of the Floquet exponents (FEs).

Arbitrary delays in DFC due to control loop latency were investigated by Just et al. (1999a) using the exact method. These researchers also introduced a first order perturbation theory approximation for easier analysis (Just et al., 1999a). Hovel and Socolar (2003) extended both analysis methods to EDFC. The exact method is limited by the requirement of solving a time-dependent, transcendental eigenproblem. The assumptions required to solve such a problem tend to limit the effectiveness of the method to low-dimensional, chaotic systems resulting from period-doubling bifurcations (Pyragas, 2006). Finally, the MDFC method has been demonstrated to control steady states within a chaotic system. Ahlborn and Parlitz (2005) demonstrated a method of analyzing systems under MDFC using a damped Newton's algorithm.

This chapter is organized in the following way. The first section describes the method and notation for arbitrary delays when using the spectral element method to evaluate the delayed feedback control of chaos. Three different examples are then presented demonstrating how the spectral element method can be applied to half-period control, control loop latency, and MDFC. Finally, the conclusions are presented demonstrating the spectral approach does not have the limitations of the other analysis methods.

6.1 Spectral Element Method with Arbitrary Delay

In a previous paper, Tweten and Mann (2012b) demonstrated that the spectral element method can be applied to the EDFC method in cases where the delay is a multiple of the UPO period. Applying the spectral element method to arbitrary delays requires interpolation with additional notation. This section applies the methods developed by Khasawneh and Mann (2013) to determine the FEs of a system with multiple arbitrary delays.

As a reminder, the general delay differential equation (DDE) for a linearized or variational system with multiple delays is given by

$$\dot{\mathbf{x}}(t) = \mathbf{A}(t)\mathbf{x}(t) + \sum_{r=1}^{n_\tau} \mathbf{B}_r(t)\mathbf{x}(t-\tau_r), \tag{6.1}$$

where $\mathbf{x}(t)$ is a column vector of d states, $\mathbf{A}(t)$ is the $d \times d$ Jacobian, τ_r is the duration of the r^{th} delay, the delay matrices $\mathbf{B}_r(t)$ are the dependencies of the states on the delayed states $\mathbf{x}(t-\tau_r)$, and n_τ is the number of delays. In general, the Jacobian $\mathbf{A}(t)$ will be a function of the UPO of interest which makes the DDE non-autonomous. In the case of MDFC, the steady state condition does not vary so the DDE is autonomous. The non-autonomous Jacobian and delay matrices are periodic so that $\mathbf{A}(t) = \mathbf{A}(t+T)$ and $\mathbf{B}_r(t) = \mathbf{B}_r(t+T)$, where T is the period of the UPO.

The spectral element method estimates the FE of the system by constructing a Monodromy matrix which maps delay states to the current states. However, it is more convenient to start with the following map

$$\mathbf{H}\mathbf{x}_m = \mathbf{G}\mathbf{x}_{m-1}\,, \tag{6.2}$$

where the delay states $\mathbf{x}_{m-1}$ are mapped to the current states $\mathbf{x}_m$ using the matrices $\mathbf{H}$ and $\mathbf{G}$. The $\mathbf{H}$ matrix is constructed of terms associated with the current states, and the $\mathbf{G}$ matrix is constructed of terms associated with the delay states.

In the case of arbitrary delays, the delay time will not line up with the nodes on the standard grid. Instead, the delay can be considered to align with a second grid with an arbitrary offset from the standard grid. In the following equations, an element in the offset grid will be identified by the notation j^* while an element on the standard grid will be identified with j. The method of weighted residuals can then be modified to include the offset grid as follows

$$\int_0^1 \left(\frac{1}{t_j} \mathbf{x}_{j,i}\, \phi_i'(\eta) - \mathbf{A}(t_\eta)\mathbf{x}_{j,i}\, \phi_i(\eta) - \sum_{r=1}^{n_\tau} \mathbf{B}_r(t_\eta^*)\mathbf{x}_{j^*,i}\, \phi_i(\eta) \right) \psi_p(\eta)\, \mathrm{d}\eta = 0, \tag{6.3}$$

where $\psi_p(\eta)$ is the p^{th} Legendre polynomial, i is the i^{th} node on the Legendre-Gauss-Lobatto (LGL) grid, η is the normalized time in the standard elements, η^* is the normalized time in the offset elements, $t_\eta = (\eta + j - 1)t_j$, and $t_\eta^* = t_\eta - \tau_r$. The trial functions have the same form as Eq. (6.7) and the useful property

$$\phi_i(t_k) = \delta_{i,k}\,,\ t_k \in \{t_i\}_{i=1}^{n+1}\,, \tag{6.4}$$

their derivatives are given by

$$\phi_i'(t_k) = \begin{cases} \frac{\rho_i/\rho_k}{t_i - t_k}, & i \neq k \\ \sum\limits_{i=0, i\neq k}^{n+1} \frac{-\rho_i/\rho_k}{t_i - t_k}, & i = k\,, \end{cases} \tag{6.5}$$

and the barycentric weights (Higham, 2004) given by

$$\rho_i = \frac{1}{\prod\limits_{j=1, j\neq i}^{n+1} (t_i - t_j)},\ j = 1, 2, \ldots, n+1\,. \tag{6.6}$$

It is not practical to implement Eq. (6.3) with an offset grid. Instead, the offset elements must be interpolated onto the standard elements (Khasawneh and Mann,

2013). The interpolation results in each offset element being distributed across two standard elements. The interpolation is achieved using the barycentric Lagrange formula (Khasawneh and Mann, 2013)

$$\Gamma_i(\eta_k) = \frac{\frac{\rho_i}{\eta_k - \eta_i}}{\sum_{j=1}^{n+1} \frac{\rho_j}{\eta_k - \eta_j}}\,, \tag{6.7}$$

where η_i and η_j represent the time at the i^{th} and j^{th} nodes, respectively. In Eq. (6.7) the i^{th} nodes are on the standard grid and the k^{th} nodes are on the offset grid.

For the following implementation, the standard grid is assumed to begin with the element containing the largest delay as $j = 1$. Elements in the delay matrix $\mathbf{G}$ are numbered $j = 1$ to $j = N_t$, and elements in the current matrix $\mathbf{H}$ are numbered $j = N_t + 1$ to $j = N_t + E$, where E is the number of elements in a period. The term N_t is given by

$$N_t = \left\lceil \frac{\tau_{n_\tau}}{T} \right\rceil, \tag{6.8}$$

where $\lceil \cdot \rceil$ is the ceiling function, and τ_{n_τ} is the duration of the longest delay. The first element of an interpolated delay term is given by

$$q = \left\lfloor \frac{N_t T - \tau_r}{t_j} \right\rfloor + j - N_t E\,, \tag{6.9}$$

where $\lfloor \cdot \rfloor$ is the floor function.

Each element in the $\mathbf{H}$ matrix is composed of the current terms in Eq. (6.3). These elements in the $\mathbf{H}$ are defined by the submatrix

$$\mathbf{N}^p_{j,i} = \sum_{k=1}^{n+1} \left(\frac{1}{t_j} \mathbf{I} \phi_i'(\eta_k) \psi_p(\eta_k) w_k \right) - \mathbf{A}(t_\eta) \psi_p(\eta_i) w_i\,, \tag{6.10}$$

where $\mathbf{I}$ is the $d \times d$ identity matrix (Khasawneh and Mann, 2011b). The indexes i and k refer to the i^{th} and k^{th} nodes, respectively on the j^{th} element. The LGL

quadrature weights are given by

$$w_k = \begin{cases} \frac{2}{n(n+1)} & k = 1, n+1 \\ \frac{2}{n(n+1)(L_n(\eta_k))^2}, & \text{otherwise}\,. \end{cases} \tag{6.11}$$

The delay submatrices $\mathbf{P}' = [\mathbf{P}_q\ \mathbf{P}_{q+1}]$ cover two elements on the standard grid in the $\mathbf{G}$ matrix and are defined by

$$\mathbf{P}^p_{q,i} = \sum_{r=1}^{n_\tau} \sum_{k=1}^{n'} \mathbf{B}_r(t^*_\eta)\psi_p(\eta_k) w_k \Gamma_i(\eta_k + \delta)\,, \tag{6.12a}$$

$$\mathbf{P}^p_{q+1,i} = \sum_{r=1}^{n_\tau} \sum_{k=n'}^{n+1-n'} \mathbf{B}_r(t^*_\eta)\psi_p(\eta_k) w_k \Gamma_i(\eta_k + \delta - 1)\,, \tag{6.12b}$$

where n' are the number of nodes on the offset grid that fall in element q, and the offset is given by

$$\delta = \left\lceil \frac{\tau_r}{t_j} \right\rceil - \frac{\tau_r}{t_j}\,. \tag{6.13}$$

Note that the summation over r in Eq. (6.12) indicates that multiple delays are additive in each element. If the element q or $q+1$ of the submatrix $\mathbf{P}'$ is within the $\mathbf{H}$ matrix, $\mathbf{P}$ is also additive in the $\mathbf{H}$ matrix.

A graphical representation of the $\mathbf{G}$ and $\mathbf{H}$ matrices are given in Fig. 6.1 for representative delays smaller and greater than the period. The gray rectangle represents the $\mathbf{G}$ matrix, the white square represents the $\mathbf{H}$ matrix, and the internal boxes represent the elements. The elements are populated with zeros except for those populated by the submatrices $\mathbf{N}$ and $\mathbf{P}'$ which are indicated by white squares and cross-hatched rectangles, respectively in the figure. Note that the $\mathbf{P}'$ submatrix covers two elements and may be contained within the $\mathbf{H}$ matrix. Also note that the $d \times d$ identity matrix in the upper left of the $\mathbf{H}$ matrix and the upper right of the $\mathbf{G}$ matrix are missing from Fig. 6.1 for clarity. A detailed representation of the $\mathbf{G}$ and

H matrices including the identity matrices implemented with a single element has been given previously (Tweten and Mann, 2012b).

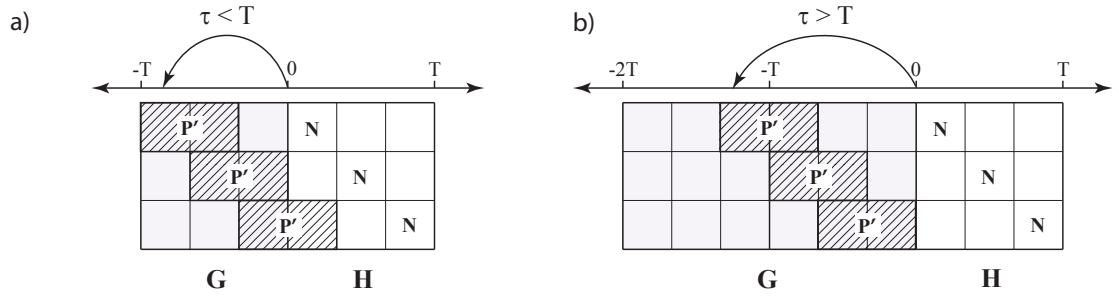

FIGURE 6.1: Graphical representation of the **G** and **H** matrices from Eq. (6.2) for a single delay of arbitrary duration and $E = 3$. The gray rectangle represents the **G** matrix, the white square represents the **H** matrix, and the internal boxes represent elements. Figure (a) shows the case where $\tau < T$, $N_t = 1$, and $q = 1$ for $j = 1$. Figure (b) shows the case where $\tau > T$, $N_t = 2$, and $q = 3$ for $j = 1$.

The final step is to construct the monodromy matrix **U** from Eq. (6.2). Using the matrices **G** and **H** and mapping identical states results in

$$\mathbf{U}(\mathbf{x}_0(t), t) = \begin{bmatrix} \mathbf{0}_{D_3 \times d \cdot E \cdot n} & \mathbf{I}_{D_3 \times D_3} & \mathbf{0}_{D_3 \times d} \\ & \mathbf{H}^{-1}\mathbf{G} & \end{bmatrix} \tag{6.14}$$

where $D_1 = d(1 + n \cdot E)$, $D_2 = d(N_t \cdot E \cdot n + 1)$, $D_3 = D_2 - D_1$, and the size of $\mathbf{H}^{-1}\mathbf{G}$ is $D_1 \times D_2$. The vector $\mathbf{x}_m$ includes states in the period $[0, T]$ and enough delay states to be of equal length as $\mathbf{x}_{m-1}$. The added delay states in $\mathbf{x}_m$ are required to make the monodromy matrix square. The additional states are mapped directly to the identical states in $\mathbf{x}_{m-1}$ through the identity matrix $\mathbf{I}_{D_3 \times D_3}$. The eigenvalues of the monodromy matrix are the Floquet multipliers μ of the system under control which relate to the FEs λ by $\mu = \exp(\lambda T)$.

6.2 Examples

The first example is a Lorenz system used by Nakajima and Ueda (1998) to demonstrate the capability of DFC to stabilize orbits with a half period delay. The equations

are given by

$$\dot{x} = -\sigma(x - y) - K[x(t - T/2) + x], \tag{6.15a}$$

$$\dot{y} = rx - y - xz, \tag{6.15b}$$

$$\dot{z} = xy - bz, \tag{6.15c}$$

where $\sigma = 10$, $r = 28$, $b = 8/3$, and the stabilized period-1 UPO has a period of $T \approx 1.559$ (Nakajima and Ueda, 1998). The matrices $\mathbf{A}$ and $\mathbf{B}$ are calculated by the same method used for the case $\tau = T$ as shown previously (Tweten and Mann, 2012b). For the case of a half period delay, one may either choose to use an odd number of elements requiring an arbitrary grid or an even number of elements in which the grid of the current elements align with the grid of the delay elements. The latter option was chosen with $E = 2$, $R = 0$, and $n = 20$.

Figure 6.2 shows the maximal nonzero Floquet exponent verses the gain K and shows the root locus plot for a range of K between 0 and 1000. Figure 6.2 (a) is nearly identical to the figure given by Nakajima and Ueda (1998). In Fig. 6.2 (b) the poles, denoted by the X, at 0 and 1 approach each other, combine at K $\approx$ 4 near 0, and then circle back to the negative half of the plane via complex ellipses. Once the poles return to the real axis on the negative half of the complex plane, one pole approaches zero and the other grows smaller remaining on the real axis. As K increases, the rest of the poles shown approach $0 + 0j$, indicated by the circle. It should be noted that while the Benettin method is fully capable of generating the analysis shown in Fig. 6.2 (a), the method is not capable of generating a root locus plot. This limitation occurs since the Benettin method is only capable of determining the real part of the FEs.

The second example shows how the spectral element method can be used to evaluate systems with control loop latency. The equations for the Toda oscillator

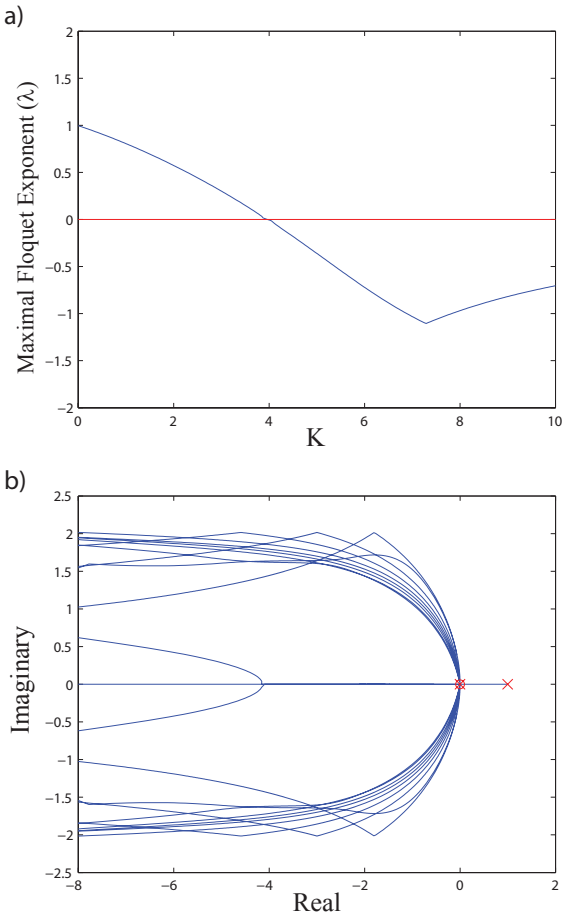

FIGURE 6.2: Example 1: Maximal nonzero Floquet exponent λ of the stabilized orbit $T \approx 1.559$ in figure (a) and the root locus in figure (b). In Fig. (b) the X represent the poles for $K = 0$ and the circle shows the location the poles approach at $K = 1000$.

studied by Just et al. (1999a) are given by

$$\dot{x} = y\,, \tag{6.16a}$$

$$\dot{y} = -\mu y - \alpha[\exp(x) - 1] + A\sin(2\pi t) + F(y - \delta)\,, \tag{6.16b}$$

$$F(y) = K\left[(1-R)\sum_{r=1}^{\infty} R^{r-1} y(t - rT) - y(t)\right], \tag{6.16c}$$

where $\mu = 0.8$, $\alpha = 25$, $A = 105$, and δ is the control loop latency. The stabilized period-1 UPO has a period of $T = 1$. Figure 6.3 shows the stability of the system with $R = 0$ for various K and δ. The solid, dash, and dash-dot curves in Fig. 6.3 (a) show

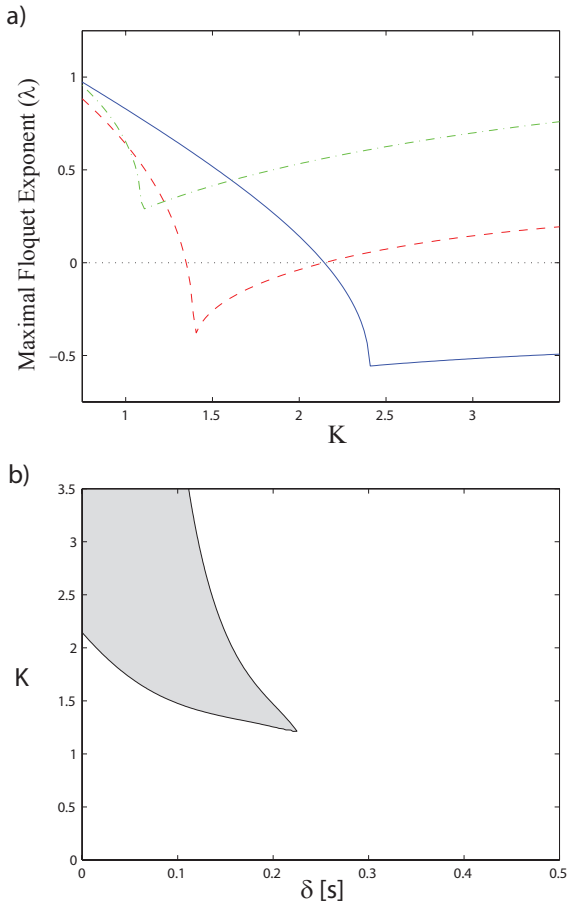

FIGURE 6.3: Example 2: Stability results of the Toda oscillator with $R = 0$. The solid, dash, and dash-dot curves in Fig. (a) show the maximal FE for control loop latencies of 0, 0.15, and 0.3 seconds respectively. The shaded areas in Fig. (b) are the regions for which the UPO is stabilized.

the maximal FE for control loop latencies of 0, 0.15, and 0.3 seconds respectively. These results compare well to the results presented by Just et al. (1999a). The shaded areas in Fig. 6.3 (b) are the regions for which the UPO is stabilized for a range of K and δ. The number of nodes used for Fig 6.3 (a) is $n = 20$, and the number of nodes used for Fig 6.3 (b) is 25. Figure 6.3 (b) was constructed from a 200×200 grid of K and δ values.

The spectral element method can also be readily applied to a system with control loop latency and EDFC. Figure 6.4 shows how the stable region of the Toda oscillator

with control loop latency is expanded when R is increased from 0 to 0.9. The number of nodes for the figure is $n = 25$, the number of delays are 50, and the figure is composed of a grid of 200×200 K and δ values. The number of required delays was found by increasing the number of delays until the maximal FE no longer changed with more delays (Tweten and Mann, 2012b). To confirm the boundaries of the stability region, eight simulations were run with a continuously increasing K. The diamonds in Fig. 6.4 show the transition points in the simulation in which the UPO is stabilized.

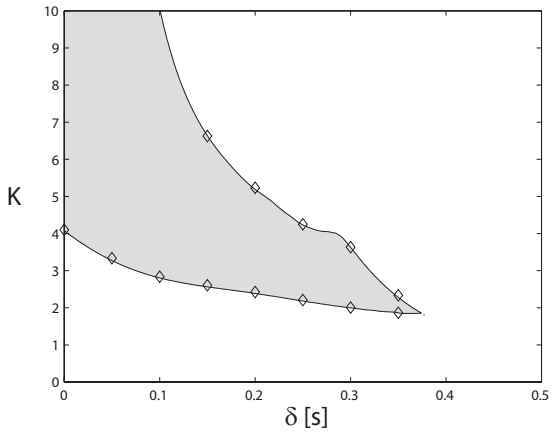

FIGURE 6.4: Example 2: Stability results of the Toda oscillator with $R = 0.9$. The shaded areas are regions in which the UPO is stabilized, and the diamonds are the transitions of stability determined using simulations.

The final example is the steady state control of a Rössler system using MDFC. In this case, only two delays are necessary to stabilize the fixed point. The equations are given by

$$\dot{x} = -y - z\,, \tag{6.17a}$$

$$\dot{y} = x + ay + k_1[y(t-\tau_1) - y] + k_2[y(t-\tau_2) - y]\,, \tag{6.17b}$$

$$\dot{z} = b + (x - c)z\,, \tag{6.17c}$$

where $a = 0.2$, $b = 0.2$, $c = 5.7$, and $k_1 = k_2 = 0.2$ (Ahlborn and Parlitz, 2005). Since there is no period associated with this system, one may be selected which

is convenient. Khasawneh and Mann (2013) recommend using the largest delay as the period, and that is the approach taken for this example. Figure 6.5 shows the stability diagram of the system for various durations of the delays τ_1 and τ_2. The shaded portion is the region in which unstable fixed point is stabilized. The figure agrees well with the results from Ahlborn and Parlitz (2005).

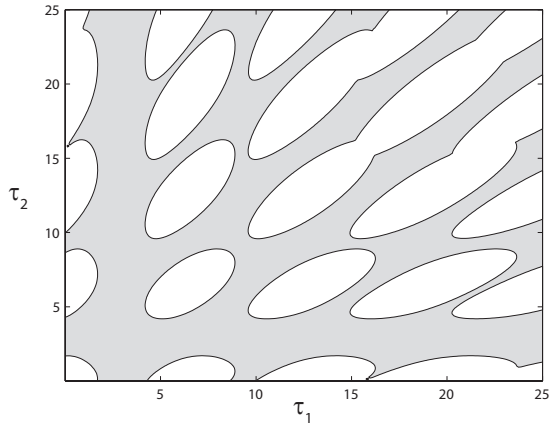

FIGURE 6.5: Example 3: Stability diagram of the fixed point (0,0) of the Rössler system. The shaded portions show the regions where the unstable fixed point is stabilized for various delays.

6.3 Conclusions

The technique of applying the spectral element method to the delayed feedback control of chaos with arbitrary delays was introduced along with the required notation. Arbitrary delays have a duration different than the period of UPO of interest or are any delays used to control steady states. The spectral approach approximates the infinite dimensional monodromy operator with a finite dimensional monodromy matrix. The eigenvalues of the monodromy matrix are the Floquet multipliers from which the FEs can be determined.

The spectral approach was applied to analyze a Lorenz system under half-period DFC and for the first time a root locus plot was created for the system. The Benettin

method can be used for analyzing the half-period control of the Lorenz system as well. However, the spectral approach has the advantage of calculating both the real and imaginary parts of the FE.

A Toda oscillator was analyzed under both DFC and EDFC with various control loop latencies. The DFC analysis using the spectral element method compared well with a previously published analysis, and the EDFC analysis compared well with numerical simulations. The exact method can be used to calculate the imaginary part of the FE, but is limited to systems in which assumptions regarding the initial magnitude of the imaginary part can be made (Pyragas, 2006). These assumptions tend to limit the effectiveness of the method to low-dimensional, chaotic systems resulting from period-doubling bifurcations (Pyragas, 2006). The spectral approach has no such limitations and therefore, has the potential to be applicable to a larger range of systems (Tweten and Mann, 2012b).

Finally, steady state control of a Rössler system via MDFC was analyzed using the spectral approach and compared well with previously published results using a damped Newton's algorithm. This last example demonstrates that the spectral approach is a good alternative to Newtons' algorithm for analyzing steady state control in chaotic systems. The spectral element approach is clearly a flexible method that can be applied to a large set of systems and control methods. The flexibility and advantages of the spectral approach have the potential to extend the delayed, feedback control of chaos to more complex systems.

7

Stochastic Resonance Methods

Stochastic resonance (SR) has come to describe systems in which output signals are enhanced rather than degraded by the presence of noise (McDonnell and Abbott, 2009). Phenomenon that fit under this broad definition include processes without a clearly identifiable signal. The classical concept of SR, however, refers to a system which has an increased sensitivity or amplification to a small signal at an optimal noise level (Gammaitoni et al., 1998; Anishchenko et al., 1999). This classical definition of SR is representative of nonlinear systems in which the signal synchronizes with system switching between equilibrium states (Gammaitoni et al., 1998). This chapter will focus exclusively on the classical definition of SR, and from this point forward, SR will be taken to mean classical stochastic resonance.

Stochastic resonance is a nonlinear phenomenon involving the rate of the escape of a system from potential wells. It is not surprising that techniques used to analyze and predict SR behavior tend to apply Kramers rate (Gammaitoni et al., 1998; Anishchenko et al., 1999). Kramers rate for a bi-stable system with parabolic potential

wells excited by white noise is given by

$$r_K = \frac{1}{2\pi}[\frac{|U''(0)|\,U''(x_m)}{c^2}]^{1/2}\exp\left(-\frac{\Delta U_0}{D}\right), \tag{7.1}$$

where $U(x)$ is the potential function, ΔU_0 is the barrier height, $x = x_m$ is the position of the potential minimum, $x = 0$ is the position of the barrier height, c is the damping coefficient, and D is the noise intensity (Anishchenko et al., 1999). If a system experiences thermal noise, the noise intensity can be modeled using the expression $D = k_B T$, where k_B is the Boltzmann constant and T is the absolute temperature (Hanggi et al., 1990). Kramers rate represents the mean escape rate for a system from an equilibrium without a signal present. Since SR requires a signal, Kramer rate by itself cannot fully describe this complex behavior.

SR occurs when the time-scale of the signal coincides with the time scale of the mean switching rate between equilibrium states (Gammaitoni et al., 1998). In nonlinear systems in which SR is possible, there are at least two time-scales. The global time is governed by the switching rate, that is the interwell behavior, and is therefore related to Kramers rate (Gammaitoni et al., 1998). The remainder of the time scales are associated with the local dynamics around each equilibrium state, that is the intrawell behavior. In order for SR to occur, there must be a clear separation between the global time scale and the local time scales (Gammaitoni et al., 1998). Finally, in SR behavior the forcing signal is not large enough to force the system between equilibrium positions, that is the forcing signal is weak (Anishchenko et al., 1999).

For an example of how the signal and global time-scales coincide in SR behavior, consider the commonly used example of the over-damped, non-dimensional, bistable

system with the equation of motion (EOM)

$$c\dot{x} + U'(x) = A\cos(\Omega t + \phi) + (2D)^{1/2}\xi(t)\,, \tag{7.2a}$$

$$U(x) = -\frac{1}{2}x^2 + \frac{1}{4}x^4\,, \tag{7.2b}$$

$$\langle \xi(t)\xi(0)\rangle = \delta(t)\,, \tag{7.2c}$$

where A is the signal amplitude, Ω is the signal frequency, ϕ is the signal phase, $\delta(t)$ is the Dirac delta function, and $\xi(t)$ is white Gaussian noise. For all examples in this chapter, the damping is $c = 1$. The Kramers rate for the EOM in Eq. (7.2), which can be found using (7.1), is $r_K = (1/\pi\sqrt{2})\exp(-1/4D)$. When the global time-scale and signal time-scale coincide, the following relationship is approximately true

$$T_n = (n - \frac{1}{2})T_\Omega \tag{7.3}$$

where T_n is the multiple of the first mean residence time in one well, n is the multiple, and T_Ω is the period of the signal (Gammaitoni et al., 1995). The residence time is the mean duration spent in a potential well. Figure 7.1 shows a physical explanation for Eq. (7.3) with the system represented as a highly damped ball moving in the bistable contour. To make the time-scale coincidence more clear, the potential function is often reformulated to include the forcing signal as $U(x) = -1/2x^2 + 1/4x^4 - A\cos(\Omega t + \phi)$ which is mathematically equivalent to treating the signal as an external forcing function. With this formulation, the potential varies with time. At time $t = 0$ the ball jumps from the right well to the left well. At T_1 seconds later, the potential is favorable for a jump to the right well as shown by case 1. If the global rate is about twice the signal rate, the system will tend to jump. When the ball does not jump, as in case 2, the potential is not favorable for a jump at $t = T_\Omega = 2T_1$ and tends to stay in the left well. Finally, the next opportunity for case 2 to jump with

a favorable potential occurs at $t = \frac{3}{2}T_\Omega$. Thus when the time-scales of Kramers rate and the signal coincide, the distribution of the residence times in the wells occur at the intervals $(n - 1/2)T_\Omega$.

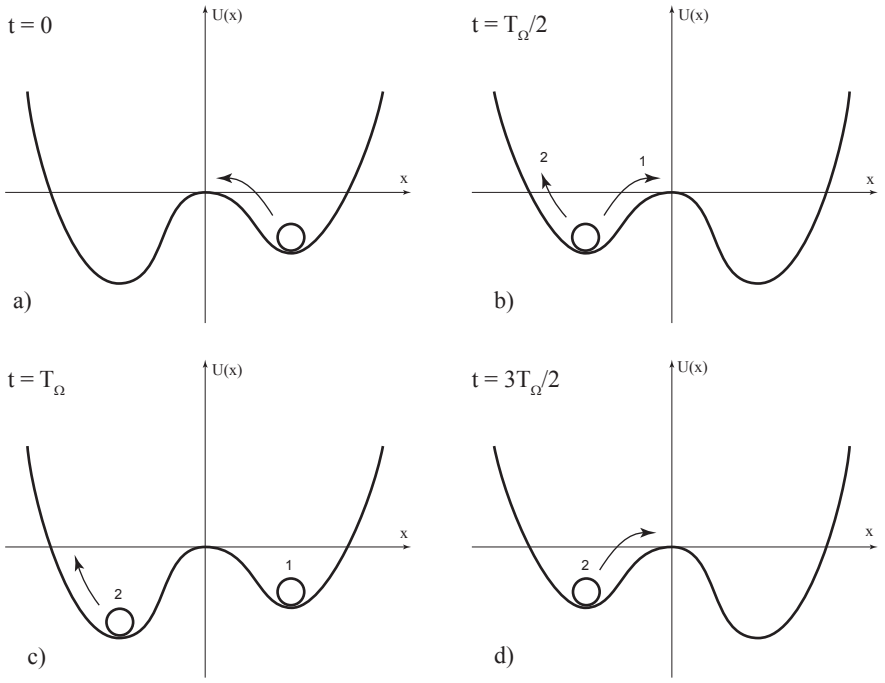

FIGURE 7.1: Coincidence of global and signal time-scales in an over-damped system with a SR response. Figure (a) shows the system immediately before jumping from the right to the left well. In figure (b) for time $t = T_\Omega/2$, conditions are favorable for a jump from the left to right well, but the system may stay in the left well. Figure (c) shows that if the system did not jump at time $t = T_\Omega/2$ the system tends to wait another forcing period before conditions become favorable again. Figure (d) shows the next favorable opportunity to change wells.

7.1 Analytical Models

The main focus of this chapter is to present numerical methods to analyze and simulate SR behavior. There are several analytical models that have been used extensively to analyze the system of Eq. (7.2). These models can provide useful insight into SR behavior and benchmarks with which to compare numerical methods.

This section briefly covers the two most commonly used models: two-state theory and linear response theory (LRT).

Two-state theory simplifies the SR behavior of a system as a discrete process modeling only the switching between equilibrium positions (Anishchenko et al., 1999). This theory requires the clear separation of the global and local time-scales in order to be accurate. Implicit in this assumption is that the local dynamics or relaxation processes are ignored since they are much faster than the switching rate (Anishchenko et al., 1999). The two-state theory also relies on the assumption of a weak signal $Ax_m << D$, where x_m is the equilibrium position which is included due to linearization (Gammaitoni et al., 1998).

Analytical solutions or numerical simulations using two-state theory are based on the so called "master equation"

$$\dot{n}_{\pm}(t) = -W_{\mp}(t)n_{\pm}(t) + W_{\pm}(t)n_{\mp}(t)\,, \tag{7.4}$$

where $n_{\pm}(t)$ are the probabilities that the system resides in either the right $+$ or left $-$ state and $W_{\pm}$ are the periodic probability densities of switching between states (Gammaitoni et al., 1998; Anishchenko et al., 1999). Solving Eq. (7.2) and (7.4) leads to closed form solutions for the spectral power amplification (SPA), signal to noise ratio (SNR), and phase lag between output and signal input. It should be noted that these solutions break down when the weak signal assumption no longer applies.

Linear response theory (LRT) attempts to overcome the limitations of two-state theory by including the local dynamics. The LRT is encapsulated in the estimation of the response function $\chi(t)$ which is related to the mean response $\langle x(t)\rangle$ of the system through

$$\langle x(t)\rangle = \langle x\rangle_{st} + \int_{-\infty}^{\infty} \chi(t-\tau, D) f(\tau)\,\mathrm{d}\tau\,, \tag{7.5}$$

where $f(t)$ is the forcing signal and $\langle x \rangle_{st}$ is the mean value of the unperturbed system (Anishchenko et al., 1999). The response function, $\chi(t)$, cannot be determined exactly and therefore approximations are used instead (Anishchenko et al., 1999). The power spectral density $G_{xx}(\omega)$ of the response determined by LRT is

$$G_{xx}(\omega) = G_{xx}^{(0)}(\omega) + \frac{\pi}{2} A^2 \left|\chi(\Omega)\right|^2 \times (\delta(\omega - \Omega) + \delta(\omega + \Omega)) + \mathcal{O}(A^2) \tag{7.6}$$

where $\delta(\omega)$ is the Dirac delta function, the susceptibility $\chi(\omega)$ is the Fourier transform of the response function, and $G_{xx}^{(0)}$ is the unperturbed power spectral density (PSD) (Anishchenko et al., 1999). Equation (7.6) makes clear the assumption in LRT that the local and global dynamics are treated as additive. This is a reasonable assumption in many cases since the global and local times scales are clearly separated in most SR behavior. The susceptibility determined from LRT is given by Jung (1993) as

$$\chi(\omega, D) = \frac{1}{D}\left(\frac{g_1 \lambda_m^2}{\lambda_m^2 + \omega^2} + \frac{g_2 \alpha^2}{\alpha^2 + \omega^2}\right) - i\frac{\omega}{D}\left(\frac{g_1 \lambda_m}{\lambda_m^2 + \omega^2} + \frac{g_2 \alpha}{\alpha^2 + \omega^2}\right). \tag{7.7}$$

The remaining terms in in Eq. (7.7) are given by

$$g1 = \left\langle x^2 \right\rangle_{st} - g_2\,, \tag{7.8a}$$

$$g2 = \frac{\lambda_m \left\langle x^2 \right\rangle_{st}}{\lambda - \alpha} + \frac{\left\langle x^2 \right\rangle_{st} - \left\langle x^4 \right\rangle_{st}}{\lambda_m - \alpha}\,, \tag{7.8b}$$

$$\lambda_m = 2r_K\,, \tag{7.8c}$$

$$\alpha = \left|U''(x_m)\right|\,, \tag{7.8d}$$

where ω is the signal frequency (Anishchenko et al., 1999). The stationary values of the unperturbed system are given by

$$\left\langle x^n \right\rangle_{st} = \frac{\int_{-\infty}^{\infty} x^n \exp\left(\frac{U(x)}{D}\right) \mathrm{d}x}{\int_{-\infty}^{\infty} \exp\left(\frac{U(x)}{D}\right) \mathrm{d}x}\,, \tag{7.9}$$

where $U(x)$ is given in Eq. (7.2) (Anishchenko et al., 1999). Finally, in order to calculate the SNR, one must know the spectral density of the unperturbed system which Anishchenko et al. (1999) gives as

$$G_{xx}^{(0)}(\omega) = \frac{2g_1\lambda_m}{\lambda_m^2 + \omega^2} + \frac{2g_2\alpha}{\alpha^2 + \omega^2}\,. \tag{7.10}$$

7.2 Analysis Methods

The analysis methods used to evaluate the SR behavior of a system can be categorized as signal amplification or system organization techniques. Methods that evaluate the signal amplification include SPA which is the ratio of the magnitudes of the output power to the input power at the signal frequency and the SNR which compares the signal response to the noise response. Methods that evaluate the system organization include the residence time distribution (RTD) which is the normalized time the system spends in each well and the phase lag of the response to the signal. In addition, the RTD can be used to evaluate SR behavior as an actual resonance. Resonance in the case of SR is defined as an amplification of the forcing signal due to time-scale coincidence (Gammaitoni et al., 1995). The remainder of this section describes the numerical techniques used in section 7.3 to determine the SPA, SNR, RTD, and phase lag of the response. The analytical expressions used as a benchmark for these numerical methods are also presented in this section.

The SPA, which is ratio of output and input power, is given by

$$\eta = \frac{p_1}{p_A}\,, \tag{7.11}$$

where p_1 is the power of the output at the signal frequency and p_A is the power of the signal (Anishchenko et al., 1999). When using LRT, the expression for the SPA is given by $\eta = |\chi(\Omega)|^2$. For a simulation or experiment, the power must be calculated

numerically. The numerical method used for the examples in section 7.3 is given by

$$\eta = \frac{\langle |X(\Omega)| \rangle^2}{A^2}\,, \tag{7.12}$$

where X is the single-sided Fourier transform of the output and the angle brackets represent the average of multiple ensembles.

The SNR of the response is defined as

$$\mathrm{SNR} = \pi \frac{\lim\limits_{\Delta\omega \to 0} 2 \int\limits_{\Omega-\Delta\omega}^{\Omega+\Delta\omega} G_{xx}(\omega)\,\mathrm{d}\omega}{G_{xx}^{(0)}(\Omega)}\,, \tag{7.13}$$

where G_{xx} is the two-sided PSD of the response (Gammaitoni et al., 1998). When using LRT, the analytical expression is $\mathrm{SNR} = \pi A^2 \left|\chi(\Omega)\right|^2 / G_{xx}^{(0)}(\Omega)$. For simulations and experiments, the spectral density must be calculated numerically. A number of noise ensembles are typically used in simulations to determine the mean response. One numerical method for the mean PSD is given by

$$G_{xx}(\omega) = \int\limits_{-\infty}^{\infty} \mathrm{e}^{-i\omega\tau} \langle x(t+\tau)x(t) \rangle\,\mathrm{d}\tau\,, \tag{7.14}$$

where $x(t+\tau)x(t)$ represents the auto correlation of the output data, the brackets represent the average of all the noise ensembles, and the integral with $\mathrm{e}^{-\imath\omega\tau}$ is the Fourier transform (Gammaitoni et al., 1998). The numerical method used for the examples in section 7.3 is given by

$$\mathrm{SNR} = \pi \frac{\langle |X(\Omega)| \rangle^2}{G_{xx}^{(0)}}\,. \tag{7.15}$$

where X is the one-sided Fourier transform. In some cases the unperturbed PSD $G_{xx}^{(0)}$ fluctuated, so a least squares fit was used to find the value of the PSD at the

forcing signal. It should be noted that while the unperturbed PSD was used in the denominator in Eq. (7.15) to match LRT, it is also common to estimate the SNR from the perturbed PSD (McDonnell and Abbott, 2009) by averaging the PSD on either side of the response peak (Anishchenko et al., 2007).

The residence time is the duration the system remains in a single potential well. The expected amount of time spent in each well can be predicted using a probability distribution referred to as the residence time distribution. Several analytical expressions for the RTD are available in the literature including a rather complicated expression from Zhou et al. (1990) and a fairly simple equation highlighted by Gammaitoni et al. (1998). The examples in section 7.3 use both expressions, but since both result in nearly identical predictions, only the equation presented by Gammaitoni et al. (1998) will be given here. The RTD, given by $N(T)$, can be predicted using

$$N(T) = N_0 \left[1 - \frac{1}{2} \left(\frac{A}{D} \right)^2 \cos(\Omega T) \right] r_K \mathrm{e}^{-r_K T} , \tag{7.16a}$$

$$N_0^{-1} = 1 - \frac{1}{2} \frac{\left(\frac{A x_m}{D} \right)^2}{\left[1 + \left(\frac{\Omega}{r_K} \right) \right]} , \tag{7.16b}$$

where the time T represents the period and $N(T)$ is normalized so that $\int_0^\infty N(T)\,\mathrm{d}T = 1$. The RTD can also be estimated from a time series by normalizing a histogram of the residence times. In order to estimate the RTD for the simulations in section 7.3, the data was first filtered using a two-state filter (i.e. data points for $x(t) > 0$ were given the value of $+x_m$, and data points for $x(t) < 0$ were given the value of $-x_m$). The residence times in both potential wells where saved and the results plotted in a histogram. The histogram was normalized so that $\sum_{n=1}^{N} N(T_n)/\Delta T = 1$, where N is the total number of data points in the histogram and ΔT is the bin size.

The phase lag ψ of the response can be calculated by LRT using the expression

$$\psi = -\arctan\frac{\Im\left[\chi(\Omega)\right]}{\Re\left[\chi(\Omega)\right]}\,, \tag{7.17}$$

given by Anishchenko et al. (1999). For simulations and experiments, the phase lag can be determined using the Fourier transform:

$$\psi = -\arctan\frac{\Im\left[\langle X(\Omega)\rangle\right]}{\Re\left[\langle X(\Omega)\rangle\right]}\,, \tag{7.18}$$

where X is the one-sided Fourier transform of the response. If the signal phase is $\phi \neq 0$, than the phase lag is calculated by $\phi + \psi$.

Finally, simulations which involve the integration of the EOM can cause a number of problems when adding noise. This is especially true of predictor-corrector solvers such as Matlab's ode45. Alternative processes that are deterministic to the solver but approximate a Gaussian process are a good compromise. One such process is the Bennett-Rice (BR) representation of Gaussian noise which was selected for the simulations in the next section. The Bennett-Rice approximation is given by

$$G_N(t) = \sum_{k=1}^{N} a_k \cos(k\delta\omega t + \phi_{0k})\,, \tag{7.19a}$$

$$a_k = \left[\frac{2\Psi_0(\omega_k)}{2\pi}\right]^{1/2}\,, \tag{7.19b}$$

where N is the number of harmonics, ω_{cut} is the maximum frequency of the process, $\Delta\omega = \omega_{cut}/N$, and ϕ_{0k} is uniformly distributed over $[0\ 2\pi]$ (Simiu, 2002). In the simulations below, the BR representation was used to approximate Gaussian white noise so $\Psi_0 = 2\pi/\omega_{cut}$ was used in all cases.

7.3 Simulations

In this section, the response of numerical simulations are compared with the response predicted from the LRT. Since the expressions for the LRT presented in Section 7.2

assume the system presented in Eq. (7.2), this system was also selected for the simulations. To approximate Gaussian white noise, the BR method in Eq. (7.19) was used with a cut-off frequency of $\omega_{cut} = 3$ rad/s and $N = 5000$ harmonics for all simulations. In addition, the responses of 225 different ensembles where used to estimate the mean response at each data point. More than one set of parameters was necessary to compare the signal amplification methods and the system organization methods. The comparisons for these two types of methods as well as the parameter chosen are presented in the next two subsections.

7.3.1 Signal Amplification

In this subsection, the amplitude of the signal is 0.1 in non-dimensional units. All other parameters are included in the figures. The PSD for simulations with and without a signal are compared with the unperturbed PSD predicted using LRT in Fig. 7.2. For low values of noise intensity, the unperturbed PSD of both the simulation and LRT tend to agree. However, as the noise intensity increases, the PSD calculated from the simulations and the theory tends to diverge. The difference may be caused by the fact that the simulations do not perfectly reflect true white Gaussian noise due to the cut-off frequencies.

The SPA calculated using LRT and simulations for two different signal frequencies ($\Omega = 0.1$ rad/s and $\Omega = 0.01$ rad/s) are presented in Fig. 7.3. The overall trend is the same for both theory and simulations. The agreement is better for the faster signal frequency, $\Omega = 0.1$. Since simulations using both signal frequencies were integrated for the same length of time, the better agreement for the faster signal frequency may indicate longer simulation times will improve the agreement for the lower frequency as well.

The SNR calculated using LRT and simulations for two different signal frequencies ($\Omega = 0.1$ rad/s and $\Omega = 0.01$ rad/s) are presented in Fig. 7.4. The overall trend for

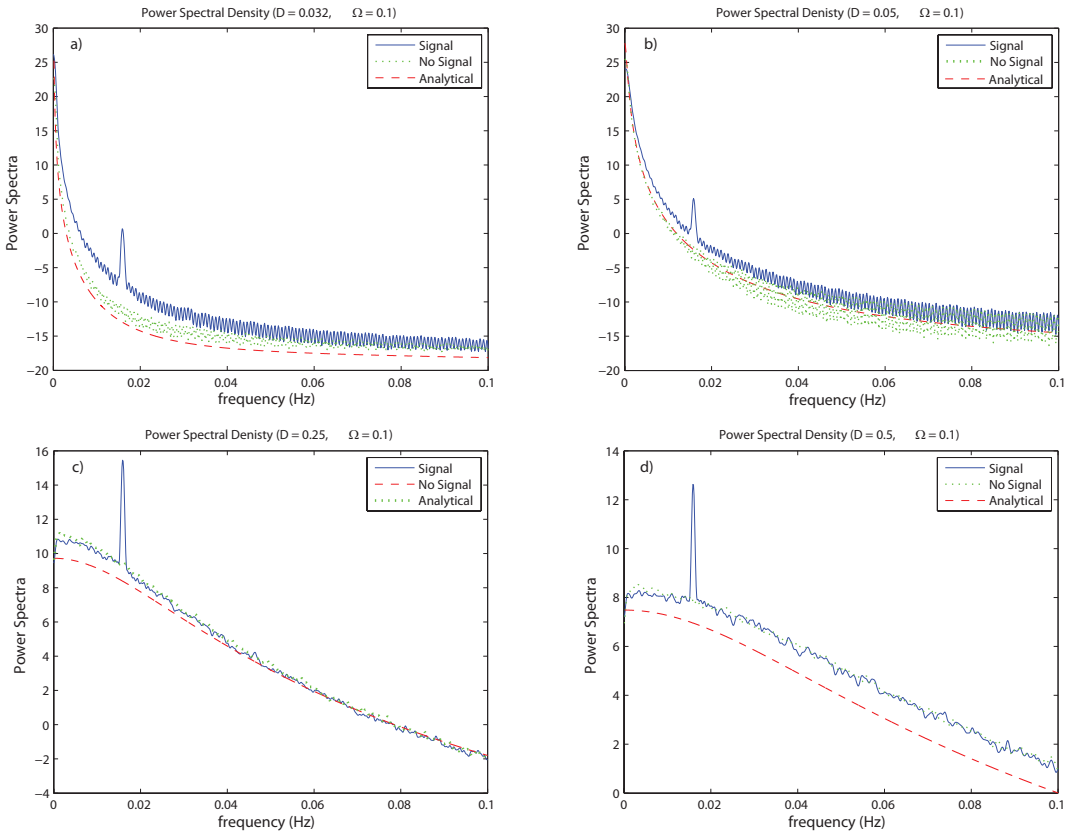

FIGURE 7.2: Comparison of the PSD for the system response simulated with a signal ($A = 0.1$ and $\Omega = 0.1$), simulated without a signal, and the analytical LRT prediction for no signal (plots show $10 \times \log_{10}(G_{xx}(\omega))$). Figure (a) shows the comparison for $D = 0.032$, Fig. (b) for $D = 0.05$, Fig. (c) for $D = 0.25$, and Fig. (d) for $D = 0.5$.

the theory and simulations is quite similar except at the transition between low and high noise intensities, which occurs at $D = 0.032$ for $\Omega = 0.01$ and $D = 0.05$ for $\Omega = 0.1$. At low noise intensities, the dominant dynamics are mainly local, and at high noise intensities, the dominant dynamics are mainly global. Since LRT assumes the local and global dynamics are additive, it may be that the theory breaks down at the transition.

7.3.2 System Organization Examples

In this subsection, amplitudes of both 0.1 and 0.2 in non-dimensional units were used in the simulations. All parameters are included in the figures. Figure 7.5 provides

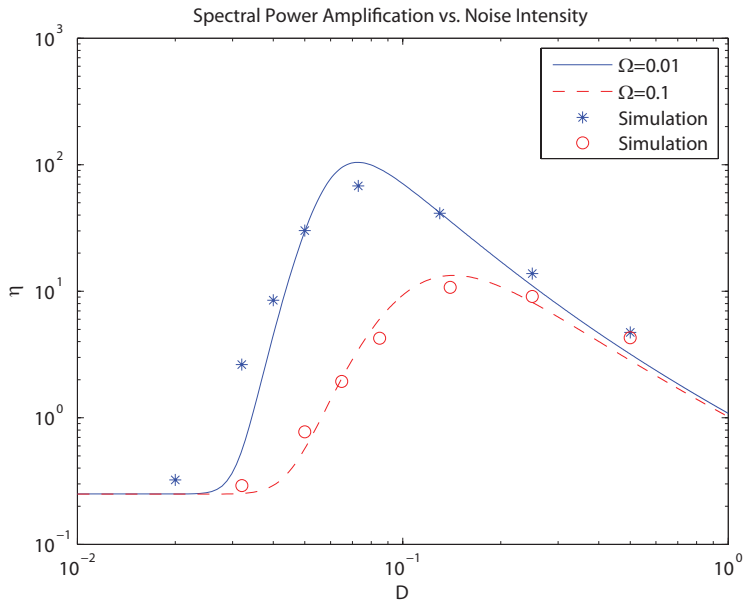

FIGURE 7.3: A comparison of the SPA using the LRT and simulations. Plotted is the SPA calculated using LRT with $\Omega = 0.01$ (solid line) and $\Omega = 0.1$ (dashed line) and the SPA calculated from simulations with $\Omega = 0.01$ (stars) and $\Omega = 0.1$ (circles).

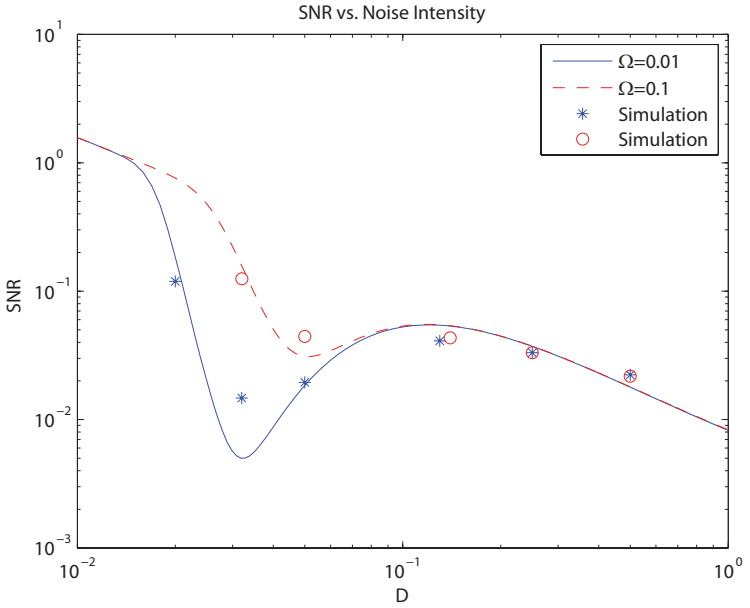

FIGURE 7.4: A comparison of the SNR using LRT and simulations. Plotted is the SNR calculated using LRT with $\Omega = 0.01$ (solid line) and $\Omega = 0.1$ (dashed line) and the SNR calculated from simulations with $\Omega = 0.01$ (stars) and $\Omega = 0.1$ (circles).

a comparison between the RTD using the analytical method of Zhou et al. (1990) and numerical simulations for a signal frequency of $\Omega = 0.0319$ rad/s. The figure highlights how the RTD changes as the noise intensity increases. Figure 7.5a shows the RTD for the system with a noise intensity below the SPA peak. Figures 7.5b and 7.5c show the distributions as the noise intensity increases. The RTD in Fig. 7.5c is for a noise intensity nearly at the peak SPA which corresponds to a coincidence of global and signal time-scales. Fig. 7.5d shows the RTD for a noise intensity well above the SPA peak, and the resulting near exponential distribution is similar to a system with no signal present.

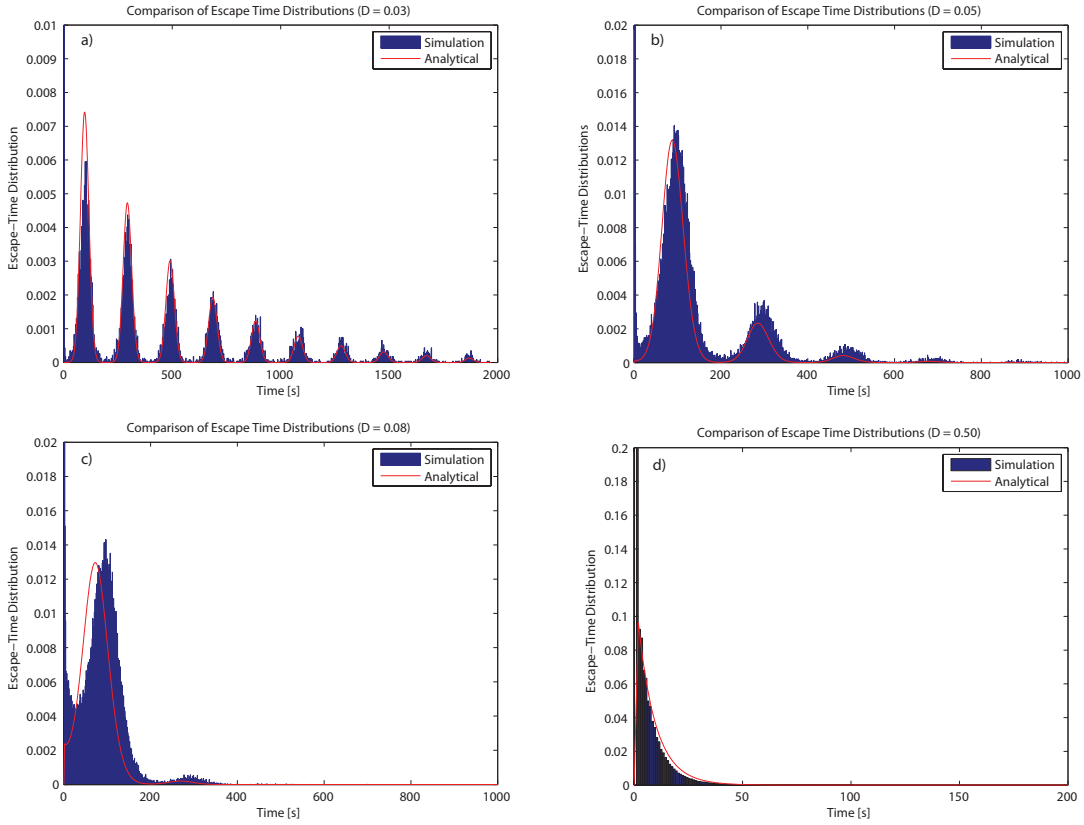

FIGURE 7.5: Comparison of the of the residence time distributions for simulations and the analytical method presented by Zhou et al. (1990) for $A = 0.2$ and $\Omega = 0.0319$ rad/s. Figure (a) shows the comparison for $D = 0.03$, Fig. (b) for $D = 0.05$, Fig. (c) for $D = 0.08$, and Fig. (d) for $D = 0.5$.

Time histories of the response corresponding to the RTDs in Fig. 7.5 are presented in Fig. 7.6. Each graph in Fig. 7.6 shows the response of the system, the forcing signal in arbitrary units, and a sinusoid representing the phase of the system response at the signal frequency in arbitrary units. Figure 7.6a shows little switching between equilibrium positions which corresponds to RTD peaks with low amplitudes. Figures 7.6b and 7.6c show more switching events as expected based on the coincidence of global and signal time-scales. Finally in Fig. 7.6d, the switching occurs at a much faster rate than the signal which results in little influence on the system from the signal.

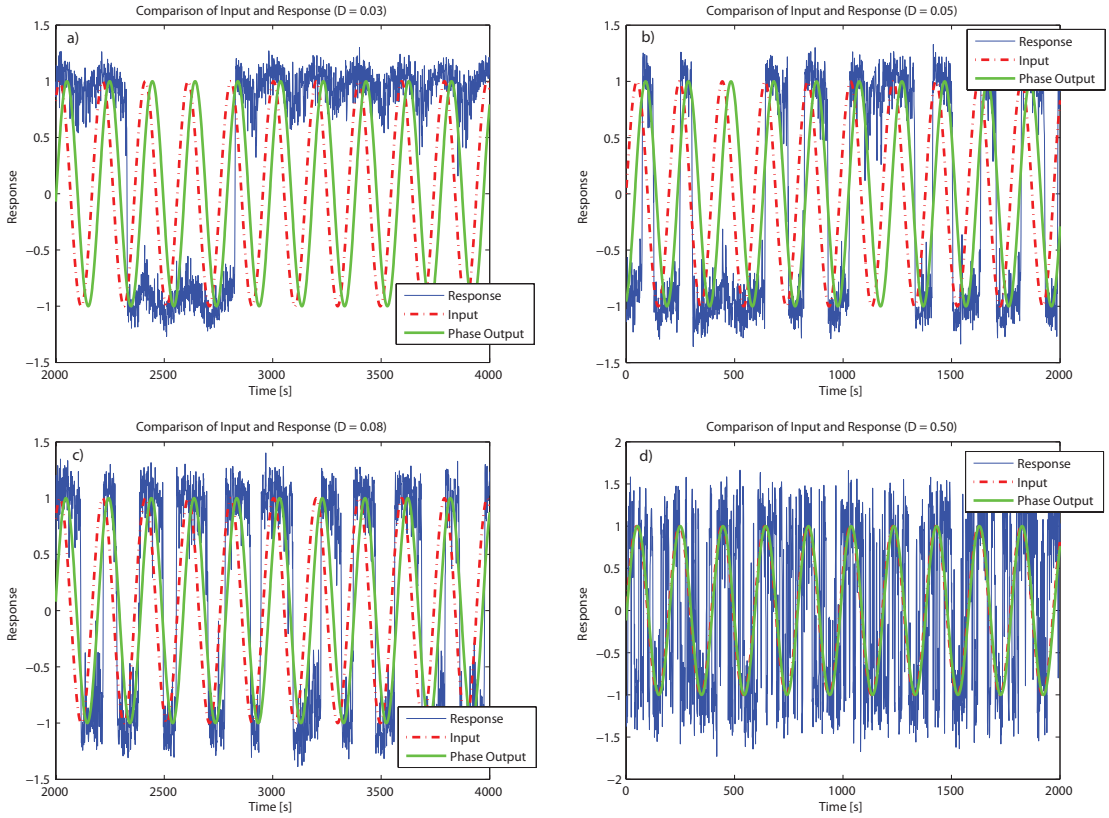

FIGURE 7.6: Time history plots of the simulations for $A = 0.2$ and $\Omega = 0.0319$ rad/s. The plots compare the response of the system, the forcing signal in arbitrary units, and a sinusoid representing the phase of the system response at the signal frequency in arbitrary units. Figure (a) shows the comparison for $D = 0.03$, Fig. (b) for $D = 0.05$, Fig. (c) for $D = 0.08$, and Fig. (d) for $D = 0.5$.

The phase relationship between the forcing signal and the response at the signal frequency is given in Fig. 7.7 for LRT, two-phase theory, and simulations for $A = 0.2$ and $\Omega = 0.0319$ rad/s. For large noise intensities, all three methods agree well. However, for low noise intensities, the phase lag calculated using LRT, two-phase theory, and simulations diverge. The LRT method models the system response as linear within the wells but does not agree well with the simulations at low noise intensities. However, if the simulation results are processed using a two-state filter, the phase lag is remarkably similar to the phase lag predicted by the two-state theory. It appears that this discrepancy may be due to limitations in the LRT. This conclusion arises from the fact that the phase lag of the simulation data agrees well with two-state theory after a two-state filter is applied to the simulation data.

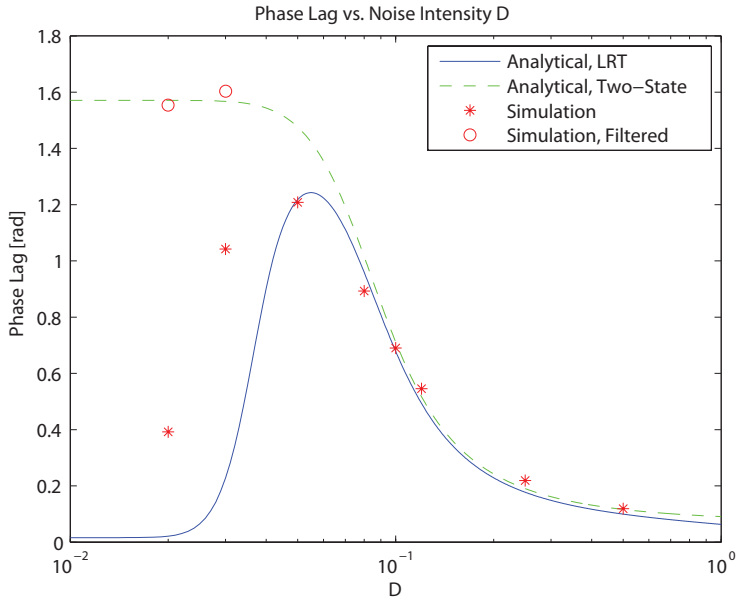

FIGURE 7.7: The phase lag between the forcing signal and the system response calculated using LRT (solid line), two-state theory (dashed line), and simulations for $A = 0.2$ and $\Omega = 0.0319$ rad/s. The simulation results are presented both for unfiltered data (stars) and after applying a two-state filter (circles).

Finally, a resonant relationship between the forcing signal and the response has been established by considering the strength of the RTD peaks while holding the

noise intensity constant and varying the forcing signal frequency (Gammaitoni et al., 1995). The strength of each peak P_n is determined using

$$P_n = \int_{T_n-\alpha T_\Omega}^{T_n+\alpha T_\Omega} N(T)\,\mathrm{d}T\,, \tag{7.20}$$

where n is the multiple of the first peak of the RTD and $\alpha = 1/4$ (Gammaitoni et al., 1995). The strength of the first multiple P_1 calculated using Eq. (7.16), the analytical method presented by Zhou et al. (1990), and the results of the simulations are presented in Fig. 7.8. The parameters used in all three methods are $A = 0.1$ and $D = 0.14$. The analytical method given by Zhou et al. (1990) produces nearly identical results to those calculated using Eq. (7.16) highlighted by Gammaitoni et al. (1998). Since Eq. (7.16) is much simpler, Eq. (7.16) is the preferable method. The amplitude of the peak determined from the simulations is slightly lower than the peaks predicted by the analytical methods, but clearly the same trend is demonstrated by all three methods. It may be that the peak calculated using the simulations will approach the analytical expressions if the simulation length is long enough or perhaps the analytical methods over-predict the peaks. For the simulation at the resonance peak ($\Omega = 0.1$ rad/s), a total number of about 43,000 residence times were used to calculate P_1. Unfortunately, each simulation took nearly an hour to complete, so significantly increasing the number of residence times would be time prohibitive.

7.4 Conclusions

In this chapter a number of well established numerical models and analysis methods were presented. The numerical methods were applied to simulated data and then compared to equivalent calculations for analytical results; this was done to demonstrate the effectiveness and accuracy of the numerical methods. The trends in both

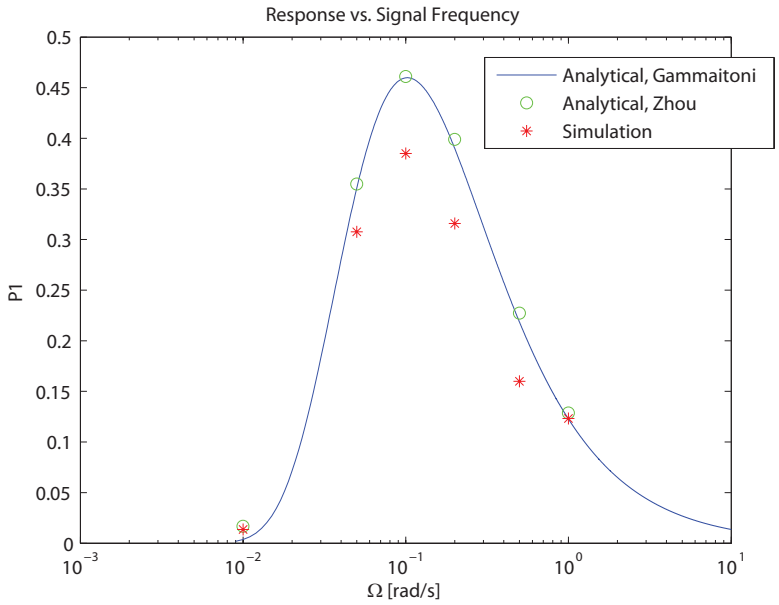

FIGURE 7.8: Strength of the first RTD peak versus signal frequency using Eq. (7.16), the analytical method presented by Zhou et al. (1990), and simulations. The system parameters are $A = 0.1$ and $D = 0.14$.

the analytical methods and the simulated data agreed well in all cases.

The first technique for analyzing SR behavior is SPA which is the ratio of the output power and signal power at the signal frequency. Comparisons between theory and simulations for the SPA in Fig. 7.3 show good agreement for nearly all cases. The second technique presented is SNR which is the ratio of the output power over the PSD at the signal frequency multiplied by π shown in Fig. 7.4. The SNR from the theory and simulations agree well except in the cases at the transition between low and high noise intensities. At low noise intensities the dominant dynamics are local, and at high noise intensity the dominant dynamics are global. Since LRT assumes the local and global dynamics are additive, it appears that in this case the theory breaks down at the transition.

The third technique utilizes the RTD which is the normalized distribution of the time spent in a single well. There was excellent agreement between theory and the

simulations as shown in Fig. 7.5. The fourth technique presented is the phase lag between the forcing signal and the system response at the signal frequency as shown in Fig. 7.7. For large noise intensities there is excellent agreement between theory and simulations. However, at low noise intensities, there is a disagreement between LRT and the simulations although the overall trend agrees well. It appears that this discrepancy may be due to limitations in the LRT. This conclusion arises from the fact that the phase lag of the simulation data agrees well with two-state theory after a two-state filter is applied to the simulation data.

Finally, the fact that stochastic resonance can be viewed as a true resonance is highlighted. Resonance in this case is defined as the amplification of a forcing input due to coincidence of two time-scales. The strength of the first RTD peak is plotted versus signal frequency in Fig. 7.8. The typical resonant response of an increasing amplitude for frequencies up to a resonant frequency and then a decreasing amplitude at frequencies larger than the resonant frequency is demonstrated. The trend of both the theory and simulations agree well. However, the theory predicts a larger amplitude response near the peak response. It may be that the peak calculated using the simulations will approach the analytical expressions if the simulation length is long enough or perhaps the analytical methods over-predict the peaks.

8

Stochastic Resonance in a Bi-Stable Beam

There is a great deal of stochastic resonance (SR) literature that presents analytical work for overdamped systems. In fact, comprehensive and informative papers (Anishchenko et al., 1999; Gammaitoni et al., 1998; Jung, 1993) and books (Andó and Graziani, 2000; Anishchenko et al., 2007) are readily available. However, underdamped systems, while also discussed in some of these references, have received much less attention. A few examples of works addressing analytical methods for underdamped systmes include the Kramers (1940) approach for the escape rates, which has been available for some time. Another underdamped method, introduced by Simiu (2002), was derived using Melnikov theory. More recently, Kovaleva (2005) extended the two-state theory of SR to underdamped systems.

Analytical methods for modeling the effects of colored noise on SR has focused almost exclusively on overdamped systems (Gammaitoni et al., 1989, 1998; Hänggi et al., 1993). An exception to this trend was presented by Gammaitoni et al. (1989) who approximated their underdamped system using overdamped methods. There have been no analytical methods developed for underdamped systems excited by colored noise.

Only a handful of experiments involving SR in systems excited by colored noise have been reported over the years. One of the first set of experiments was performed by Gammaitoni et al. (1989) using an underdamped circuit. More recently Misono et al. (1998) presented a study on an overdamped bistable optical system. Finally, a recent example using nanomechanical resonators excited by colored noise was provided by Dunn et al. (2009). While other experimental investigations are available, additional studies especially of underdamped systems are needed.

In this chapter, the results of an experimental study of an underdamped system excited by colored noise are presented. The underdamped system selected for the study is similar to the energy harvester investigated by Stanton et al. (2010, 2011). In addition, analytical expressions for SR in underdamped systems introduced by Kramers (1940), Simiu (2002), and Kovaleva (2005) are compared with the experimental results. It appears that Kovaleva's two-state approximation has never been compared with experimental data. The analytical expressions are also adapted to take into account the modal mass of the system. Finally, an alternative approach is suggested to adjust the underdamped expressions for systems excited by colored noise.

The content of this paper is organized as follows. First, the experimental approach taken is outlined including the method to identify parameters and evaluate the system response. Next, analytical methods are presented based on Kramers, Melnikov, and two-state approaches. Then, the analytical methods are compared with the experimental results. Finally, conclusions are draw and suggestions given for future work.

8.1 Experimental Approach

A base excited, double-well, composite beam with tip mass was selected for the experimental system as shown in Fig. 8.1. The beam has a polymer substrate with

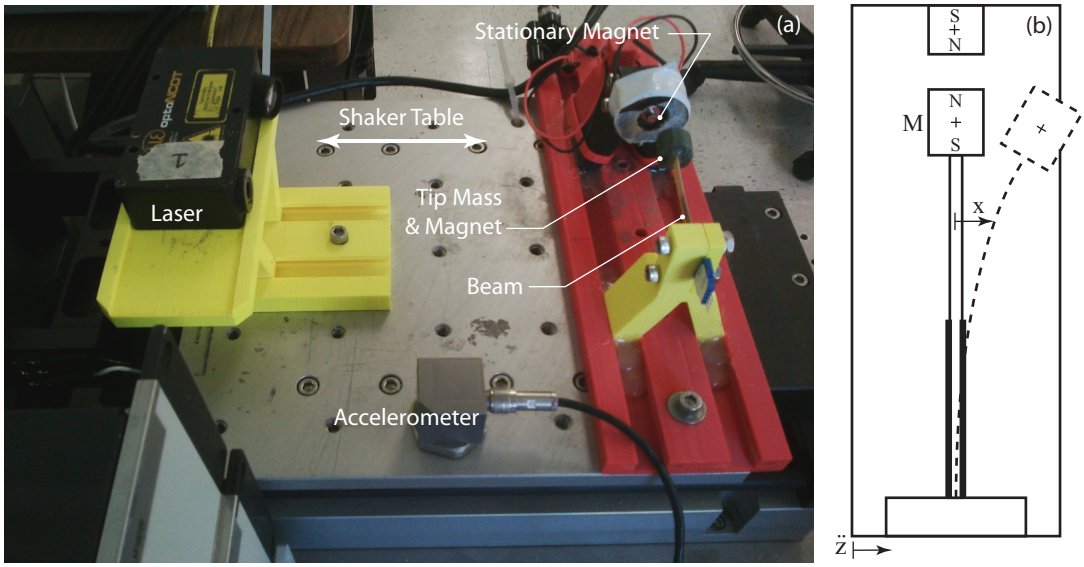

FIGURE 8.1: Experimental setup. Figure (a) shows a picture of the experimental setup with the location of the laser measurement system, accelerometer, stationary magnet, and the composite beam. Note that the stationary magnet is clamped to the shaker table. Figure (b) is a schematic of the system showing the beam displacement x and shaker table acceleration $\ddot{z}$.

piezoelectric laminates on both sides. The tip mass includes a magnet, and a corresponding stationary magnet is affixed to the shaker-table. The poles of the magnets are aligned so that they repel each other resulting in a bi-stable system. In the following subsections, the approach to identifying the system parameters and for generating the noise and signal are presented. Then, the methods for collecting and processing the data to estimate the average up-crossing period, spectral power amplification (SPA), and signal to noise ratio (SNR) are discussed.

8.1.1 System Identification

The schematic shown in Fig. 8.1(b) was used to derive the equations of motion and parameters of the system. The measurements taken consist of the deflection of the beam indicated by x and the acceleration of the base indicated by $\ddot{z}$. Stanton et al. (2011) demonstrated that the potential of such a tip-mass system can be closely approximated using a power series in the form of Eq. (8.2). This simplification has

also been made for in this chapter, and the equation of motion is given by

$$\tilde{m}\ddot{x}(t) = -\tilde{m}\gamma\dot{x}(t) - \tilde{m}U'(x) + A\sin(\Omega t) + \sigma_c W(t)\,, \tag{8.1}$$

where x is the deflection of the beam, γ is the damping coefficient, A is the signal amplitude, the prime represents a derivative with respect to x, and Ω is the frequency of the signal. The restoring force $U(x)$ is given by

$$U(x) = \sum_{n=1}^{N} \frac{1}{n+1} b_n^{n+1}\,, \tag{8.2}$$

with $N = 3$. The displacement reference $x = 0$ has been defined so that there is no offset term, thus $b_0 = 0$. The function $W(t)$ is white Gaussian noise with a standard deviation of σ_c which is defined later.

The harmonic balance parameter identification (HBID) method (Yasuda et al., 1988b; Yasuda and Kamiya, 1990) can be used to identify the dimensionless inertia coefficient $\tilde{m}$, damping coefficient γ, and the restoring force coefficients from Eq. (8.2). Tweten and Mann (2012a) demonstrated that the effect of a beam's modal mass can be taken into account using a dimensionless inertia coefficient $\tilde{m}$. In subsequent sections, the modified amplitude $\breve{A} = A/\tilde{m}$ is used to account for the effect of the modal mass on the analytical expressions for SR. The parameters identified for the present system in Table 8.1 were identified using the SNR weighting matrix from Tweten and Mann (2013). The signal had an amplitude of $A = 0.40$ (m/s^2) and a frequency of 1 Hz.

The standard deviation of the noise in Eq. (8.1) is defined by

$$\sigma_c^2 = \tilde{m}^2 \int_0^{\omega_{cut}} 2D\gamma\Psi(c,\omega)\,\mathrm{d}\omega\,, \tag{8.3}$$

where ω_{cut} is the maximum frequency of the noise spectrum (Simiu, 2002). The

Table 8.1: Parameters for composite beam system identified by HBID using the SNR weighting matrix.

$\tilde{m}$	γ	b_1	b_2	b_3
(unitless)	(1/s)	($1/s^2$)	($1/ms^2$)	($1/m^2s^2$)
6.41	2.66	-1300	6640	4.15×10^8

power spectral density $\Psi(c, \omega)$ and the noise intensity D are defined by

$$\Psi(c, \omega) = \frac{1}{1 + \left(\frac{c\omega}{2\pi}\right)^2}, \tag{8.4}$$

$$D = \frac{\alpha}{\gamma \tilde{m}^2}, \tag{8.5}$$

where c is the color coefficient, α is the power spectral density (PSD) of the base acceleration, and ω is the angular velocity in rad/s.

Figure 8.2 provides a comparison of the four color coefficients used in the experiments. The noise intensity for all curves in Fig. 8.2 was $D = 0.17 \times 10^{-3}$ (m^2/s^2) which corresponds to a spectral density of $\alpha = 0.019$ ((m^2/s^4)/Hz). Note that the single sided PSD is plotted in Fig. 8.2 so the curves approach 2α. The dotted curve is the input spectrum to the shaker-table which agrees well with the measured spectrum from the accelerometer.

A representative curve for the potential defined in Eq. (8.2) is plotted in Fig. 8.3. The two stable equilibrium points are x_1 and x_2, and the unstable equilibrium point at $x = 0$ is given by x_0. The energy barriers (or difference of energy between stable and unstable states) for x_1 and x_2 are E_{b1} and E_{b2}, respectively. The Kramers rate from state x_1 to state x_2 is given as r_{K1} as shown and the rate in the opposite direction is r_{K2}.

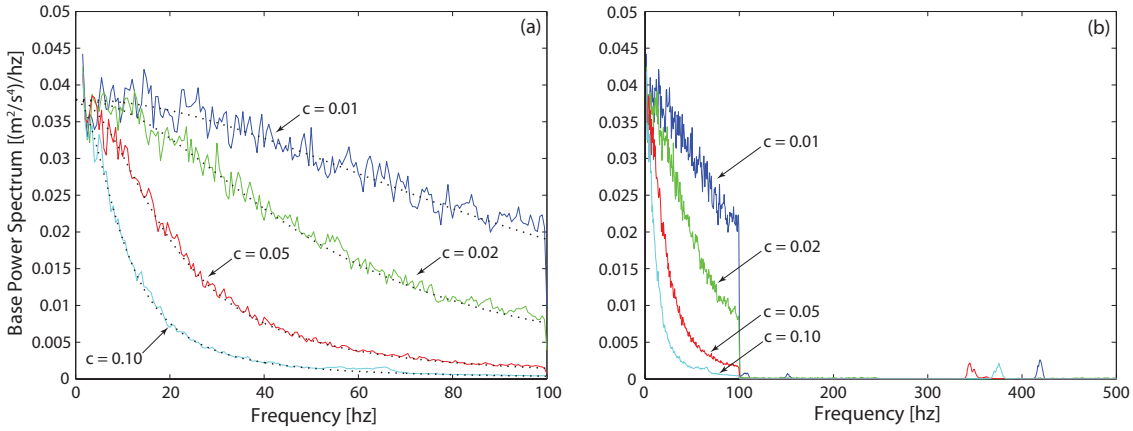

FIGURE 8.2: Experimentally determined PSDs of colored noise with color coefficients $c = 0.01$, 0.02, 0.05, and 0.10. Figure (a) provides a comparison between the input spectrum (dotted curves) and the measured PSD (solid curves). Figure (b) shows that the frequency content above the cut-off frequency $\omega_{cut} = 2\pi \cdot 100$ (rad/s) is negligible.

8.1.2 Experimental Methods

Estimating the position of the unstable equilibrium is necessary for determining the average up-crossing period. For example, Fig. 8.4 shows a time history of the deflection as a solid line and the unstable equilibrium position as a dashed line. The duration of a single up-crossing occurs after the systems crosses the unstable equilibrium position twice. Note that the system tends to spend extended periods of time on either side of the unstable equilibrium.

Measuring the unstable equilibrium point in the static case was not straight forward. Instead, the equilibrium from the dynamic data was estimated using a histogram such as the one shown in Fig. 8.5. Since the system tends to spend most of its time on either side of the unstable equilibrium, the unstable equilibrium appears as a minimum between two peaks. The histogram was fitted with a spline to automate the process of estimating the unstable equilibrium.

Up-crossing periods were determined by smoothing the deflection data using the

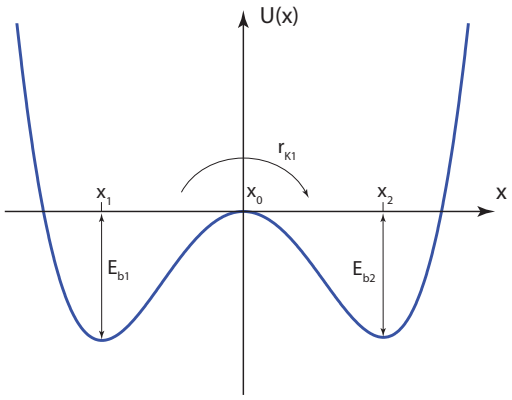

FIGURE 8.3: Energy $U(x)$ of a fourth order, bi-stable potential vs. deflection. The two stable equilibrium points are x_1 and x_2, and the unstable equilibrium point at $x = 0$ is x_0. The energy barriers for the stable equilibrium are E_{b1} and E_{b2}. The direction of Kramers rate for r_{K1} is indicated, and r_{K2} is in the opposite direction.

technique introduced by Garcia (2010) and then applying a two-state filter. The two-state filter was implemented with hysteresis using the same approach given by Lindner et al. (1995). The data smoothing and hysteresis prevented measurement noise and minor excursions from appearing as transitions between states as highlighted by Fig. 8.4. All up-crossing experiments where performed with white noise excitation ($c = 0$).

Two common methods for observing SR in the frequency domain are SNR and SPA. The following definitions of SNR and SPA are based on those given by McNamara and Wiesenfeld (1989)

$$\hat{S}(\Omega) = \frac{(P_{xx}(\Omega) - P_N(\Omega))\, G}{F_s\, N}\,, \tag{8.6}$$

$$\text{SNR} = \frac{\hat{S}(\Omega)}{P_N(\Omega)}\,, \tag{8.7}$$

$$\text{SPA} = \frac{P_{xx}(\Omega) - P_N(\Omega)}{P_{aa}(\Omega)}\,, \tag{8.8}$$

where $P_{xx}(\Omega)$ is the PSD of the total response and $P_N(\Omega)$ is the PSD of the response due to noise excitation alone at the frequency Ω. In addition, $P_{aa}(\Omega)$ is the PSD

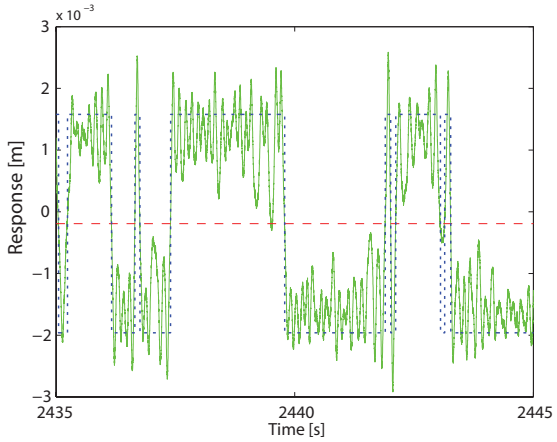

FIGURE 8.4: An example of the system response to white noise without a signal is shown ($D = 0.43 \times 10^{-3}\,\mathrm{m}^2/\mathrm{s}^2$). Experimental deflection (solid curve), estimated unstable equilibrium (dashed curve), and two-state filtered data (dotted curve) are plotted versus time. Note that due to the hysteresis, not all of the excursions past the centerline are considered a change of state.

of the base acceleration at the frequency Ω, F_s is the sample frequency, N is the number of samples in the PSD, and G is the equivalent noise bandwidth. Since the PSD of a signal varies with N, the estimated signal power $\hat{S}$ was chosen to calculate the SNR. For the SPA, as long as the same N is used for both $P_{xx}(\Omega)$ and $P_{aa}(\Omega)$, the ratio of the two terms will be identical to the ratio of the output to input powers.

All PSDs were created using Welch's method (Welch, 1967) with a Tukey window ($\alpha = 0.5$) and an overlap of about 99% which is a similar approach taken by both McNamara and Wiesenfeld (1989) and Lindner et al. (1995). For both $P_{xx}(\Omega)$ and $P_{aa}(\Omega)$, the number of samples in each window was $N = 2\pi \cdot 50/\Omega$ which placed the signal frequency at a bin center resulting in no scallop loss. The signal response peak was found by selecting the magnitude at the signal bin. For the noise estimate $P_N(\Omega)$, the number of samples in each window was $N = 2\pi \cdot 10/\Omega$. Reducing the number of samples for $P_N(\Omega)$ facilitated automating the noise response, which was accomplished by fitting a smoothing spline to the bins on either side of the signal bin. It should be noted that none of the signals were smoothed before estimating the

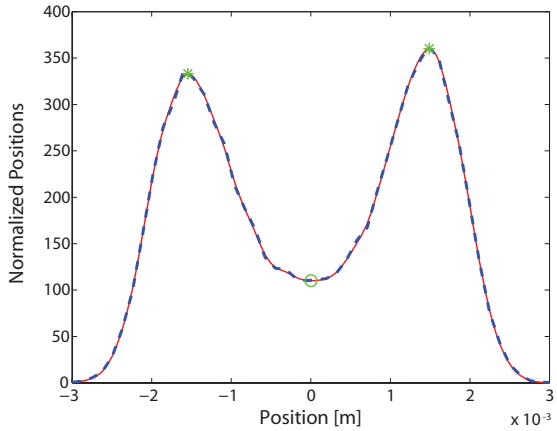

FIGURE 8.5: Normalized histogram of the beam deflection excited by white noise without a signal ($D = 0.43 \times 10^{-3}\,\mathrm{m}^2/\mathrm{s}^2$). The dashed curve is the original histogram and the solid curve is a smoothing spline generated. The peaks of the spline are indicated with stars, and the minimum between the peaks is indicated by the circle.

PSD. The equivalent noise bandwidth of $G = 1.22$ was taken from Harris (1978).

An example of the automated procedure for estimating $P_{xx}(\Omega)$ and $P_N(\Omega)$ is shown in Fig. 8.6. The 50 cycle PSD is given by the dashed curve with the star indicating the signal response peak. The 10 cycle PSD is shown by the solid curve with the cross indicating the automatically estimated noise response.

For all of the experiments, the position and acceleration data was taken at a 1000 Hz sample rate after passing through a 500 Hz analogue, anti-aliasing filter. The output signal was passed through a 300 Hz low-pass filter before being sent to the power amplifier. The cut-off frequency for the noise spectrum was 100 Hz in all cases. In addition, the SR experiments included a weak signal. Unfortunately, the amplitudes varied slightly from experiment to experiment which impacted the quality of the comparison of the SNR between experiments. In order to overcome this limitation, the experimental SNRs were multiplied by the proscribed signal power and then divided by the experimental signal power for each data point.

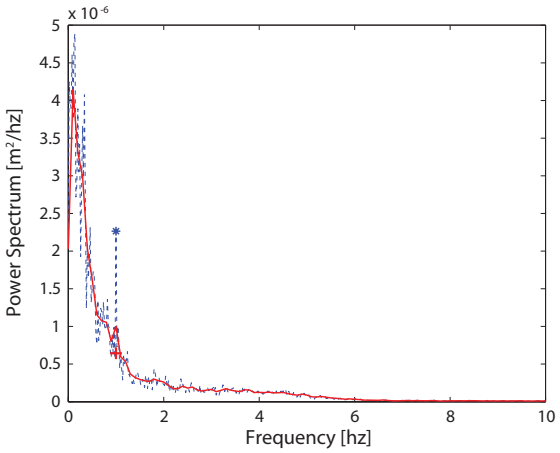

FIGURE 8.6: An example of the experimental PSD of the deflection response for colored noise with the signal ($D = 0.43 \times 10^{-3}\,\mathrm{m}^2/\mathrm{s}^2$). The dashed curve is the 50 cycle PSD, and the solid curve is the 10 cycle PSD. The star indicates the estimated peak response, and the cross indicates the estimated noise response of the system.

8.2 Analytical Approach

This section presents the underdamped equations for Kramers rate, Melnikov theory, and two-state theory. The underdamped Kramers and Melnikov rates are compared with the average up-crossing periods found experimentally in Section 8.3.1. The Melnikov method is also used for a proposed adjustment for colored noise. Expressions for SNR and SPA which are based on the underdamped, two-state theory are compared with the experimental results in Section 8.3.2.

8.2.1 Kramers Rate

The underdamped Kramers rate of a system, also referred to as an energy-diffusion-limited rate, is the average escape rate from a potential well (Hanggi et al., 1990). For symmetric bistable systems, Kramers rates for both wells are identical, but for the more general case of unsymmetric potentials, the escape rates out of each well are different. The equations for this more general case are given by Hanggi et al.

(1990) as

$$r_{K1} = (1-p)\,\gamma \frac{\omega_2 I(E_{b1})}{2\pi D} \exp\left(-\frac{E_{b1}}{D}\right) \tag{8.9a}$$

$$r_{K2} = p\,\gamma \frac{\omega_1 I(E_{b2})}{2\pi D} \exp\left(-\frac{E_{b2}}{D}\right) \tag{8.9b}$$

where r_{K1} and r_{K2} are the escape rates from the potential wells about the equilibrium positions x_1 and x_2, respectively. The natural frequencies ω_1 and ω_2 at the stable equilibriums are given by $\sqrt{U''(x_1)}$ and $\sqrt{U''(x_2)}$, respectively which for the present system are $\omega_1 = 50.8$ and $\omega_2 = 51.1$ (rad/s). The probability p is given by

$$p = \frac{I(E_{b1})}{I(E_{b1}) + I(E_{b2})}\,. \tag{8.10}$$

The terms $I(E_{b1})$ and $I(E_{b2})$ are the action at the barrier energy for the potential wells about x_1 and x_2, respectively (Hanggi et al., 1990). The actions are calculated by integrating the area within the homoclinic orbits (Hanggi et al., 1990; Kramers, 1940) which are shown for the present system in Fig. 8.7. If the equation of motion includes a mass term, than the integration must be of the momentum around the homoclinic orbit. It is easily shown that the homoclinic velocity in terms of position for a non-symmetric, fourth-order polynomial, potential function is given by

$$v_h(x) = \pm\sqrt{-b_1 x^2 - \frac{2}{3} b_2 x^3 - \frac{1}{2} b_3 x^4}\,, \tag{8.11}$$

where the expression is valid between 0 and the equilibrium points x_1 or x_2.

The up-crossing period is the time taken to escape both wells consecutively. For unsymmetrical potential wells, the up-crossing period can be approximated by

$$\tau_K = \frac{1}{r_{K1}} + \frac{1}{r_{K2}}\,. \tag{8.12}$$

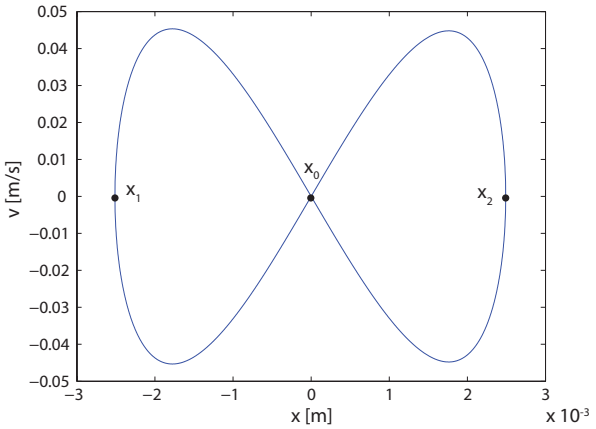

FIGURE 8.7: Estimated homoclinic orbit of the experimental system. The stable equilibrium points are x_1 and x_2, and the unstable equilibrium point is x_0.

Note that Hanggi et al. (1990) indicates that Eq. (8.9) is valid as long as the following conditions are applicable

$$D << E_b \,, \text{and} \tag{8.13}$$

$$\gamma I(E_b) << D \,. \tag{8.14}$$

For the first condition, the value of the smaller energy barrier is $E_{b2} = 0.0011$ which implies the noise intensity must be much less than 1×10^{-3} $[\text{m}^2/\text{s}^2]$ for Eq. (8.9) to be valid. For the second condition, the product of the damping and action is $\gamma I(E_{b2}) = 0.00048$ which implies the noise intensity must be much larger than 0.5×10^{-3} $[\text{m}^2/\text{s}^2]$ for Eq. (8.9) to be valid. The result is that the Kramers approach is not likely to model the system well.

8.2.2 Melnikov Methods

The Melnikov approach provides a second, independent method for predicting the average up-crossing period which does not have the same limitations as the Kramers

approach (Simiu, 2002). The mean up-crossing period is given by

$$\tau_S = a^{-1}\sqrt{\frac{2\pi}{D}}\exp\left(\frac{E_b}{D}\right)\,, \tag{8.15}$$

$$a^{-1} = \int_0^\infty \exp\left(-\frac{U(x)}{D}\right)\,\mathrm{d}x\,, \tag{8.16}$$

where E_b is the energy barrier of a symmetric system (Simiu, 2002). Because the homoclinc orbits are nearly identical for the composite beam, the average of the energy barriers is a good approximation for E_b.

It is also possible to use Melkinov theory to predict whether a system will enter a chaotic state due to a forcing signal. Simiu (2002) demonstrated that this method can also be used to determine if a signal or set of signals is "weak" which is a necessary condition for SR (Anishchenko et al., 1999; Gammaitoni et al., 1998). A signal is weak if it is too small to induce chaos or an interwell response. The following Melnikov inequality is a necessary condition for chaos

$$-4\gamma/3 + \check{A}S(\Omega) > 0\,, \tag{8.17}$$

where $S(\omega)$ is the Melnikov scale factor defined in Eq. (8.18) (Simiu, 2002). For the signal $\check{A}$ of the present system, the term on the left is about -3.6 which means that the signal amplitude is not large enough to induce chaos in the system and is therefore a "weak" signal.

The Melnikov scale factor is given by Simiu (2002) as

$$S(\omega) = \int_{-\infty}^{\infty} h(t)\sin(\omega t)\,\mathrm{d}t\,. \tag{8.18}$$

The term $h(t)$ in this case is the same as the velocity component $v_h(t)$ of the homoclinic orbit as a function of time which was found by Litak and Borowiec (2006) to

be

$$h(t) = \frac{4x_1x_2\alpha \exp(\alpha(t-t_0))\left((x_1-x_2)^2 - \exp(2\alpha(t-t_0))\right)}{\left((x_1-x_2)^2 + \exp(2\alpha(t-t_0)) - 2(x_1+x_2)\exp(\alpha(t-t_0))\right)^2}\,, \tag{8.19}$$

Since the homoclinic orbits are nearly symmetric, the scale factor for the potential well about x_2 was selected to represent both wells. The terms t_0, α, x_1 and x_2 in Eq. (8.19) are given by

$$t_0 = -\frac{\ln|x_1 - x_2|}{\alpha}\,, \tag{8.20}$$

$$\alpha = \sqrt{-\frac{x_1x_2b_3}{2}}\,, \quad \text{and} \tag{8.21}$$

$$x_{1/2} = \frac{(-2b_2/3) \mp \sqrt{(2b_2/3)^2 - 2b_1b_3}}{b_3}\,. \tag{8.22}$$

The Melnikov scale factor can also be used to assess how the frequency spectrum of the noise affects the escape rate of a system. A useful relationship noted by Simiu (2002) is that as the integral

$$I = \int_0^{\omega_{cut}} \Psi(c,\omega)S(\omega)^2\,\mathrm{d}\omega \tag{8.23}$$

increases, so does the escape rate. Thus, if the colored noise cuts off the peak of the scale factor, the escape rate will decrease (Simiu, 2002). Figure 8.8 compares the Melnikov scale factor (with the peak normalized to unity) and the noise spectrums from Eq. (8.4). Based on Fig. 8.8, it is expected that response to the $c = 0.10$ noise spectrum will exhibit the greatest difference from white noise.

It is well known that the peak (e.g. ideal) SNR and SPA as well as the noise intensity at which the peak occurs is affected by colored noise. To address this shift due to colored noise, scaling the noise intensity in Eq. (8.4) with a normalized

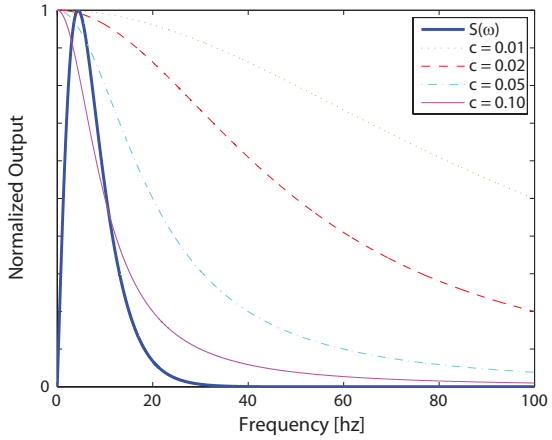

FIGURE 8.8: The Melnikov scale function normalized to the peak value and the various colored noise spectrums are plotted versus frequency.

realization of the integral in Eq. (8.23) is proposed. This relationship is given by

$$D_c = D\left(\frac{I}{\int_0^{\omega_{cut}} S(\omega)^2\,\mathrm{d}\omega}\right) = DI', \tag{8.24}$$

where D_c is the scaled noise intensity with the color coefficient c, and I' is the normalized integral. The normalized integral for both wells of the current system are compared in Table 8.2 for the four color coefficients used in this paper and white noise ($c = 0$). Since both integrals are nearly identical, I_2' was selected to generate all scaled noise intensities. Scaling the noise intensity in this way is similar to the decoupled approximation briefly mentioned by Hänggi et al. (1993).

8.2.3 Two-State Methods

Recently, the two-state theory was extended to underdamped systems by Kovaleva (2005). The surprising result of Kovaleva's work is that many of the expressions developed for overdamped systems can be used for underdamped cases. In particular, the underdamped expressions for SPA and SNR are valid for an underdamped system if the overdamped Kramers rate is replaced by the underdamped rate from Eq. (8.9).

Table 8.2: Normalized Melnikov integrals for the color coefficients used in the experiments. The scaled noise intensities D_c are calculated by multiplying the white noise intensity D with the normalized integral I_2'.

c	0.00	0.01	0.02	0.05	0.10
I_1'	1	0.995	0.982	0.906	0.739
I_2'	1	0.995	0.982	0.907	0.741

Thus, the expressions for SPA and SNR used to predict the experimental results in this work are based on the well know equations for two-state theory.

The magnitude of the SR response is given by Anishchenko et al. (1999) as

$$X_1(D) = \frac{2\check{A}x_m^2 r_K}{D\sqrt{4r_K^2 + \Omega^2}}\,, \tag{8.25}$$

where r_K is the Kramers rate, and x_m is the average magnitude of the two equilibrium positions given by

$$x_m = \frac{x_1 - x_2}{2}\,. \tag{8.26}$$

The SPA of the response is therefore given by

$$\eta = \frac{X_1^2}{A^2} = \left(\frac{\check{A}}{A}\right)^2 \cdot \frac{4r_K^2 x_m^2}{D^2\left(4r_K^2 + \Omega^2\right)}\,. \tag{8.27}$$

In the case of the composite beam, the term $(\check{A}/A)^2$ is reduced to $1/\tilde{m}^2$. For systems without a modal mass, the term $(\check{A}/A)^2$ reduces to unity and Eq. (8.27) becomes the same as the one presented by Anishchenko et al. (1999).

The noise response of the system is given by Anishchenko et al. (1999) as

$$G_N(\Omega) = \frac{4x_m^2 r_K}{4r_K^2 + \Omega^2}\left(1 - \frac{X_1^2(D)}{2x_m^2}\right)\,, \tag{8.28}$$

from which the SNR can be calculated. To be consistent with the experimental expression defined in Eq. (8.7), the SNR is defined for the two-state theory by

$$SNR = \frac{X_1^2}{G_N(\Omega)}\,, \tag{8.29}$$

where X_1^2 is equivalent to $\hat{S}$.

8.3 Experimental Results

In this section, the analytical methods from Section 8.2 are compared with the experimental results. First, mean up-crossing periods are compared for white noise excitation. Second, analytical and experimental SNR and SPA results are compared for colored noise excitation.

8.3.1 Average Up-Crossing Period

The average up-crossing periods predicted by the Melnikov approach in Eq. (8.15) and the Kramers approach in Eq. (8.12) are compared with the experimental results in Fig. 8.9. The Melnikov approach compares well to the experimental data especially

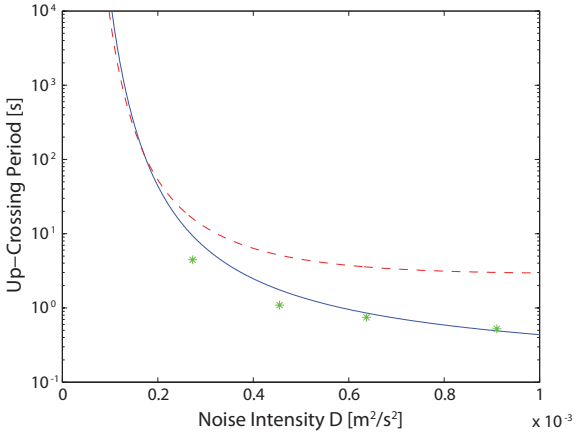

FIGURE 8.9: Comparison of average up-crossing periods calculated using the Melnikov approach (solid curve) and the Kramers approach (dashed curve) with experimental data (stars).

at larger noise intensities (shorter periods). For each experiment, a total number of 3.528×10^6 data points were used which is about one hour in duration. Since each experiment had the same length of time, longer experiments for the smaller noise intensities would have resulted in a closer comparison. For the smallest noise intensity at 0.091×10^{-3} [m^2/s^2], no crossings were observed. This observation is consistent with the predicted average up-crossing period of nearly 4 hours.

While the Melnikov approach performed well, the Kramers approach did a poor job of predicting the average up-crossing period. However, this is not surprising as the conditions in Eq. (8.13) were not met. In fact, based on Eq. (8.13) it would appear that the Kramers approach would not be valid for any level of noise intensity in the present system. It is interesting to note, though, that both the Melnikov and Kramers approaches tend to agree for noise intensities smaller than 0.2×10^{-3} [m^2/s^2]. This suggests that the lower limit given in Eq. (8.13) may not be applicable for the present system.

Estimating the average up-crossing rate accurately is important to predict the SNR and SPA using two-state theory. The average escape rate r_K is used for both the SNR in Eq. (8.29) and SPA in Eq. (8.27). In developing the two-state theory for underdamped systems, Kovaleva (2005) used the Kramers approach in Eq. (8.9) for the escape rate. However, for the present system the Kramers approach will not lead to good results. Instead, the Melnikov approach was chosen to model the escape rate. Since the system was nearly symmetric, the assumption by the Melnikov approach of symmetry was not a limitation.

8.3.2 Frequency Response

The four color coefficients and resulting noise spectrums presented in Fig. 8.8 were applied to the composite beam system. For each color coefficient, eleven noise intensities D were applied: 0.17, 0.26, 0.35, 0.43, 0.52, 0.61, 0.69, 0.78, 0.87, 0.95, and 1.0

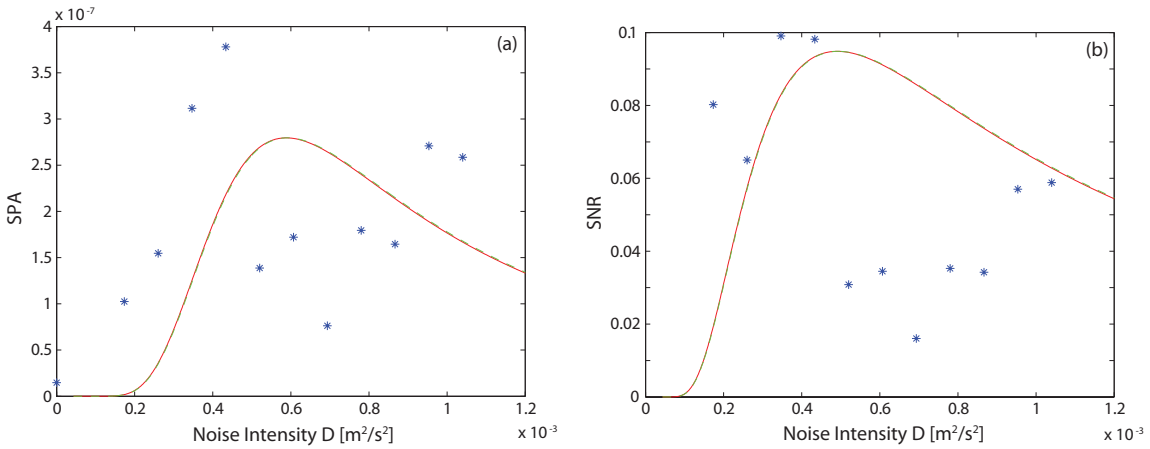

FIGURE 8.10: Comparison of experimental and analytical SPA and SNR for the color coefficient $c = 0.01$. Figure (a) compares the experimental (stars), two-state (solid curve), and color adjusted two-state (dashed curve) SPA of the system. Figure (b) compares the experimental (stars), two-state (solid curve), and color adjusted two-state (dashed curve) SNR of the system.

($\times 10^{-3}\,\mathrm{m}^2/\mathrm{s}^2$). In addition, a single experiment was performed with only the signal (D=0). A total number of 4.9×10^5 samples was used for each experiment.

Comparisons for the $c = 0.01$ noise spectrum between experimental and theoretical SNRs and SPAs are given in Fig. 8.10. Since the calculation of the SPA is not explicitly dependent on the signal amplitude, the variance in the signal amplitude had little impact on the comparisons. The initial slope of the theoretical SPA up to the peak agrees well with the experimental values in Fig. 8.10(a). For larger noise intensities ($D > \ 0.6 \times 10^{-3}$), the theoretical curve does not predict the experimental trend as well. The proposed color adjustment in Eq. (8.24) has little affect on the theoretical SPA in this case. This indicates that the $c = 0.01$ noise spectrum does not differ much from white noise for this system. From Fig. 8.10(b), it is difficult to draw conclusions on whether the theoretical SNR matches the experimental results.

Comparisons for the $c = 0.02$ noise spectrum between experimental and theoretical SNR and SPA are given in Fig. 8.11. The comparison of the SPAs for the

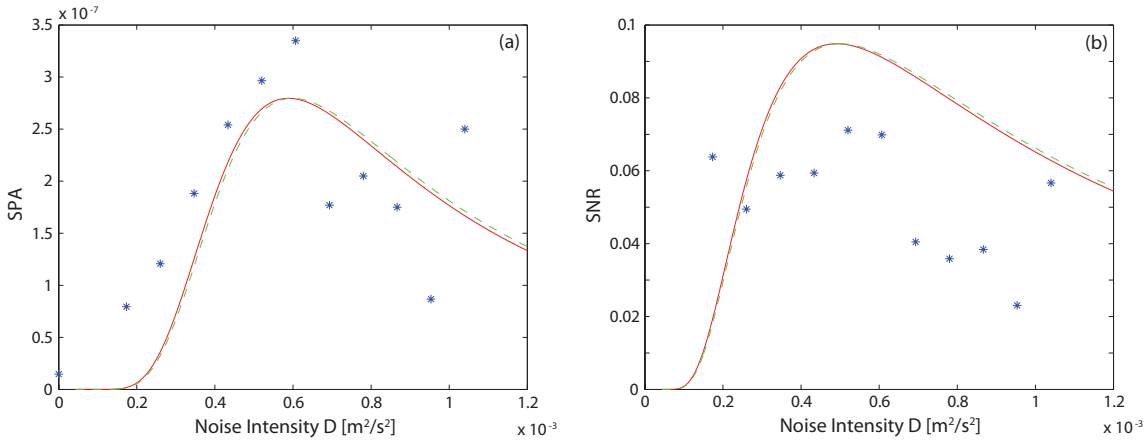

FIGURE 8.11: Comparison of experimental and analytical SPA and SNR for the color coefficient $c = 0.02$. Figure (a) compares the experimental (stars), two-state (solid curve), and color adjusted two-state (dashed curve) SPA of the system. Figure (b) compares the experimental (stars), two-state (solid curve), and color adjusted two-state (dashed curve) SNR of the system..

initial slope is better than in the $c = 0.01$ case, and the results for intensities past the SPA peak show agreement for some intensities unlike the $c = 0.01$ data. Again, the color adjustment for the $c = 0.02$ noise spectrum appears little different from the response due to white noise. Based on Fig. 8.11(b), it is difficult to determine whether the theoretical SNR is a good fit for the experimental system, although the trend is closer than for the $c = 0.01$ data.

Comparisons for the $c = 0.05$ noise spectrum between experimental and theoretical SNR and SPA are given in Fig. 8.12. The comparison of the SPAs for the initial slope is excellent in Fig. 8.12(a). The results for intensities past the SPA peak show good agreement for several data points. For the color coefficient of $c = 0.05$, the color adjusted curve begins to separate from the response due to white noise. The experimental SNRs in Fig. 8.12(b) hover around the theoretical values, and show some agreement for intensities past the SNR peak.

Comparisons for the $c = 0.10$ noise spectrum between experimental and theo-

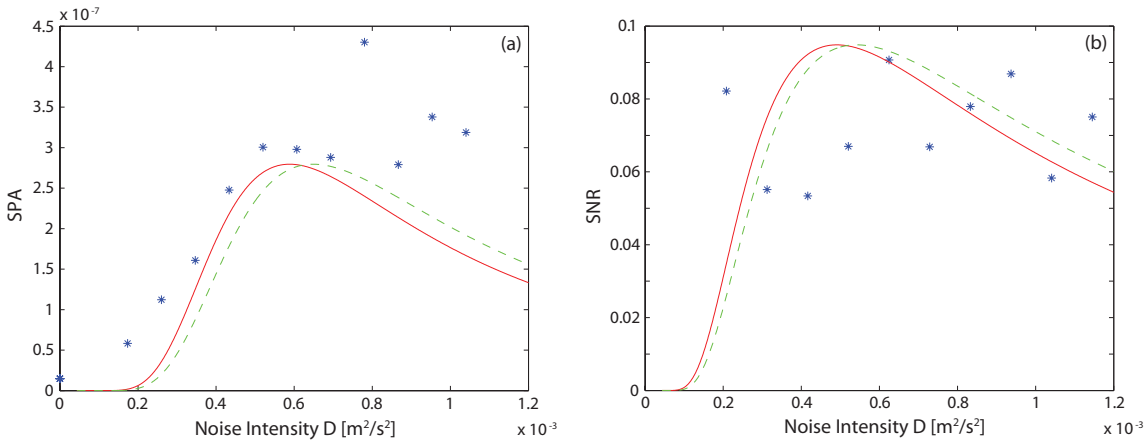

FIGURE 8.12: Comparison of experimental and analytical SPA and SNR for the color coefficient $c = 0.05$. Figure (a) compares the experimental (stars), two-state (solid curve), and color adjusted two-state (dashed curve) SPA of the system. Figure (b) compares the experimental (stars), two-state (solid curve), and color adjusted two-state (dashed curve) SNR of the system..

retical SNR and SPA are given in Fig. 8.13. As with the $c = 0.05$ SPA results, there is good agreement between theoretical and experimental SPAs. A few larger experimental SPAs around the peak are the exception of this trend. In the $c = 0.10$ case, the effects of the color adjustment proposed in Eq. (8.24) are most clearly seen. The analytical prediction using the adjusted noise intensity agrees well with the experimental results for all but a few of the noise intensities. This indicates that the proposed adjusted color method has promise for predicting SR for systems under colored noise and is consistent with the data.

The theoretically predicted SNRs for $c = 0.10$ in Fig. 8.13(b) are the closer to the experimental values than any of the other data sets. It is interesting to note the large experimental SNR at the noise intensity of $D = 0.17 \times 10^{-3}\,(\mathrm{m}^2/\mathrm{s}^2)$. This large increase of SNR for a low noise intensity is consistent with the theoretical examples given by Anishchenko et al. (1999) using linear response theory. The increase in SNR for low noise intensities is due to intrawell dynamics and is not predicted by two-state

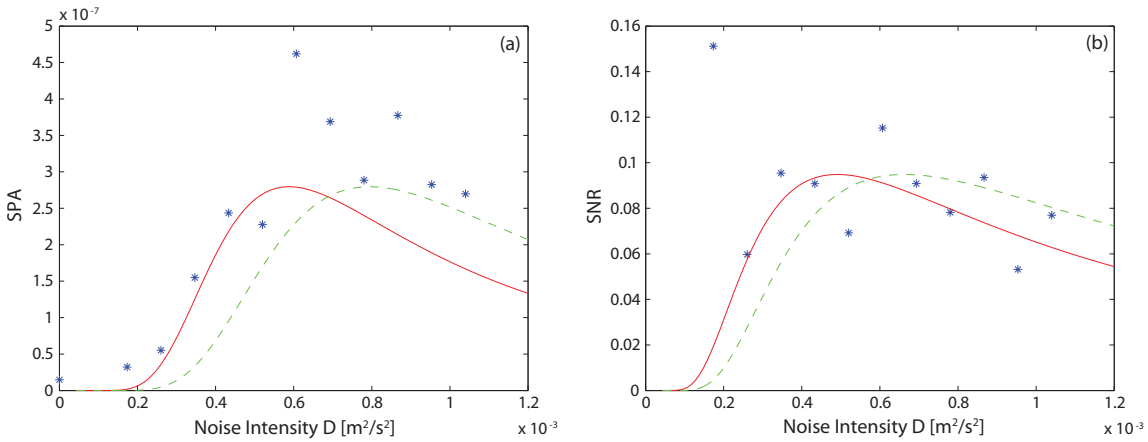

FIGURE 8.13: Comparison of experimental and analytical SPA and SNR for the color coefficient $c = 0.10$. Figure (a) compares the experimental (stars), two-state (solid curve), and color adjusted two-state (dashed curve) SPA of the system. Figure (b) compares the experimental (stars), two-state (solid curve), and color adjusted two-state (dashed curve) SNR of the system..

theory. Therefore, the spike in SNR appears to indicate that the experimental SNR follows the typical SR pattern, but the pattern is being obscured by variations in signal amplitude.

8.4 Summary and Conclusions

In this chapter, an experimental study of stochastic resonance in an underdamped, bistable, composite beam excited by colored noise was presented. Analytical methods were compared with the experimentally determined average up-crossing period, SPA, and SNR for a variety of colored noise spectrums. For the two-state approach, this paper presents the first comparison with experimental results. In addition, a new approach for adjusting the SPA and SNR analytical expressions for colored noise was proposed.

The following results and conclusions were found for the experimental system and analytical approaches. First, it was shown that the Melnikov approach for predicting

average up-crossing periods was a better method for predicting the behavior of the composite beam system than the underdamped Kramers approach. In fact, the Melnikov approach agreed well with the experimental data. It should also be noted that the system was outside the valid limits of the Kramers approach so it is not surprising that it performed poorly in this case.

Second, the two-state analytical approach was found in general agreed well with the experimental SPA. A few exceptions occurred for noise intensities above the peak SPA. In addition, the use of the escape rates from the Melnikov approach was demonstrated to be a valid adaptation for the two-state approach. This is significant because the derivation of the two-state theory assumed the Kramers escape rate for underdamped systems. Unfortunately, the comparison of the experimental and analytical SNRs was not clear in every case. This is due to the limitation of the experiment in which the signal amplitude was not constant. Finally, the proposed scaled noise method for colored noise was consistent with experimental data.

An opportune extension of the work in this paper is the exploration of a stochastic resonant, piezoelectric beam energy harvester. Based on both the successes and limitations of the experimental setup described in this chapter, the following recommendations can be made for future work. A metal substrate such as brass is a better choice for the piezoelectric beam. Such a material change avoids material creep present in polymer substrates and increases the first natural frequency of the system. This change would both increase the repeatability of experiments and allow for larger signal frequencies. Additionally, the signal amplitude should be actively controlled if the experimental setup tends to induce variation in the signal amplitude. A more consistent signal amplitude will improve comparisons between analytical and experimental SNRs.

9

Summary

Multistable systems present innumerable challenges for investigators. The chapters in this dissertation have explored, applied, and improved methods to understand multistable systems and predict their behavior. In addition, methods that leverage opportunities not available in linear systems have been explored. The techniques discussed in the previous chapters fall into the categories of parameter identification, delay feedback control, and stochastic resonance.

9.1 Conclusions

In chapter 2, applications of and improvements to the harmonic balance identification (HBID) were discussed. First, experimentally identified parameters of a weakly nonlinear, base excited, beam energy harvester were presented. An experimental approach to determine the number of restoring force coefficients and Fourier coefficients required for convergence was introduced. Then, parameters for a non-linear energy harvester were then identified using HBID. The accuracy of the nonlinear parameters were demonstrated by comparing frequency sweeps of both simulations based on the parameters and experimental data. Next, the effects of weighting matrices on

the accuracy of parameter estimation using the HBID method were explored. The exponential and SNR weighting strategies were introduced and demonstrated to perform better than the typically used identity matrix. Finally, a method for identified parameters using a limited phase space was successfully established.

The logarithmic decrement method was explored in chapter 3 for potential improvements. An uncertainty analysis was presented in which the uncertainty of the damping ratio was found in terms of the uncertainty of the displacement and period. Factors such as the number of periods, uncertainties in the peak and period measurements, and the affect of damping itself were taken into consideration. Ultimately, it was found that one simply needed to estimate the damping to determine the ideal number of periods to use. This information was distilled into a single figure for a wide range of uncertainties and damping ratios.

In chapter 4, the semi-discretization, spectral element, and Legendre collocation methods for solving delay differential equations were presented and contrasted. The methods were compared for relative convergence rate and computational time using three numerical studies consisting of a ship stability example, the delayed damped Mathieu equation, and a helicopter rotor control problem. The spectral element method was found to have the quickest convergence rate for all three studies, but the Legendre collocation method had the shortest computational time. The semi-discretization method did not converge for any of the numerical studies and required the longest computational time of all three studies.

In chapter 5, the spectral approach was introduced which applies the spectral element method to evaluate chaos control. The spectral approach determines the Floquet exponents (FE)s of unstable periodic orbits (UPO)s and equilibrium states stabilized by such techniques as extended delayed feedback control (EDFC) or multiple delay control (MDFC). The spectral approach was applied to Duffing systems including an example of an UPO with an odd number of unstable FEs. The FEs cal-

culated by the spectral approach were compared to results published using previously established methods. The spectral approach was also successfully used to analyze a higher dimensional, asymmetrical system with a UPO in chaos arising from tori doubling.

In chapter 6, the spectral approach was applied to self-excited systems with arbitrary delays. The method was first applied to the half-period, delayed feedback control (DFC) of a Lorenz system. The spectral approach was then successfully applied to evaluate DFC and EDFC of a Toda oscillator with control loop latency. Finally, steady state control of a Rössler system via MDFC was analyzed using the spectral approach. In all the cases, the spectral approach results agreed well with previously published results.

In chapter 7, a number of well established numerical models and analysis methods were presented. The numerical methods include spectral power amplification (SPA), signal to noise ratio (SNR), residual time distributions (RTD), and the phase lag between signal input and switching. The numerical methods were applied to simulated data and then compared to equivalent calculations for analytical models; the trends in both the analytical methods and the simulated data agreed well. Finally, stochastic resonance as a true resonance was highlighted using the first RTD peak plotted versus signal frequency.

Stochastic resonance of a base excited, double-well, composite beam excited by colored noise was experimentally observed in chapter 8. First, it was shown that the Melnikov approach for predicting average up-crossing periods was a better method for the composite beam system than the underdamped Kramers approach. Then, the two-state analytical approach using rates from Melnikov theory was compared with the experimental SPA and SNR for a variety of noise intensities. The theoretical SPA values matched the experimental data well for most cases. The exception was for a few noise intensities above which the peak SPA occurred. Unfortunately, the

experimental and analytical SNRs could not be compared clearly. This is due to the limitation of the experiment in which the signal amplitude was not constant. Finally, the proposed scaled noise method for adjusting the analytical method for colored noise was found to be consistent with experimental data.

9.2 Future Work

The work outlined above provides a number of opportunities for new applications and extensions of the methods. The most interesting opportunities revolve around extensions to the harmonic balance identification method, delayed feedback control, and stochastic resonance in bistable beams which are presented below.

In the HBID method explored in Chapter 2, it was assumed that the entire data set for parameter identification was available. However, in some cases, not all of the data is available at once or the system parameters change. In these cases, it would be advantageous to continually estimate parameters or update estimated parameters. The opportunity is to extend the HBID method to continuously estimate parameters. One potential approach is to use a Kalman filter to derive such a method for HBID, but other options may be explored. It would also be valuable to determine a method to continuously estimate parameters in a chaotic response. Yuan and Feeny (1998) already demonstrated that such parameter identification is possible but relied on using an entire data set. A particularly compelling application for a continuous identification scheme for chaos is code breaking. Cuomo and Oppenheim (1993) presented a method to mask electronic communications using chaos to essentially encrypt and recover messages. A Kalman filter approach or similar method to identify parameters and then synchronize with such a system has the potential to crack communications encrypted using chaos.

The spectral approach in chapters 5 and 6 was shown to successfully predict the stabilization of UPOs and equilibrium states. In each of these cases, the usual

method of constant feedback gain was applied. An option that has not been explored in the literature is piecewise control of chaos. A few basic applications of piecewise control include reducing control output, switching between orbits, and control of problematic orbits. The control output power when using delayed feedback control approaches zero, but in the presence of noise, the feedback never truly reaches zero. For cases in which conserving power is of the utmost importance, restricting the feedback to a percentage of the orbit makes sense. Determining the limitations of such an approach has the potential to extend the delayed feedback method to new applications. For chaotic responses with more than one orbit with the same period, it is not always possible to select the desired orbit. Piecewise control could be an effective method to ensure the desired orbit is stabilized or to switch between orbits. Finally, some UPOs are notoriously difficult to stabilize (Just et al., 2007). It would be advantageous to determine if piecewise control can provide another method of stabilizing such UPOs.

Stochastic resonance in a bistable, composite beam was observed in chapter 8. With limited underdamped, experimental work available in the literature, two worthwhile extensions of the work in this chapter are energy harvesters and chains of oscillators. Research into energy harvesting using bistable beams is currently focused on resonant responses (Stanton et al., 2010, 2011). Exploiting stochastic resonance for energy harvesting would greatly expand the number of deployment options for energy harvesters. The focus of this additional work is to determine whether stochastic resonance increases output power. Arrays of resonators undergoing stochastic resonance are know to be capable of amplifying the resonance response (Lindner et al., 1995). Much of the focus of this topic has been related to overdamped systems (Lindner et al., 1995; Löcher et al., 1998; Gao et al., 2001; Anishchenko et al., 2007). Experimental observation of the response of underdamped arrays with stochastic resonance would be a valuable addition to the literature. Determining the effects of different

methods for linking the resonators is important for future work and applications. Ideal applications of the research includes mechanical sensors and energy harvesters.

Bibliography

Ahlborn, A. and Parlitz, U. (2005), "Controlling dynamical systems using multiple delay feedback control," *Phys. Rev. E*, 72, 016206.

Amann, A., Schöll, E., and Just, W. (2007), "Some basic remarks on eigenmode expansion of time-delay dynamics," *Physica A*, 373, 191–202.

Andó, B. and Graziani, S. (2000), *Stochastic Resonance: Theory and Applications*, Kluwer Academic Publishers.

Anishchenko, V., Neiman, A., Moss, F., and Schimansky-Geier, L. (1999), "Stochastic resonance: noise-enhanced order," *Physics-Uspekhi*, 42, 7–36.

Anishchenko, V., Astakhov, V., Neiman, A., Vadivasova, T., and Schimansky-Geier, L. (2007), *Nonlinear Dynamics of Chaotic and Stochastic Systems*, Springer-Verlag.

Arcara, P., Bittanti, S., and Lovera, M. (2000), "Periodic Control of Helicopter Rotors for Attenuation of Vibrations in Forward Flight," *IEEE Transactions on Control Systems Tehcnology*, 8, 883–894.

Balogh, L., Kollar, I., and Gueret, G. (2002), "Variance of Fourier Coefficients Calculated from Overlapped Signal Segments for System Identification," in *Proceedings Of The 19th IEEE Instrumentation And Measurement Technology Conference*, vol. 2, pp. 1065–1070.

Benettin, G., Froeschle, C., and Scheidecker, J. P. (1979), "Kolmogorov entropy of a dynamical system with an increasing number of degrees of freedom," *Phys. Rev. A*, 19, 2454–2460.

Berrut, J. and Trefethen, L. N. (2004), "Barycentric Lagrange Interpolation," *SIAM Review*, 46, 501–517.

Boyd, J. P. (2001), *Chebyshev and Fourier Spectral Methods*, Dover Publications.

Brogan, W. (1991), *Modern Control Theory*, Prentice Hall.

Butcher, E. and Bobrenkov, O. (2011), "On the Chebyshev spectral continuous time approximation for constant and periodic delay differential equations," *Commun. Nonlinear Sci. Numer. Simul.*, 16, 1541–1554.

Cuomo, K. and Oppenheim, A. (1993), "Circuit implementation of synchronized chaos, with applications to communications," *Physical Review Letters*, 71, 65–68.

Dunn, T., Guerra, D., and Mohantya, P. (2009), "Noise color and asymmetry in stochastic resonance with silicon nanomechanical resonators," *The European Physical Journal B*, 69, 5–10.

Fang, J. and Lyons, G. (1996), "Structural damping of tensioned pipes with reference to cables," *Journal of Sound and Vibration*, 193, 891–907.

Fielder, B., Flunkert, V., Georgi, M., Hövel, P., and Schöll, E. (2007), "Refuting the Odd-Number Limitations of Time-Delayed Feedback Control," *Phys. Rev. Lett.*, 98, 114101.

Gammaitoni, L., Menichella-Saetta, E., Santucci, S., Marchesoni, F., and Presilla, C. (1989), "Periodically time-modulated bistable systems: Stochastic resonance," *Physical Review A*, 40, 2114–2119.

Gammaitoni, L., Marchesoni, F., and Santucci, S. (1995), "Stochastic Resonance as a Bona Fide Resonance," *Physical Review Letters*, 74, 1052–1055.

Gammaitoni, L., Hanggi, P., Jung, P., and Marchesoni, F. (1998), "Stochastic resonance," *Reviews of Modern Physics*, 70, 223–287.

Gao, Z., Hu, B., and Hu, G. (2001), "Stochastic resonance of small-world networks," *Physical Review E*, 65, 016209–1–016209–4.

Garcia, D. (2010), "Robust smoothing of gridded data in one and higher dimensions with missing values," *Computational Statistics and Data Analysis*, 54, 1167–1178.

Gaul, L., Bohlen, S., and Kempfle, S. (1985), "Transient and forced oscillations of systems with constant hysteretic damping," *Mech. Res. Commun.*, 12, 187–201.

Grover, L. and Weaver, D. (1978), "Cross-flow induced vibrations in a tube bank-vortex shedding," *Journal of Sound and Vibration*, 59, 263–276.

Hanggi, P., Talkner, P., and Borkovec, M. (1990), "Reaction-rate theory: fifty years after Kramers," *Reviews of Modern Physics*, 62, 251–341.

Hänggi, P., Jung, P., Zerbe, C., and Moss, F. (1993), "Can colored noise improve stochastic resonance?" *Journal of Stochastic Physics*, 70, 25–47.

Harris, F. (1978), "On the use of windows for harmonic analysis with the discrete fourier transform," *Proceedings of the IEEE*, 66, 51–83.

Higham, N. (2004), "The numerical stability of barycentric Lagrange interpolation," *IMA J Numer Anal*, 24, 547–556.

Hovel, P. and Socolar, J. (2003), "Stability domains for time-delay feedback control with latency," *Phys. Rev. E*, 68, 036206.

Hughes, I. and Hase, T. (2010), *Measurements and their Uncertainties*, Oxford.

Insperger, T. and Stépán, G. (2002), "Semi-Discretization Method for Delayed Systems," *International Journal for Numerical Methods in Engineering*, 55, 503–518.

Insperger, T. and Stepan, G. (2002), "Stability chart for the delayed Mathieu equation," *Proceedings of Royal Society of London A*, 458, 1989–1998.

Insperger, T. and Stepan, G. (2003), "Stability of the Damped Mathieu Equation With Time Delay," *Journal of Dynamic Systems, Measurement, and Control*, 125, 166–171.

Insperger, T. and Stépán, G. (2004), "Updated semi-discretization method for periodic delay-differential equations with discrete delay," *International Journal for Numerical Methods in Engineering*, 61, 117–141.

Insperger, T. and Stpn, G. (2011), *Semi-Discretization for Time-Delay Systems: Stability and Engineering Applications (Applied Mathematical Sciences)*, Springer, New York.

Insperger, T., Stépán, G., and Turi, J. (2008), "On the higher-order semi-discretizations for periodic delayed systems," *Journal of Sound and Vibration*, 313, 334–341.

Jung, P. (1993), "Periodically driven stochastic systems," *Physics Reports*, 234, 175–295.

Just, W., Bernard, T., Ostheimer, M., Reibold, E., and Benner, H. (1997), "Mechanism of Time-Delayed Feedback Control," *Phys. Rev. Lett.*, 78, 203–206.

Just, W., Reckwerth, D., Reibold, E., and Benner, H. (1999a), "Influence of control loop latency on time-delayed feedback control," *Phys. Rev. E*, 59, 2826.

Just, W., Reibold, E., Benner, H., Kacperski, K., Fronczak, P., and Holyst, J. (1999b), "Limits of time-delayed feedback control," *Phys. Lett. A*, 254, 158–164.

Just, W., Fiedler, B., Georgi, M., Flunkert, V., Hovel, P., and Scholl, E. (2007), "Beyond the odd number limitation: A bifurcation analysis of time-delayed feedback control," *Phys. Rev. E*, 76, 026210.

Kay, S. (1993), *Fundamentals of Statistical Signal Processing*, Prentice-Hall.

Kenfack, A. (2003), "Bifurcation structure of two coupled periodically driven double-well Duffing oscillators," *Chaos, Solitons Fractals*, 15, 205–218.

Kerschen, G., Worden, K., Vakakis, A., and Golinval, J. (2006), "Past, present and future of nonlinear system identification in structural dynamics," *Mechanical Systems and Signal Processing*, 20, 505–592.

Kestin, J. and Khalifa, H. (1976), "Measurement of logarithmic decrements through the measurement of time," *Applied Scientific Research*, 32, 483–493.

Khasawneh, F. and Mann, B. (2010), "A spectral element approach for the stability analysis of time-periodic delay equations with multiple delays," *Journal of vibration and acoustics*, -, –, submitted.

Khasawneh, F. and Mann, B. (2011a), "Stability of delay integro-differential equations using a spectral element method," *Mathematical and Computer Modelling*, 54, 2493–2503.

Khasawneh, F. and Mann, B. (2013), "A spectral element approach for the stability analysis of time-periodic delay equations with multiple delays," *Commun. Nonlinear Sci. Numer. Simul.*, In press.

Khasawneh, F., Mann, B., and Butcher, E. (2011a), "A multi-interval Chebyshev collocation approach for the stability of periodic delayed systems with discontinuities," *Communications in Nonlinear Science and Numerical Simulation*, 16, 4408–4421.

Khasawneh, F., Barton, D., and Mann, B. (2011b), "Periodic solutions of nonlinear delay differential equations using spectral element method," *Nonlinear Dynamics*, 67, 641–658.

Khasawneh, F. A. and Mann, B. P. (2011b), "A spectral element approach for the stability of delay systems," *International Journal for Numerical Methods in Engineering*, pp. 566–592.

Kovaleva, A. (2005), "Noise-induced synchronization and stochastic resonance in a bistable system," *IUTAM Symposium on Chaotic Dynamics and Control of Systems and Processes in Mechanics Solid Mechanics and its Applications*, 122, 345–353.

Kozlowski, J., Parlitz, U., and Lauterborn, W. (1995), "Bifurcation analysis of two coupled periodically driven Duffing oscillators," *Phys. Rev. E*, 51, 1861–1867.

Kramers, H. (1940), "Brownian motion in a field of force adn the diffusion model of chemical reactions," *Physica*, 7, 284–304.

Lathrop, D. P. and Kostelich, E. J. (1989), "Characterization of an experimental strange attractor by periodic orbits," *Phys. Rev. A*, 40, 4028–4031.

Liang, J. and Feeny, B. (2006), "Balancing energy to estimate damping parameters in forced oscillators," *Journal of Sound and Vibration*, 295, 988–008.

Liao, Y. and Wells, V. (2011), "Modal parameteridentificationusingthelogdecrement-method and band-passfilters," *Journal of Sound and Vibration*, 330, 5014–5023.

Lindner, J., Meadows, B., and Ditto, W. (1995), "Array Enhanced Stochastic Resonance and Spatiotemporal Synchronization," *Physical Review Letters*, 75, 3–6.

Litak, G. and Borowiec, M. (2006), "Oscillations with asymmetric single and double well potentials," *Acta Mechanica*, 184, 47–59.

Löcher, M., Cigna, D., Hunt, E., Johnson, G., Marchesoni, F., Gammaitoni, L., Inchiosa, M., and Bulsara, A. (1998), "Stochastic resonance in coupled nonlinear dynamic elements," *Chaos*, 68, 604–615.

Mann, B. and Khasawneh, F. (2009), "An energy-balance approach for oscillator parameter identification," *Journal of Sound and Vibration*, 321, 65–78.

Mann, B. and Patel, B. (2010), "Stability of delay equations written as state space models," *Journal of Vibration and Control*, 16, 1067–1085.

Mann, B. P. and Sims, N. D. (2009), "Energy harvesting from the nonlinear oscillations of magnetic levitation," *Journal of Sound and Vibration*, 319, 515–530.

McDonnell, M. and Abbott, D. (2009), "What Is Stochastic Resonance? Definitions, Misconceptions, Debates, and Its Relevance to Biology," *PL0S Computational Biology*, 5, e1000348.

McNamara, B. and Wiesenfeld, K. (1989), "Theory of stochastic resonance," *Physical Review A*, 39, 4854–4869.

Meirovitch, L. (2001), *Fundamentals of Vibration*, McGraw-Hill.

Mezzetti, E. (1979), "Automatic analysis of the logarithmic decrement in damped oscillations," *Journal of Physics E: Scientific Instruments*, 12, 1163–1165.

Minorsky, N. (1942), "Self Excited Oscillations in Systems Possesing Retarded Actions," *Journal of Applied Mechanics*, 9, 65–71.

Minorsky, N. (1962), *Nonlinear Oscillations*, D. Van Nostrand Company, Inc.

Misono, M., Kohmoto, T., Fukuda, Y., and Kunitomo, M. (1998), "Stochastic resonance in an optical bistable system driven by colored noise," *Optics Communications*, 152, 255–258.

Mohammad, K., Worden, K., and Tomlinson, G. (1992), "Direct parameter estimation for linear and non-linear structures," *Journal of Sound and Vibration*, 152, 471–499.

Nakajima, H. and Ueda, Y. (1998), "Half-period delayed feedback control for dynamical systems with symmetries," *Phys. Rev. E*, 58, 1757.

Ott, E., Grebogi, C., and Yorke, J. (1990), "Controlling Chaos," *Physical Review Letters*, 64, 1196–1199.

Ottman, G., Hofmann, H., Bhatt, A., and Lesieutre, G. (2002), "Adaptive Piezoelectric Energy Harvesting Circuit for Wireless Remote Power Supply," *IEEE Transactions on Power Electronics*, 17, 669–676.

Pandiyan, R. and Sinha, S. (1999), "Periodic flap control of a helicopter blade in forward flight," *Journal of Vibration and Control*, 5, 761–777.

Park, G., Rosing, T., Todd, M., Farrar, C., and Hodgkiss, W. (2008), "Energy Harvesting for Structural Health Monitoring Sensor Networks," *Journal of Infrastructure Systems*, 14, 64–79.

Parter, S. (December 1999), "On the Legendre-Gauss-Lobatto Points and Weights," *Journal of Scientific Computing*, 14, 347–355(9).

Pyragas, K. (1992), "Continuous control of chaos by self-controlling feedback," *Phys. Lett. A*, 170, 421–428.

Pyragas, K. (1995), "Control of chaos via extended delay feedback," *Phys. Lett. A*, 206, 323–330.

Pyragas, K. (2006), "Delayed feedback control of chaos," *Phil. Trans. R. Soc. A*, 364, 2309–2334.

Reddy, J. (1993), *An Introduction To The Finite Element Method*, McGraw-Hill, Inc., New York, NY, 2 edn.

Saito, H. and Yaguchi, H. (1982), "Frequency and loss factor of rectangular plates reinforced by intermediate viscoelastic line supports," *Journal of Sound and Vibration*, 83, 157–162.

Scholl, E. and Schuster, H. G. (2008), *Handbook of Chaos Control*, Wiley-VCH, 2 edn.

Simiu, E. (2002), *Chaotic transitions in deterministic and stochastic dynamical systems: applications of Melnikov processes in engineering, physics, and neuroscience*, Princeton University Press.

Sinha, S. (2004), "Dynamic characteristics of a flexible bladed-rotor with Coulomb damping due to tip-rub," *Journal of Sound and Vibration*, 273, 875–919.

Socolar, J., Sukow, D., and Gauthier, D. (1994), "Stabilizing unstable periodic orbits in fast dynamical systems," *Phys. Rev. E*, 50, 3245–3248.

Sodano, H., Inman, D., and Park, G. (2005), "Comparison of Piezoelectric Energy Harvesting Devices for Recharging Batteries," *Journal of Intelligent Material Systems and Structures*, 16, 799–807.

Stanton, S., McGehee, C., and Mann, B. (2010), "Nonlinear dynamics for broadband energy harvesting: Investigation of a bistable piezoelectric inertial generator," *Physica D: Nonlinear Phenomena*, 239, 640–653.

Stanton, S., Mann, B., and Owens, B. (2011), "Melnikov theoretical methods for characterizing the dynamics of the bistable piezoelectric inertial generator in complex spectral environments," *Physica D: Nonlinear Phenomena*, 241, 711–720.

Sukow, D., Bleich, M., Gauthier, D., and Socolar, J. (1997), "Controlling chaos in a fast diode resonator using extended time-delay autosynchronization: Experimental observations and theoretical analysis," *Chaos*, 7, 560–576.

Tamaševičius, A., Mykolaitis, G., Pyragas, V., and Pyragas, K. (2007), "Delayed feedback control of periodic orbits without torsion in nonautonomous chaotic systems: Theory and experiment," *Phys. Rev. E*, 76, 026203.

Tweten, D. and Mann, B. (2012a), "Parameter Identification of a Nonlinear Beam Energy Harvester," in *Proceedings of the 24th Conference on Mechanical Vibration and Noise, Chicago*.

Tweten, D. and Mann, B. (2012b), "Spectral element method and the delayed feedback control of chaos," *Phys. Rev. E*, 86, 046214.

Tweten, D. and Mann, B. (2013), "On the use of weighting matrices to improve harmonic balance parameter identification results," *Journal of Sound and Vibration*, 332, 2941–2953.

Tweten, D., Lipp, G., Khasawneh, F., and Mann, B. (2012), "On the comparison of semi-analytical methods for the stability analysis of delay differential equations," *J. Sound Vib.*, 331, 4057–4071.

van den Bos, A. (1989), "Estimation of Fourier Coefficients," *IEEE Transactions on Instruments and Measurements*, 38, 1005–1007.

Welch, P. (1967), "The use of fast fourier transform for the estimation of power spectra," *IEEE Transactions on Audio and Electroacoustics*, 15, 70–73.

Whetham, W. (1890), "On the Alleged Slipping at the Boundary of a Liquid in Motion," *Phil. Trans. R. Soc. Lond. A*, 181, 559–582.

Wilcox, P. and Crawford, W. (1968), "A least squares method for the reduction of free-oscillation data," Tech. Rep. TN D-4503, National Aeronautics and Space Administration.

Yasuda, K. and Kamiya, K. (1990), "Identification of a Nonlinear Beam (Proposition of an Identification Technique)," *JSME International Journal, Series III*, 33, 535–540.

Yasuda, K., Kawamura, S., and Watanabe, K. (1988a), "Identification of Nonlinear Multi-Degree-of-Freedom Systems (Identification Under Noisy Measurements)," *JSME International Journal, Series III*, 31, 502–509.

Yasuda, K., Kawamura, S., and Watanabe, K. (1988b), "Identification of Nonlinear Multi-Degree-of-Freedom Systems (Presentation of an Identification Technique)," *JSME International Journal, Series III*, 31, 8–14.

Yuan, C. and Feeny, B. (1998), "Parametric Identification of Chaotic Systems," *Journal of Vibration and Control*, 4, 1–22.

Zhou, T., Moss, F., and Jung, P. (1990), "Escape-time distributions of a periodically modulated bistable system with noise," *Physical Review A*, 42, 3161.

Biography

Dennis Jeremy Tweten was born on November 29, 1976 in Englewood, Colorado. He earned is BS from LeTourneau University in Engineering, and his MSE from The University of Texas at Austin in Mechanical Engineering. He began is PhD studies at Duke University in 2010.

Awards

James B. Duke Fellowship, Duke University, 2010

Phi Kappa Phi, National Honor Society, 2003

Thrust Fellowship, The University of Texas, 2001

Epsilon Eta Sigma, Engineering Honor Society, 1994

Journal Publications

D. Tweten, B. Mann, (2013), "On the use of weighting matrices to improve harmonic balance parameter identification results," *J. Sound Vib.*, 332, 2941–2953.

D. Tweten, B. Mann, (2012), "Spectral element method and the delayed feedback control of chaos," *Physical Review E*, 86, 046214.

D. Tweten, G. Lipp, F. Khasawneh, B. Mann, (2012), "On the comparison of semi-analytical methods for the stability analysis of delay differential equations," *J. Sound Vib.*, 331, 4057–4071.